

**ELASTIC PROPERTIES PREDICTION FOR DRILLING AND
SUBSURFACE EVALUATION FOR THE GRAND BANKS AND
NIGER DELTA**

©Babatunde Olaiya Yusuf, B.Eng., M.Eng.

A thesis submitted to the School of Graduate Studies
In partial fulfilment of the requirements for the degree of

Doctor of Philosophy

In

Oil and Gas Engineering

Faculty of Engineering and Applied Science
Memorial University of Newfoundland
St John's, Newfoundland, Canada

July, 2019

Abstract

Formation bulk density (ρ_b) is an essential parameter which can provide very useful information required for planning the position of a new well and properly characterize a reservoir for effective field development. Several correlations had been developed in the past decades to estimate bulk density. A previous study done using data from the Grand Banks reveal that the prior density-velocity relations could not predict density accurately in the five wells studied. The two major problems with these empirical relationships are: (1) they were developed primarily for clean formations and they have failed to produce reasonable estimates in non-clean/mixed-lithology formations; (2) they are not applicable to rocks that contain micro-cracks/fractures. There is no single model that has dealt with these two problems. In this thesis, a new formation bulk density prediction method that can be applied to clean formations, non-clean/mixed-lithology formations and rocks that contain micro-cracks is proposed. The model is validated with additional laboratory measurements on cores and field-tested with field wireline log data from the Niger Delta and Grand banks basins.

The most reliable method of deriving the shear wave velocity is by estimation from compressional wave velocity. Most old wells lack shear wave velocity data and for the wells drilled recently, the need to verify poor quality data makes the development of models very important. A region-specific model is proposed for more accurate derivation of shear wave velocity from compressional wave velocity applicable to the Grand Banks. This model was found to predict better than prior models.

Poisson's ratio is commonly utilized in estimation of fracture pressure. There is need to develop a correlation specific for the Grand Banks. The availability of sufficient well data, a depth trend of Leak-off-test (LOT) data and series of Modular Dynamic Formation Tester (MDT) type data were used to establish a depth trend of fracture pressure and pore pressure profiles to aid successful well planning. The application of outputs from these models and correlations to subsurface reservoir characterization and field development was tested using the Excess Pressure (EP) methodology.

Acknowledgement

I would like to express my sincere gratitude to Dr. Stephen Butt for his professionalism, invaluable guidance and patience during the different phases of my doctorate research and thesis development. I also would like to thank Dr. Sam Nakhla and Dr. James Yang for their contributions through providing challenging ideas as members of my supervisory committee. I also acknowledge the contributions from Robert Flemming and Olalere Oloruntobi.

I owe a heartfelt thanks to my family; my late father for giving me a sound educational, spiritual and personal foundation. I pray to the Almighty God to grant him paradise; my sincere thanks and appreciations also go to my wonderful mother, my brother and my sisters. My unwavering love, thanks and appreciation goes to my wife; a rare gem, without whom this degree will not be possible, and our special, blessed and gifted kids; Maryam, AbdurRahman, Aisha and AbduLlah. I love you all and thank you all for your understanding, support, inspiration and encouragement.

Table of Contents

Abstract	i
Acknowledgement	ii
List of Tables	viii
List of Figures	ix
Nomenclature	xii
Chapter 1	1
Topic Development	1
1.1 Introduction.....	1
1.2 Research Objectives	9
1.3 Contributions of the Research.....	10
1.4 Thesis Organization	11
Chapter 2	13
Literature Review	13
2.1 Density - Compressional Velocity Relation	13
2.2 Shear Velocity - Compressional Velocity Relation.....	20
2.3 Poisons-Ratio, Fracture Pressure and Pore Pressure.....	24
2.4 Excess Pressure Methodology	29

2.4.1 Excess Pressure Concept	29
2.4.2 Subsurface Pressure Barriers	32
2.5 Geology of the Grand Banks.....	35
2.5.1 Jeanne d’Arc Basin.....	37
2.5.2 Flemish Pass Basin	40
2.5.3 Other Sedimentary Basins.....	41
2.6 Geology of the Niger Delta	42
2.7 Chapter Summary.....	45
Chapter 3	46
Prior Bulk Density Model Calibration	46
3.1 Bulk Density from Compressional Velocity	46
3.1.1 Data Quality Control.....	47
3.1.2 Lithology Separation	47
3.2 RhoB - Vp Relation	48
3.3 Discussion of Calibration Methodology	56
3.4 Chapter Summary.....	58
Chapter 4	59
A New Formation Bulk Density Model.....	59
4.1 The New Formation Bulk Density Prediction Technique	59
4.2 Model Method 1 Development.....	60
4.2.1 Model Method 1 Calibration.....	61
4.2.2 Validation of the Model Method 1	64
4.2.3 Grand Banks Basin Example for Model Method 1	68

4.2.4 Niger Delta Basin Example for Model Method 1	72
4.3 Model Method 2 Development.....	77
4.3.1 Model Method 2 Methodology	77
4.3.2 Validation of Model Method 2	79
4.3.3 Grand Banks Basin Example for Model Method 2	83
4.3.4 Niger Delta Basin Example for Model Method 2	85
4.4 Discussion of Model Methods 1 and 2 Results	87
4.5 Model Method 2 for Siliciclastic Formations	88
4.6 Chapter Summary.....	96
Chapter 5	97
A Shear-Wave Velocity Model	97
5.1 Shear Velocity from Compressional Velocity.....	97
5.2 Previous Vs Models Preview.....	97
5.3 The Proposed Vs Model Development.....	98
5.4 The Proposed Vs Model Calibration	100
5.5 Field Wells Validation.....	101
5.5.1 Well GB2 Shear Wave Velocity Validation.....	101
5.5.2 Well GB3 Shear Wave Velocity Validation.....	105
5.5.3 Well GB4 Shear Wave Velocity Validation.....	109
5.6 Shear Wave Velocity Model Results Discussion	113
5.7 Chapter Summary.....	114
Chapter 6	115

Poisson’s Ratio Profile for the Grand Banks	115
6.1 Poisson’s Ratio Correlation	115
6.2 Eaton Poisson’s Ratio Profile Comparison	117
6.3 GB Regional Poisson’s Ratio Profile Derivation	119
6.4 Fracture and Pore Pressure Prediction from Poisson’s Ratio	126
6.5 Fracture Pressure Correlation for the Jeanne d’Arc Basin.....	129
6.6 Chapter Summary.....	131
Chapter 7	132
Excess Pressure Methodology.....	132
7.1 Excess Pressure Methodology.....	132
7.2 Field Data analyses.....	133
7.2.1 Well GB5 Analysis.....	134
7.2.2 Well GB6 Analysis.....	139
7.3 Reservoir Compartmentalization	145
7.4 Chapter Summary.....	148
Chapter 8	149
Conclusions and Recommendations	149
8.1 Conclusions	149
8.2 Recommendations.....	152
Appendix A.....	153
Appendix B	157

References 185

List of Tables

Table 1: RMSE Comparison - Calibrated Model and Gardner Model	56
Table 2: R-squared Comparison - Calibrated Models: Sand and Shale.....	57
Table 3: Model Validation's R-Square Values Comparison	67
Table 4: The laboratory data for samples #1 and #2 (Han et al. 1986).	80
Table 5: RMSE Comparison - Developed Shear Wave Velocity Model and Prior Models	113

List of Figures

Figure 1: The dipole sonic log through the Alba reservoir sand shows a large contrast in shear wave velocity and a small contrast in compressional- wave velocity with the surrounding shales (MacLeod et al., 1999).....	3
Figure 2: The Importance of Pressure data in the Petroleum Industry (Green, 2012)	5
Figure 3: Fracture pressure and Pore pressure applied to Casing Design (Zhang and Yin, 2017).....	7
Figure 4: Hierarchy of Pressure Data (Green, 2012)	8
Figure 5: Vp versus Vs for different lithology (Castagna, 1985).....	22
Figure 6: Relationship between Shale resistivity parameter and reservoir fluid pressure gradient pre Hottman and Johnson (Adapted from Fooshee, 2009).....	24
Figure 7: Variation of Poisson's ratio with depth (Eaton, 1969)	27
Figure 8: Fluid Contacts and Gradients in an Ideal Reservoir	31
Figure 9: Subsurface Geo-pressure System (Green, 2012)	33
Figure 10: Excess Pressure derived from Fluid Density (Brown, 2003)	34
Figure 11: Sedimentary Basins in the Grand Banks (Whiterose DA Volume 2, 2001).....	37
Figure 12: Jeanne D'Arc Lithostratigraphy (CNLOPB, 2019).....	39
Figure 13: Schematic Cross Section based on seismic line (NL Department of Mines and Energy, 2000)	41
Figure 14: Geologic Map of the Niger Delta (Ajayi and Okosun, 2014).....	42
Figure 15: Stratigraphy Column of the Niger Delta.....	44
Figure 16: Calibrating Well GB1 - Measured and Gardner Model comparison with GR and Resistivity logs.....	49
Figure 17: Distinct Sand and Shale on a Density-Velocity Log Plot for a Grand Bank well.....	50
Figure 18: Shale Calibration from the Calibrating Well GB1 with GR and Resistivity logs	51
Figure 19: Comparison of estimated and measured (log) p-wave wave velocities for well GB1 Shale Interval	53
Figure 20: Sand Calibration from the Calibrating Well GB1 with GR and Resistivity logs.....	54
Figure 21 : Comparison of estimated and measured (log) p-wave wave velocities for well AA Sand Interval	55
Figure 22: New Density Prediction Model Calibration using Hans et. al. Laboratory data at 5 MPa	62
Figure 23: New Density Prediction Model Calibration using Hans et. al. Laboratory data at 10 MPa	62
Figure 24: New Density Prediction Model Calibration using Hans et. al. Laboratory data at 20 MPa	63
Figure 25: New Density Prediction Model Calibration using Hans et. al. Laboratory data at 30 MPa	63

Figure 26: Gardner et al. Model for density prediction using Hans et al. Laboratory data at 5 MPa	65
Figure 27: Gardner et al. Model for density prediction using Hans et al. Laboratory data at 10 MPa	65
Figure 28: Gardner et al. Model for density prediction using Hans et al. Laboratory data at 20 MPa	66
Figure 29: Gardner et al. Model for density prediction using Hans et al. Laboratory data at 30 MPa	66
Figure 30: Approximate GB1 Well Location (NESS, 2019).....	69
Figure 31: (a) Gamma Ray and Resistivity Logs (b) Compressional velocity and Caliper log readings for GB1 well.	70
Figure 32: Measured versus predicted formation bulk density using the model method 1 for GB1 well.	71
Figure 33: Model Method 1 Density Prediction validation for GB1 well.....	72
Figure 34: Approximate ND1 Well Location (Adegoke et al., 2010)	73
Figure 35: (a) Gamma Ray-Resistivity (b) compressional velocity and caliper log plots for ND1 well	74
Figure 36: (a) Vp - Caliper plots (b) New density model match with measured density for ND1 well	75
Figure 37: Model Method 1 Density Prediction validation for ND1 well	76
Figure 38: The differential Pressures, Sonic Velocities and Porosities for samples #1 and #2.....	81
Figure 39: Measured versus predicted formation bulk density using the model method 2 for GB1 well.	84
Figure 40: Model Method 2 Density Prediction validation for GB1 well.....	85
Figure 41: Measured versus predicted formation bulk density using the model method 2 for ND1 well.	86
Figure 42: Model Method 2 Density Prediction validation for ND1 well	87
Figure 43: The well logs for well ND2 showing the petrophysical properties of the penetrated rocks.	89
Figure 44: The comparison of predicted and measured formation bulk density for various models under consideration for well ND2.....	92
Figure 45: The cross-plots of predicted and measured bulk density with histograms for Well ND2.	94
Figure 46: Well GB2 - Matching plots of new model with measured data with GR plot	102
Figure 47: Well GB2 - Measured and Estimated Vs with Residual frequency for Brocher model.	103
Figure 48: Well GB2 - Measured and Estimated Vs with Residual frequency for Castagna model.....	103
Figure 49: Well GB2 - Measured and Estimated Vs with Residual frequency for Han model	104
Figure 50: Well GB2 - Measured and Estimated Vs with Residual frequency for New model	104
Figure 51: Well GB3 - Matching plots of new model with measured data with GR plot	106

Figure 52: Well GB3 - Measured and Estimated Vs with Residual frequency for Brocher model.	107
Figure 53: Well GB3 - Measured and Estimated Vs with Residual frequency for Castagna model	107
Figure 54: Well GB3 - Measured and Estimated Vs with Residual frequency for Han model	108
Figure 55: Well GB3 - Measured and Estimated Vs with Residual frequency for New model	108
Figure 56: Well GB4 - Matching plots of new model with measured data with GR plot	110
Figure 57: Well GB4 - Measured and Estimated Vs with Residual frequency for Brocher model.	111
Figure 58: Well GB4 - Measured and Estimated Vs with Residual frequency for Castagna model	111
Figure 59: Well GB4 - Measured and Estimated Vs with Residual frequency for Han model	112
Figure 60: Well GB4 - Measured and Estimated Vs with Residual frequency for New model	112
Figure 61: Poisson Ratio from V_p/V_s and Poisson Ratio trend from Eaton method, shown for three GB wells	118
Figure 62: Bulk density trend from three Grand Banks Wells	121
Figure 63: Overburden Pressure and Gradient derived from formation bulk density.....	122
Figure 64: Derivation of Overburden Gradient - R-Squared and Equation	123
Figure 65: Established Poisson Ratio Trend for the Grand Banks Basins.....	124
Figure 66: Grand Bank Basins Poisson Ratio trend, Poisson Ratio from V_p/V_s and Poisson Ratio trend from Eaton, shown for three GB wells	125
Figure 67: The Jeanne D'Arc Basin (Enachescu M.E., 2005)	126
Figure 68: Fracture and Pore pressure data points for some Grand Bank Wells.....	128
Figure 69: A new correlation for estimating Fracture pressure (FP), given the Pore Pressure (PP) and Depth (D).	130
Figure 70: P-D Plot for Well GB5.....	134
Figure 71: Well GB5 Hydrostatic and Oil Gradient.....	135
Figure 72: Well GB5 Water Gradient.....	135
Figure 73: Well GB5 Water EP vs. TVD Plot.....	136
Figure 74: Well GB5 Oil EP vs. TVD Plot.....	137
Figure 75: Well GB5 Oil Leg 2 EP vs. TVD Plot.....	138
Figure 76: Well GB5 Oil Leg 3 EP vs. TVD Plot.....	139
Figure 77: P-D Plot for Well GB6.....	140
Figure 78: Well GB6 Hydrostatic and Oil Gradient.....	141
Figure 79: Well GB6 Hydrostatic and Oil Gradient.....	141
Figure 80: Well GB6 Water EP vs. TVD Plot.....	142
Figure 81: Well GB6 Oil EP vs. TVD Plot.....	143
Figure 82: Well GB6 Oil Leg 1 EP vs. TVD Plot.....	144
Figure 83: Well GB6 Oil Leg 2 EP vs. TVD Plot.....	145
Figure 84: Compartmentalization Plot using Well GB6 gradients.....	146
Figure 85: Compartmentalization Plot using Well GB5 gradients.....	147

Nomenclature

GB	Grand Banks
ND	Niger Delta
NRC	Natural Resource Canada
DPR	Department of Petroleum Resources
CNLOPB	Canada Newfoundland and Labrador Offshore Petroleum Board
NESS	Nalcor Exploration Strategy System
V_p	Compressional wave travel time ($\mu\text{sec}/\text{ft}$)
V_s	Shear wave travel time ($\mu\text{sec}/\text{ft}$)
V_{sh}	Volume of Shale
ρ_{ob}	Bulk Density (g/cc)
GR	Gamma ray log (gAPI)
ILD	Resistivity
V_{sh}	Shale volume
ρ_{ma}	Matrix density (g/cc)
ρ_{fl}	Fluid density (g/cc)
GR_{min}	Minimum Gamma ray (clean sandstone)
GR_{max}	Maximum Gamma ray (shale)
ϕ	Rock porosity
EP / P_{ex}	Excess Pressure

WOC	Water Oil Contact
GOC	Gas Oil Contact
TZ	Transition Zone
P-D	Pressure-Depth
FWL	Free Water Level
HWC	Hydrocarbon Water Contact
CQG	Crystal Quartz Gauge
QC	Quality Control
TVD	True Vertical Depth
Gpp	Pore Pressure Gradient
Gop	Overburden Pressure Gradient
FPG	Fracture Pressure Gradient
RFT	Repeat Formation Tester
MDT	Modular Formation Tester
RDT	Reservoir Description Tool
RMSE	Root Mean Square Error
R^2	R-Squared
LOT	Leak-Off Test
FPG	Fracture Pressure Gradient
PR	Poisson's Ratio
PP	Pore Pressure

Chapter 1

Topic Development

1.1 Introduction

Through rock physics and seismic data analyses, the ability to predict fluid and rock properties of hydrocarbon reservoirs have become clearer and well understood. This has continued to aid the discovery and development of petroleum resources around the world and more importantly as we dive into deeper and challenging environments.

Formation bulk density (RhoB) is an essential parameter which can provide very useful information required for planning the position of a new well as well as properly characterizing the reservoir. Techniques to derive bulk density include from density log, from compressional velocity using derived correlations, through basin modeling and from rock cuttings. Several correlations had been developed in the past decades to estimate RhoB from compressional p-wave velocity (V_p). Typically, this data will not be fully obtained from all section of a drilled well for various reasons including tool failure, cost considerations etc. The most used of these correlations is the one developed by Gardner et al. (1974). While the Gardner correlation was applied to different lithology using

data from the Gulf of Mexico (GOM), it has been found not to work in some regions. Previous study by Sarasty and Stewart (2002) on offshore Newfoundland reveal that the Gardner relation could not predict density accurately in the five studied wells in the Whiterose field. An important objective of this research is to develop a new density-velocity relationship using case studies from the Grand Banks area and the Niger Delta basin. Wells data from significant discovery sedimentary basins covering both deep and shallow water were analyzed. Correlation coefficients from a calibrating well were developed and verified using field wells with both sands and shales characteristics. The new model which incorporates the effect of mixed lithology and rocks with micro-cracks gave a better prediction of bulk density from compressional p-wave velocity than the Gardner model. This newly proposed model is expected to work favorably well in other basins.

Petro-physical properties are measured by well logs, analysis of which enables development of empirical relationships between properties and various parameters. Shear-wave velocity (V_s) data are not available for many of the wells drilled to date and for the very recent wells with V_s data, it is possible that acquired data are unreliable and thus, there will be need to re-estimate V_s from compressional-wave velocity (V_p). Having V_s estimated from V_p can also serve as a very good quality control tool. General empirical relations have been

developed over the years but most of them are derived to work for specific regions making their use in other regions like the Grand Banks produce erroneous results. The measurements of shear and compressional wave velocities in various rock types have been made possible by the development of more advanced dipole sonic logging tools.

Formation bulk density, compressional wave velocity and shear wave velocity are depth dependent elastic properties which can be derived by developing depth trends. From petroleum exploration point of view, depth trends are usually applied to better understand the seismic signature which is very important in the search for oil and gas. Empirical trends can be fitted and various lithology can be differentiated using cut-offs. Another method of deriving these depth dependent properties is the use of empirical porosity-depth trends for different lithology.

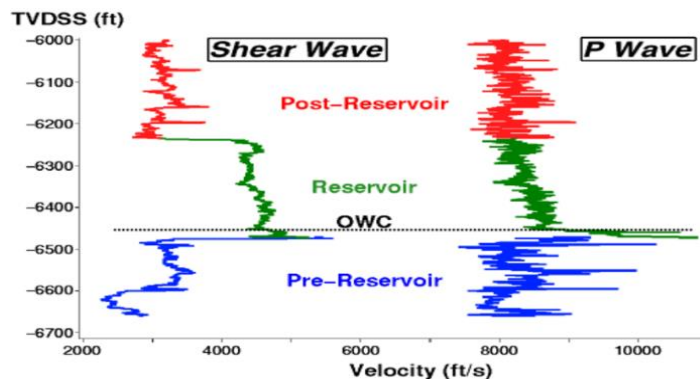


Figure 1: The dipole sonic log through the Alba reservoir sand shows a large contrast in shear wave velocity and a small contrast in compressional-wave velocity with the surrounding shales (MacLeod et al., 1999).

Rock physics provides a link between geologic reservoir parameters such as porosity, clay content, texture, lithology, cement content and saturation with the seismic properties V_p , V_s and ρ or derivatives of them such as, acoustic impedance, P-wave/S-wave velocity-ratio (V_p/V_s), Poisson's ratio and elastic moduli. A wide variety of rock physics models can be used to interpret observed sonic and seismic velocities in terms of the reservoir parameters or to extrapolate beyond the available data range to examine certain what-if scenarios, such as fluid or lithology variations. It is important however to recognize that the models have a certain degree of advantages and limitations, and have to be carefully calibrated to local conditions and areas (Ikcon Science, 2016)

In seismic work, it is vital to be able to monitor how the compressional wave velocity, the shear wave velocity and fluid and rock density change with time which could assist in the prediction of the effect of changes in seismic amplitudes and travel times.

Using Eaton (1969) method for pore pressure estimation, pore pressure can be estimated from normal pressure compaction trend line, overburden stress and the resistivity. Using Eaton method for fracture pressure estimation, fracture pressure can be estimated by knowing the pore pressure, poisson's ratio and the formation overburden stress. The Eaton method is generally accepted as a reliable and accurate method of estimating fracture pressure once the pore

pressure data is available but it was derived using data from the Gulf of Mexico. Poisson's ratio (μ) curve, after being established for a specific well, can be applied over a known area, provided fracture pressure can be fairly estimated.

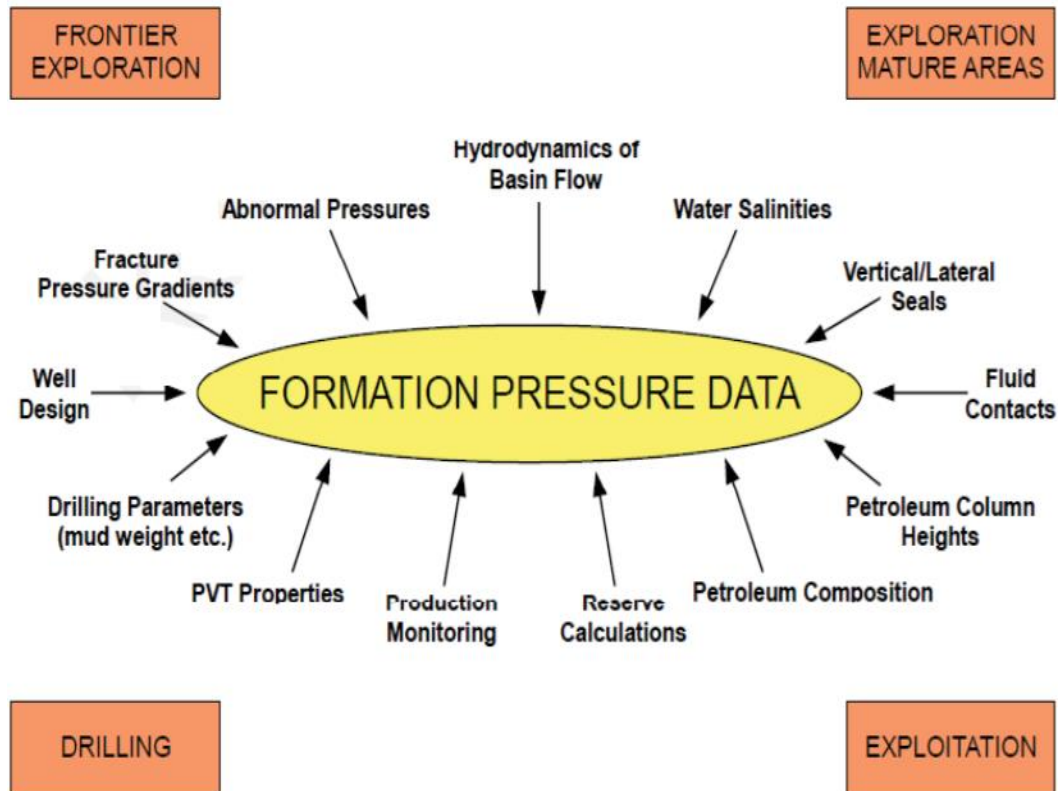


Figure 2: The Importance of Pressure data in the Petroleum Industry (Green, 2012)

Hydrostatic gradient is controlled by the density which is a function of how saline the water is. Although, it is often depicted by a straight line, in reality, it is not a straight line; it varies with the formation depth. It serves as a reference for the determination of formation overpressure.

$$P = \rho \cdot g \cdot h \quad (1.1)$$

Where ρ is the average fluid density, g is the acceleration due to gravity and h is the vertical height of the fluid column measured from the datum.

In combination with neutron log, formation bulk density can be used for lithology and pore fluid identification. Formation bulk density is also required for porosity and overburden pressure determinations. Overburden pressure is the pressure exerted by the weight of the overlying sediments including the weight of the contained fluids. Overburden gradients can be plotted for different geologic settings. It is the upper limit of pressure that can be held by the petroleum system. Deriving an accurate overburden pressure is a very important input to pore pressure prediction. Overburden pressure can be derived from density logs, sonic logs, cores and basin modeling.

$$S_v = \rho_b \cdot D \quad (1.2)$$

$$\rho_b = \rho_m (1 - \Phi) + \rho_f (\Phi) \quad (1.3)$$

Where ρ_b is the bulk density, ρ_m is the matrix density, ρ_f is the fluid density and Φ is the porosity.

Fracture pressure is the minimum compressive strength. Hydro-fractures occur in the formation when the pore pressure exceeds the fracture pressure. Dickson

(1953) define overpressure as any pore fluid pressure which exceeds the hydrostatic pressure of a column of water. Several correlations are available for estimating fracture pressure including models developed by Mathews and Kelly (1967), Eaton (1969), Breckels and Van Eekelen (1981) and Daines (1982).

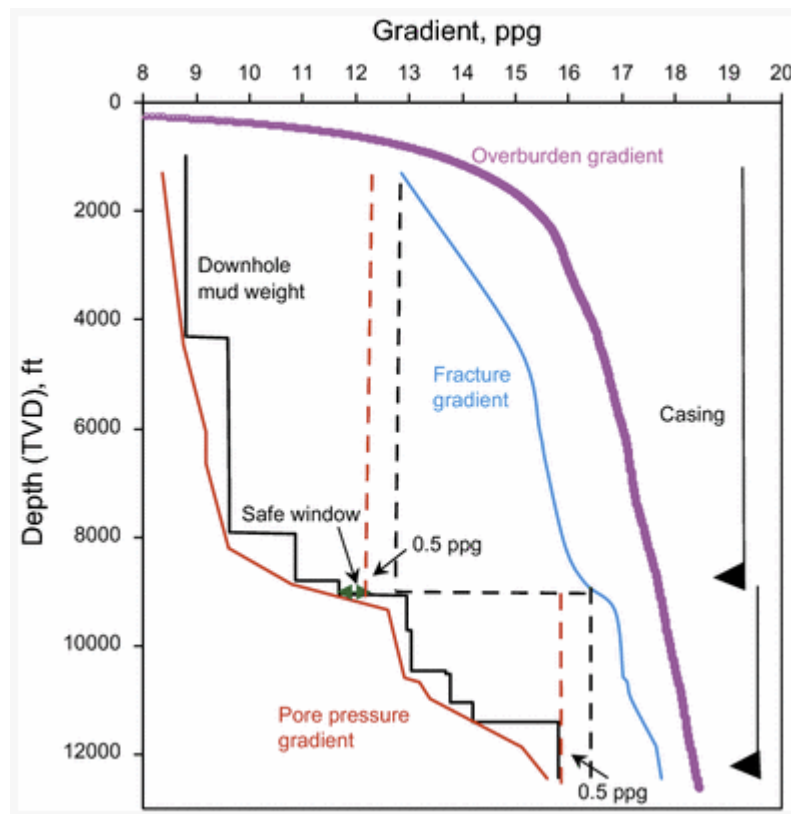


Figure 3: Fracture pressure and Pore pressure applied to Casing Design (Zhang and Yin, 2017)

Pressure-depth (P-D) plots have been the standard method used in the petroleum industry for interpreting wireline test data which is used to estimate

subsurface reservoir properties. Hydrostatic P-D plot is a plot of stabilized formation pressure and true vertical depth (TVD). This plot is used to evaluate subsurface fluids contacts as well as detect the presence of hydrocarbons. However, these plots can be very difficult to interpret. The fluid pressure gradients can be very similar, appearing parallel to each other in many cases. Also, from pressure-depth plots, fluid density is often calculated from regression, in which case, pressure barriers or small subtle changes in fluid-density can go unnoticed before regression. Thus, an uncertain fluid-density could be calculated from the trend. The Excess Pressure methodology removes the effect of a chosen fluid density, which improves the visualization of the very fine fluid-density differences or the presence of pressure barriers.

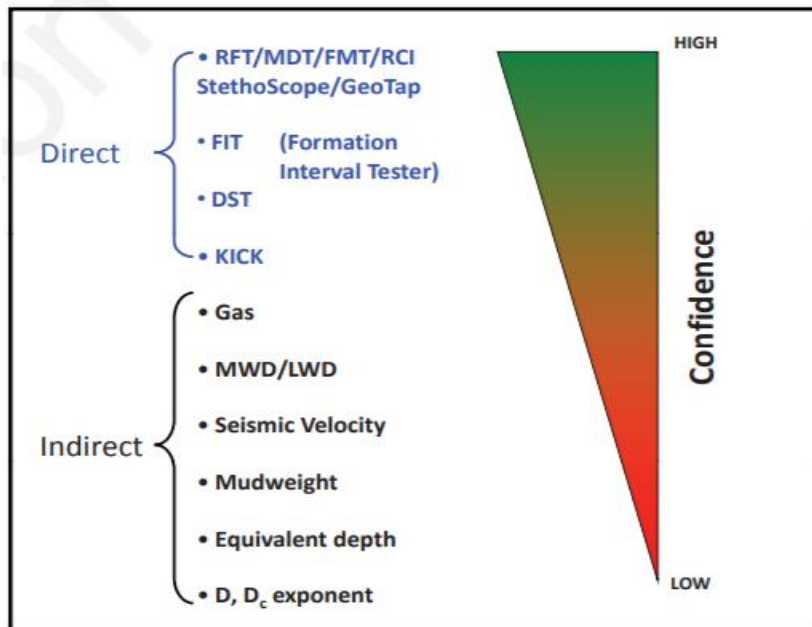


Figure 4: Hierarchy of Pressure Data (Green, 2012)

1.2 Research Objectives

The main focus of this research is to develop fit-for-purpose ρ , V_s , μ and fracture pressure models and correlations that are suitable for petroleum exploration, drilling well planning and reservoir characterization for basins and stratigraphy using case studies from offshore Newfoundland and Labrador Grand Banks and the West African Niger Delta Basins. Through these, the concept of micro-cracks is introduced in a newly derived density model and a new density term is introduced in the derived V_s equation. Furthermore, the research also explores the application of outputs from these correlations and models for fluid contacts determination and reservoir compartments discovery using the Excess Pressure methodology. The main focuses of this research are summarized below:

- ❖ Develop a new model for formation bulk density estimation by incorporating components of mixed-lithology and micro-cracks.
- ❖ Test the newly derived formation bulk density model using case studies from the Grand Banks and Niger Delta and as such prove it could be applicable to predict bulk density in other regions.
- ❖ Develop a model for the estimation of shear s-wave velocity from compressional p-wave velocity using well example from the Grand Banks.

- ❖ Test the superiority of the developed shear wave model for applicability in the basins offshore Newfoundland and Labrador when compared with industry used models
- ❖ Develop a correlation of Poisson's ratio: formation-depth correlation which can be used for fracture pressure estimation. Utilize pressure data and Leak-off test (LOT) data from 93 wells in the Grand Banks basins to show a trend for Fracture Pressure in the Jeanne d'Arc basin of the Grand Banks.
- ❖ Apply the Excess Pressure methodology for fluid density determination, subsurface properties estimation and field development.

1.3 Contributions of the Research

The resulting contributions from this thesis can be highlighted as follows:

- ❖ A new formation bulk density prediction model applicable to mixed lithology and rocks with micro-cracks.
- ❖ A shear s-wave velocity model which is found to be superior to prior models.
- ❖ A Poisson's ratio - depth trend that can be used to estimate Poisson's ratio values from seabed to total depth (TD) in the Grand Banks area. A

trend of fracture pressure and pore pressure difference as a function of depth for the Jeanne d'Arc basin of the Grand Banks.

1.4 Thesis Organization

Chapter 1 highlights the fundamental backgrounds of the topic development.

Chapter 2 provides a review of the literatures and recent developments in rock elastic properties correlations, geo-pressure estimation and subsurface pressure analyses.

Chapter 3 highlights the calibration of the prior formation bulk density model in sand and shaly formations.

Chapter 4 presents the process of development of the new formation bulk density prediction model which incorporates the concept of mixed lithology and micro-cracks.

Chapter 5 presents a more systematic approach and model development for the estimation of shear s-wave velocity.

Chapter 6 buttresses the application of the Eaton methodology which was utilized to derive Poisson's ratio as a function depth using the formation bulk density data for three offshore wells to derive the overburden gradient, together with fracture and pore pressure data at similar depths. The derived Poisson's

ratio equation is applicable to the Grand Banks. This chapter also explores the methodology applied to arrive at a fracture-pore pressure trend for the Jeanne d'Arc basin of the Grand Banks.

Chapter 7 connects the concept of Excess Pressure methodology for fluid density application from which sub-surface fluid contacts and reservoir compartmentalization can be effectively approximated. These are very important piece of information for field development.

Chapter 8 provides the concluding remarks about the research and some recommendations for future work.

Chapter 2

Literature Review

2.1 Density - Compressional Velocity Relation

Porosity, water saturation and hydrocarbon fluid type and rock mineral composition all depends on the rock bulk density. For drilling engineers, these information aids planning the position of a new producing or injecting well. For subsurface engineers, it provides essential information for characterizing a reservoir. In subsurface reservoir engineering, cross-plot of rock properties and lithology and pore fluid indicate that density provides the best differentiation between hydrocarbon reservoirs and other rock/fluid types (Van Koughnet et al., 2003), making accurate density estimates significant for reservoir characterization.

The formation bulk density is an essential parameter required for geo-mechanical analysis and reservoir characterization. Accurate knowledge of formation bulk density is required in planning the position of a new producing or injecting well. Information about the formation bulk density are required to estimate the rock mechanical properties such as Young's modulus, Bulk modulus, Shear modulus and Rock matrix compressibility (Tixier et al. 1975;

Coates and Denoo 1980; Chang et al. 2006; Ameen et al., 2009; Najibi et al., 2015). In combination with neutron log, formation bulk density log can be used for lithology and pore fluid identification. Formation bulk density data are also required for porosity and overburden pressure determinations. The magnitude of overburden pressure is obtained by integrating the density logs from surface to the depth of interest along the well path (Christman 1973; Zoback et al. 2003; Aadnoy 2010). Information about the formation bulk density can be used to estimate the pore pressure and determine the origin of subsurface overpressure conditions (Athy, 1930; Rubey & Hubber 1959; Hart et al., 1995; Bowers 2001; Flemings et al. 2002; Hoseni 2004).

Bulk density logs are among the common types of logs usually acquired in a well along with Gamma ray logs, Resistivity logs and Neutron logs. However, there are instances whereby formation bulk density logs predictions are required especially in the top hole sections. Due to the big hole sizes of the top hole sections and the unconsolidated nature of the sediments in the top holes, density logs are usually not acquired in these depth intervals (Zoback 2010). The excessive washouts that usually occur in the top holes sections limit the acquisition of density logs. Since the density logs are required for overburden pressure determination, density logs must be predicted in these intervals.

Bulk density prediction is an important aspect of petroleum exploration. The bulk density of the formation enables the derivation of a value for the total porosity of the formation which is needed to properly characterize the reservoir. Other uses of bulk density is the identification of minerals such as evaporates and the detection of gas-bearing formations.

The density tool records the bulk density of the formation. The porosity derived from this will include all pores and fractures whether they are connected or not. The sonic tool can also be used to measure the porosity of the formation. However, the sonic tool is not sensitive to fracture porosity. Hence, the difference between the porosities derived from these two measurements can be used as an indicator of the extent of fracturing in a reservoir interval (Glover, 2010)

Empirical relations have become available to predict bulk density from compressional velocity (V_p). Accurate estimation of formation bulk density is a significant part of reservoir characterization. Bulk density has also been found to be a very important acoustic indicator of shale (Quijada and Stewart, 2007).

Birch (1961) derived a relationship shown in equation 2.1 which had been the basis for many linear regression analyses.

$$V_p = a + b\rho \quad (2.1)$$

Where V_p is the compressional p-wave velocity in km/s and a and b are empirical constants and ρ is the bulk density in g/cc.

As previously mentioned, empirical relationships to predict the formation bulk density from compressional wave velocity have been available for several decades. This linear relationship had been found to produce reasonable estimates in volcanic and granitic rocks (Carroll 1969).

There are various ways in which density can be estimated. Apart from using waveform inversion of seismic data, density has been commonly estimated using geo-statistics whereby multi-linear regression is established between rock properties. Using a series of laboratory and controlled field measurements of brine saturated rocks which spans various depth and location in the Gulf of Mexico, Gardner et al. (1974) came up with an empirical relation between compressional wave velocity and formation bulk density.

$$\rho = A V_p^B \quad (2.2)$$

Where ρ is the formation bulk density, V_p is the compressional wave velocity, A and B are empirical constants.

This relation is found to be a good approximation for shales, sandstones and carbonates. Gardner stated that since correlations are based on field data which usually consists of some unknowns, they can only be satisfactorily applicable to

particular formations and environment. Castagna et al. (1993) however suggested that it will be more ideal using values of A and B specific to each lithology.

The original Gardner's equation for various lithology are thereby shown below.

$$\rho_{sands} = 1.66 (V_p)^{0.261} \quad (2.3)$$

$$\rho_{shales} = 1.75 (V_p)^{0.265} \quad (2.4)$$

$$\rho_{limestones} = 1.36 (V_p)^{0.386} \quad (2.5)$$

$$\rho_{dolomites} = 1.74 (V_p)^{0.252} \quad (2.6)$$

$$\rho_{anhydrites} = 2.19 (V_p)^{0.160} \quad (2.7)$$

While working with Gardner's empirical data, Lindseth (1979) developed a relationship between velocity and acoustic impedance:

$$\rho V = \frac{V - c}{d} \quad (2.8)$$

ρ is in g/cm³, V is in ft/s, c is 3460 and d is 0.308.

Lindseth work shows that rock type can be predicted from detailed velocity measurements.

Krasovsky (1981) established the differences between regression curve approximating laboratory measurements of density and velocity worldwide and regression curves approximating subsets of global data corresponding to various geological provinces around the world.

The formation bulk density estimates using Gardner's model usually fall between the clean sands and clean shales values. Gardner's model is an average of the fits for sandstones, shales, and carbonates. The Gardner's original model and its modifications to suite several lithology have been used in several sedimentary basins around the world (Dey and Stewart 1997; Potter and Stewart 1998; Potter 1999; Quijada and Stewart 2007; Nwozor et al. 2017; Akhter et al. 2018).

Christensen and Mooney (1995) suggested that a non-linear relationship between the formation bulk density and compressional wave velocity provides good estimates for crystalline rocks (equation 2.9). The values of A and B depend on the formation depths.

$$\rho_b = A + \frac{B}{v_p} \quad (2.9)$$

Brocher (2005) proposed a polynomial relationship between compressional velocity and formation bulk density for several rock types (equation 2.10).

$$\rho_b = 1.6612V_p - 0.4721V_p^2 + 0.0671V_p^3 - 0.0043V_p^4 + 0.000106V_p^5 \quad (2.10)$$

Miller & Stewart (1991) attempted to improve the accuracy of formation bulk density prediction by combining compressional and shear wave velocities using laboratory data provided by Han et al. (1986). The values of the parameters a, b, c and d can be obtained by calibrating this equation to any regional data.

$$\rho_b = aV_p^b [c + dV_s] \quad (2.11)$$

Ursenbach (2001) and Ursenbach (2002) extended Gardner's relation to include dependence on both shear and compressional wave velocity (equation 2.12). The values of the parameters A, B and C can be obtained by fitting this equation to any regional data.

$$\rho_b = C[V_p]^A [V_s]^B \quad (2.12)$$

In addition to laboratory measurements, the density-velocity relationship in lithospheric units of regional scale can be obtained directly from the velocity distribution within the lithosphere provided by large-scale seismic experiments and observed gravity data, as it was proposed by Kozlovskaya and Yliniemi (1999) and Kozlovskaya et al. (2001, 2002). This approach makes it possible to

find a density-velocity relationship that gives the best fit of the density model to the observed gravity data.

The major problems with most of the existing empirical relationships are: (1) they were developed mainly for clean formations. When applied over non-clean intervals, they tend to produce inaccurate estimates; (2) they are not applicable to rocks that contain micro-cracks/fractures. In this work, a new formation bulk density prediction method that can be applied to clean formations, non-clean formations and rocks that contain micro-cracks is developed. The new model will incorporate an additional parameter that will negate the effect of micro-cracks/fractures on compressional wave velocity.

2.2 Shear Velocity – Compressional Velocity Relation

It is common not to have shear wave velocity (V_s) data for many wells and as such V_s data will have to be estimated from compressional wave velocity (V_p) data. V_s can also be estimated from V_p for wells whereby acquired V_s data are erroneous or inconclusive. V_p/V_s , for binary mixtures were found to vary almost linearly with varying composition between the velocity ratios of the end members (Wilkens et. al., 1984). Compressional and shear velocity for quartz, dolomite, clay and calcite have been established (Birch, 1966 and Christensen,

1982). Tosaya (1982) developed empirical relation for V_p and V_s , in shaly rocks.

The work of Pickett (1963) is widely regarded as making the use of V_p/V_s ratio well known. In this work V_p/V_s ratio for sandstones, dolomites and limestones were established. Hamilton (1979) compiled in-situ measurements for shallow marine sands.

Castagna et al. (1985) established a general V_p/V_s relationship for clastic silicate rocks by comparing in-situ and laboratory data with theoretical model data. In their work, velocity information was examined for data from water-saturated mud rocks and sandstones from which general $V_p - V_s$ trends versus depth were established for Gulf Coast clastic rocks. Data scattering shows that V_p/V_s are primarily controlled by mineralogy. In-situ sonic and field measurements from this work yield a linear equation shown below.

$$V_p = 1.16V_s + 1.36 \quad (2.13)$$

The work explains the dependence of V_p/V_s on porosity and volume of clay. This equation reveals that increasing porosity or clay content increases V_p/V_s and that the velocity ratio is more sensitive to porosity changes.

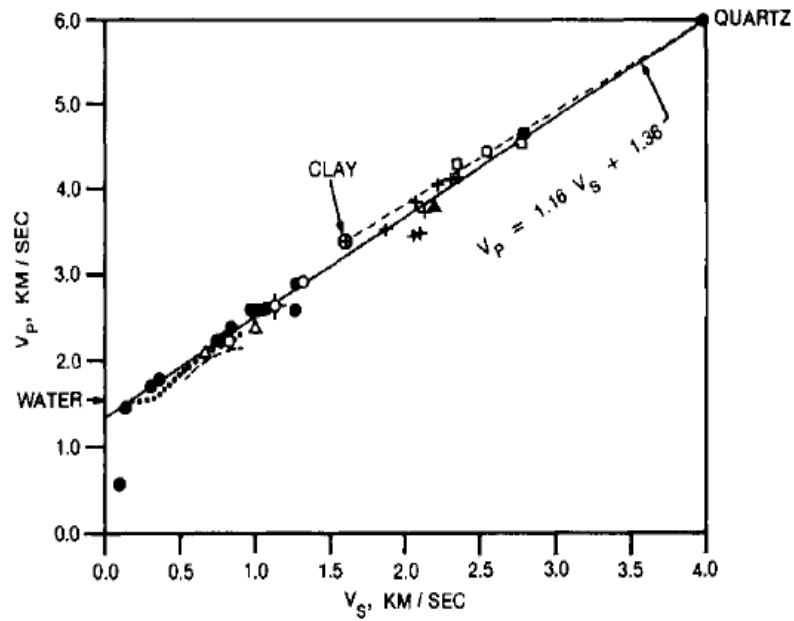


Figure 5: V_p versus V_s for different lithology (Castagna, 1985)

It was concluded that shear wave velocity is nearly linearly related to compressional wave velocity for both water saturated and dry clastic silicate sedimentary rocks. For a given V_p , mud rocks tend toward slightly higher V_p/V_s than do clean porous sandstones. For dry sandstones, V_p/V_s is nearly constant. For wet sandstones and mudstones, V_p/V_s decreases with increasing V_p .

Greenberg and Castagna (1992) developed a linear method to predict and calibrate shear wave velocity data. The calibrated equation for various lithology for the Gulf of Mexico (GOM) is below:

$$V_{S_{sands}} = 0.8041V_p - 0.8558 \quad (2.14)$$

$$V_{S_{shales}} = 0.76961V_p - 0.8673 \quad (2.15)$$

$$V_{S_{limestones}} = -0.0550V_p^2 + 1.0167V_p - 0.990 \quad (2.16)$$

$$V_{S_{dolomites}} = 0.5832V_p - 0.077 \quad (2.17)$$

Empirical porosity-depth trends can be developed for various lithology which can be used to derive density, V_p and V_s as a function of depth (Avseth et al., 2001). Avseth et al. (2008) further developed a relationship between the spatial and rock property variations as a function of depth.

It is also possible to estimate Shear wave velocity from other petro-physical data (Castagna et al. 1985; Han et al. 1986). However, it has been industry accepted standard to estimate shear wave velocity from compressional wave velocity as both are being affected by similar factors. The major limitation of the existing empirical relations is that they are both lithology and region specific.

2.3 Poisons-Ratio, Fracture Pressure and Pore Pressure

Terzaghi (1943) developed an empirical relationship which relates the pore pressure and the effective stress of the rock. The relationship has been found to be derivable analytically from 1-D compaction theory.

Using data set from Southern Louisiana and Texas Gulf Coast, Hottman and Johnson (1965) built upon Terzaghi's work and relates pore pressure, overburden stress and effective vertical stress relationship. Here, overburden pressure is taking as constant. They developed an empirical relationship between fluid pressure gradient and the electrical log properties. The authors followed this up with developing a technique using formation resistivity to estimate pore pressure.

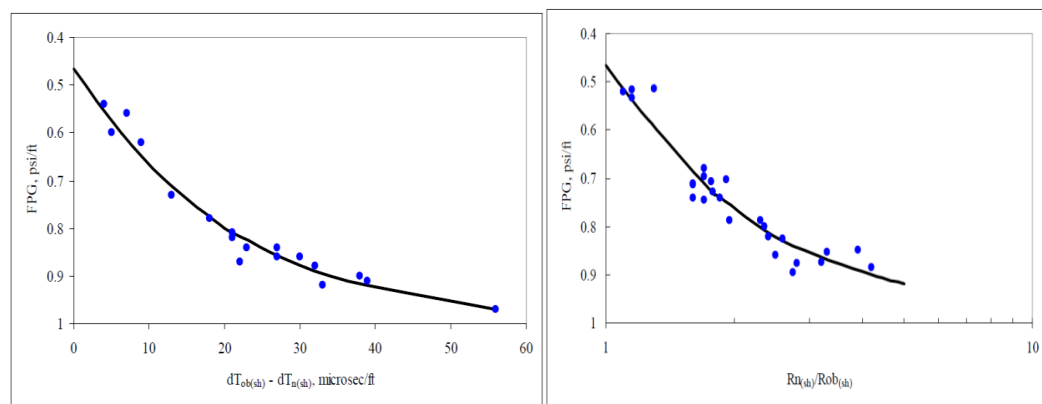


Figure 6: Relationship between Shale resistivity parameter and reservoir fluid pressure gradient pre Hottman and Johnson (Adapted from Fooshee, 2009)

Eaton (1969) intends to expand Holton and Johnson's relationship to account for the effect of overburden stress gradient. Eaton was able to prove that the overburden pressure is a function of the burial depth.

$$\sigma_{ob} = \int \rho_b dD \quad (2.18)$$

where ρ_b is the formation bulk density.

Mathews and Kelly (1967) derived fracture pressure for Louisiana and South Texas from pore pressure, vertical effective stress (VES) and stress ratio constant.

$$P_{frac} = P_{pore} + K_i VES \quad (2.19)$$

where K_i is the stress ratio, VES is the vertical effective stress which is obtained by subtracting fluid pressure from vertical stress. K_i approaches 1.0 and it varies with seabed and is based on empirical data. This equation is found to match well with intermediate well data. It however does not match the shallowest Leak Off Test (LOT). It also cannot reach the magnitude of the deepest test data as it is limited to being equal to or less than the overburden pressure.

Eaton (1969) developed an equation for fracture pressure from pore pressure, Poisson's ratio and vertical effective stress (VES).

$$P_{frac} = P_{pore} + \frac{\mu}{1 - \mu} VES \quad (2.20)$$

where μ is the Poisson's ratio which is a fraction of the horizontal strain to the vertical strain. Eaton's work gave rise to a correlation of μ increasing with depth for the GOM. Eaton and Eaton (1997) later provided same correlation for deep water. These correlations which were referenced to seabed are fully coupled and as such provide strong dependence of fracture pressure on fluid pressure.

According to Gregory (1977), Poisson's ratio is about 0.1 (corresponding to V_p/V_s of approx. 1.5) for most dry rocks and unconsolidated sands, and it is independent of pressure. The Eaton equation is however limited to never exceeding the overburden pressure.

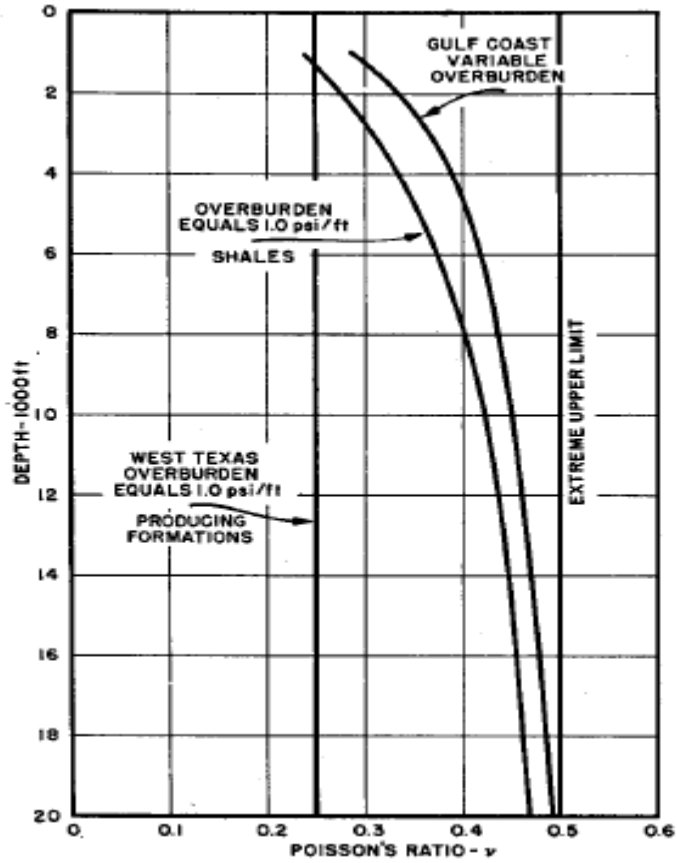


Figure 7: Variation of Poisson's ratio with depth (Eaton, 1969)

Breckles and Van Eekelen (1989) came up with power law models for fracture pressure estimation which is a function of depth range (Z) as shown in the equations below, where OP is the overburden pressure.

$$P_{frac} = (0.053 * Z^{1.145}) + (0.46 * OP) \text{ if } Z < 3500m \quad (2.21)$$

$$P_{frac} = (0.264 * Z) - 317 + (0.46 * OP) \text{ if } Z > 3500m \quad (2.22)$$

Here, the overburden on fracture pressure is not a constant. Fracture pressure rises at 0.58 psi/ft at 1600 ft to 0.76 psi/ft at 11500 ft. The power law model at $Z < 3500$ m allows fracture gradient to follow the lithostat. Using this equation, it has been found that shallow and intermediate test area are under-predicted while a good match is found in the deeper test area with allowance to exceed overburden. Hence, fracture pressure could be over-predicted.

Empirical data compiled by Daines (1982) added a tectonic stress variable to the Eaton equation as shown below.

$$P_{frac} = \Phi_t + P_{pore} + \frac{\mu}{1 - \mu} VES \quad (2.23)$$

Φ_t is derived using fracture pressure and then re-arranging the formula. Φ_t is proportional to VES at all depths if the strata remain horizontal and the basin structures do not vary significantly with depth. This equation is found to match better in the shallow and intermediate test area.

Bourgoyne et al. (1996) explained that overpressure can be generated by various mechanisms which include compaction, diagenesis, differential density and fluid migration with compaction being the most common of these mechanisms.

Ikon Science (2010) developed a fracture pressure formula which attempts to incorporate more variables.

$$P_{fract} = 14.6 + (WG * WD) + (\% \text{ of } S_v * Z_{ml}) + (A * OP) \quad (2.24)$$

Where WG is water gradient, WD is water depth, S_v is overburden, Z_{ml} is the depth below mudline, A is the pore-pressure, fracture-pressure coupling ratio and OP is the formation overpressure.

2.4 Excess Pressure Methodology

2.4.1 Excess Pressure Concept

In order to better understand the geologic formations penetrated by a drilled hole, a Well Log which consists of the detailed record of the penetrated geologic formations is required. Logging is performed by lowering a specialized tool with sensors attached to the end of a wireline into a drilled well from which a record of the petrophysical properties is obtained. The petrophysical data are analyzed and plotted as a function of well bore depth. The output of these analyses is an important variable in estimating hydrocarbon in-place and booking reserves. In most cases, a combination of Logs such as Gamma ray, Neutron-Density and Resistivity is used.

Pressures are usually expressed in terms of pressure gradient which is the change in pressure over a given depth interval. The hydrostatic pressures are usually

expressed in terms of a pressure gradient and have the value of 0.433 psi/ft for freshwater and 0.448 psi/ft for seawater. Typical wireline formation testing tools include RFT, SFTT, MDT and RDT. During pressure test, the tool is lowered in the hole in the zone of interest. The tools are equipped with a rubber pack and back-up arms which are hydraulically forced against the formation to provide seal from the wellbore fluids. The pretests are automatically activated in sequence from which the formation build up pressure is monitored and recorded.

The term Excess Pressure (EP) is the left-over pressure after subtracting sub-surface fluid weights from the total sub-surface pressure. With the Excess Pressure technique, effects of a chosen fluid density is removed which in-turn improves the visualization of subtle fluid density differences and/or the presence of a pressure barrier.

Fluid densities of oil and water can have similar densities from P-D plots which make them difficult to be identified since they appear almost parallel. The Excess Pressure methodology makes it easy for these small fluid density differences to be easily identified. The assumed density is iterated until it equalizes pressure at the depth interval of interest, as well as excess pressure variance is minimized and the excess-pressure trend is vertical. Also, P-D plots can have very large pressure ranges which make them not able to take advantage

of the high resolution of modern pressure gauges. Excess pressure plots are able to zoom in about ten times on the data of interest. As well, by removing the effects of weight of static fluid, pressure differences are enhanced, making it capable of resolving small density changes and pressure barriers that are not likely to be observed on standard P-D plots. A possible barrier can be identified by excess pressure variations with depth. If a possible barrier is identified, the depth range of analyzed samples is narrowed so that only a single fluid is evaluated (Brown, 2003).

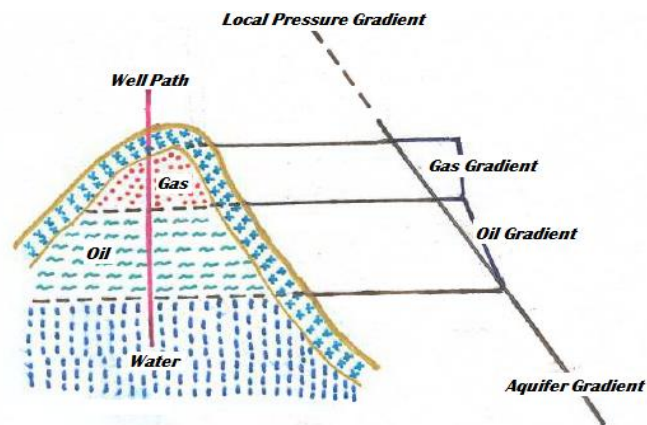


Figure 8: Fluid Contacts and Gradients in an Ideal Reservoir

In terms of resolution, P-D plot is unable to accurately differentiate between Free Water Level (FWL) and Hydrocarbon Water Contacts (HWC). The interesting thing about the FWL is that it is the meeting point of water and hydrocarbon and at that elevation, the pressure of water and hydrocarbon are

the same. This makes interpretation complicated. The difference in HWC elevation and FWL indicates whether the reservoir is hydrocarbon-wet or water-wet. Excess pressure plots can also be useful in evaluating the connectivity of the reservoir as well as to know whether or not they are divided into compartments. The pressure and density differences can then be identified.

2.4.2 Subsurface Pressure Barriers

A Fluid Contact in a reservoir is the interface which separates fluids with different densities. These interfaces are often assumed to be horizontal for simpler analytical purposes, however they are practically not; the contacts between fluids are often at an angle. The fluids separated are usually not a single entity, and there exists a Transition Zone (TZ) before contacts, made up of a movement of fluids. The TZ are fluid contacts intervals where the fluids co-exist. These fluids consist of gas, oil and water descending from depth, where gas has the lightest density, then oil and finally water. The contact between the gas and oil is called the Gas Oil Contact (GOC) and the contact between oil and water is the Oil Water Contact (OWC). Figure 9 shows the schematic of an ideal subsurface geo-pressure system.

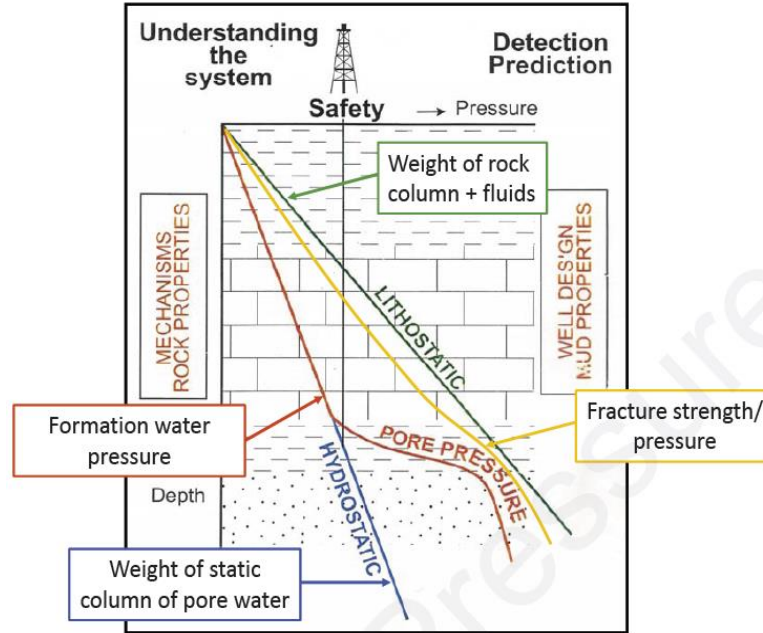


Figure 9: Subsurface Geo-pressure System (Green, 2012)

As explained earlier, all of these contacts can be easily depicted on an EP plot. As can be seen below from the EP plot in Figure 10, the vertical trend line represents the slope of the oil line. The water line is represented by the angled slope line. The depth after the last oil point and before the first water point is considered the OWC. The depth at which vertical oil trend line intersects the water trend line is considered the FWL.

The EP plot makes it easy to be able to distinguish the FWL from the OWC. This effect can be used to estimate reservoir wettability. Wettability of a reservoir refers to the preference of a solid to contact one liquid or gas, rather

than the other. Rocks can be water-wet, oil-wet or intermediate-wet, which relates to the adhesive properties of the fluid to the rock. Wettability affects relative permeability, electrical properties, nuclear magnetic resonance relaxation times and saturation profiles in the reservoir.

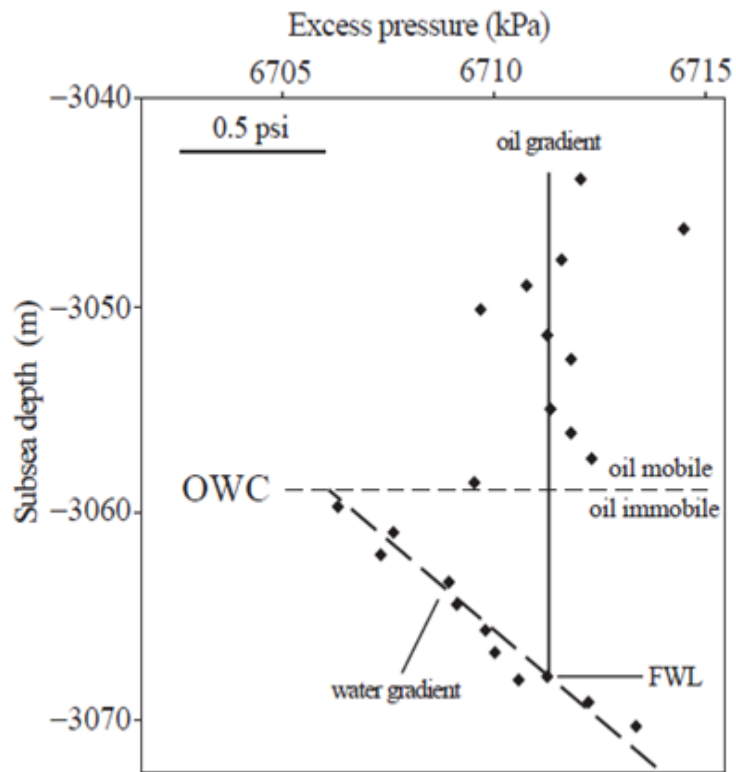


Figure 10: Excess Pressure derived from Fluid Density (Brown, 2003)

Collected data from a wireline pressure test consist of pressure points P vs. true vertical depth (TVD), h . The interest is to start by identifying a fluid density that equalizes the EP of the fluid of interest at all depths. This is an iterative

process carried out until the plot is a vertical line for the fluid of interest. The fluid density that resulted in obtaining the vertical line is used to calculate the Assumed Pressure. The difference between the Assumed Pressure and the Total Pressure from the collected data gives the Excess Pressure, which is then plotted against the TVD, ensuring that the units are consistent all through. The resulting EP plots are then evaluated and analyzed for fluid contacts, densities and pressure barriers.

$$P_a = \rho \cdot g \cdot h \quad (2.25)$$

$$P_{ex} = P_a - P_{fm} \quad (2.26)$$

where P_{ex} is the Excess Pressure, P_a is the Assumed Pressure, P_{fm} is the Formation Pressure, ρ is the Fluid Density, g is the Gravity, h is the True Vertical Depth.

2.5 Geology of the Grand Banks

The Grand Bank is the largest of the six banks on the Newfoundland and Labrador continental shelf collectively referred to as the Grand Banks (Sonnichsen and King, 2005). It is an area of approximately 100,000 square-kilometers which comprises of the eastern and southern-most portion of the

Grand Banks. Flemish Pass with depths greater than 1000 m separates the Grand Bank from the Flemish Cap. The sedimentary basins which are Mesozoic as shown in figure 11 represents failed rifts related to the opening of the present Atlantic Ocean (Enachescu, 1987). These rifts were initiated during the Late Triassic-Early Jurassic in response to the rifting between North America and Africa which began to drift apart in the Early Jurassic. The drifting was temporarily stopped at the Newfoundland Transform Zone south of the Grand Banks. The rift axis moved to the east of the Grand Banks and Iberia separated from the Grand Banks in Early Cretaceous. The rest of Europe separated from Grand Banks in Middle to Late Cretaceous and rifting propagated to the Labrador Sea (DeSilva, 1999).

The most prolific basin in the Grand Banks to date is the shallow-water Jeanne D'Arc Basin which is where all the four current offshore developments in this region are based. The water depth in the Jeanne D'Arc basin ranges from 90 m to 120 m. Recent exploration work is leading to significant discovery in the Flemish Pass Basin which is expected to see its first development soon.

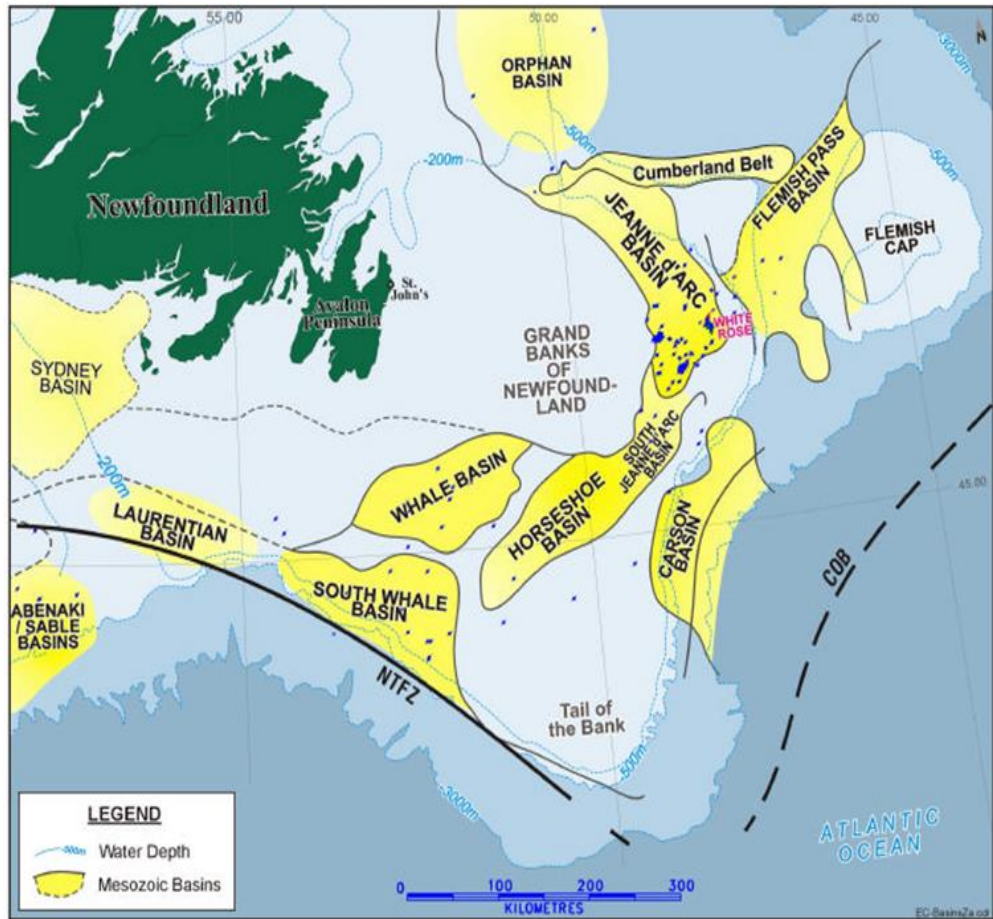


Figure 11: Sedimentary Basins in the Grand Banks (Whiterose DA Volume 2, 2001)

2.5.1 Jeanne d'Arc Basin

The Jeanne d'Arc Basin is bounded to the east by Ridge complex and to the west by the Bonavista Platform. It has the Avalon uplift to the south and it is open to the north linking it to the Orphan basin. All of the four producing

fields to date (Hebron, Hibernia, Terra Nova and White Rose) are housed in this basin.

Enachescu (1987) and McAlpine (1990) have extensively discussed the stratigraphy of the Jeanne d'Arc Basin. The major source rock in this basin is the Kimmeridgian which is an Egret member. Generally, the oil within the basin is sweet with an API generally greater than 30 except for the recently developed Hebron field which is a little heavier with an API of 21 degrees. Figure 12 shows the lithostratigraphy of the Jeanne D'Arc basin.

2.5.2 Flemish Pass Basin

The few wells drilled in the Flemish Pass basin to date have shown the presence of source rocks and reservoirs. This basin is in deeper water with a water depth of approximately 1000 m. The play type consists of rollover anticlines and tilted fault blocks. Source rock made up of Egret member and reservoirs equivalent to Hibernia and Jeanne d'Arc sandstones have been encountered.

A cross section along the axis of the Jeanne d'Arc Basin illustrates the presence of stacked sandstone reservoirs throughout the basin and the principal trapping mechanism associated with normal faults that trend SE across the basin. (NL Government Report, 2000). Discussions relating to the development of the Bay Du Nord field in this basin are currently in progress.

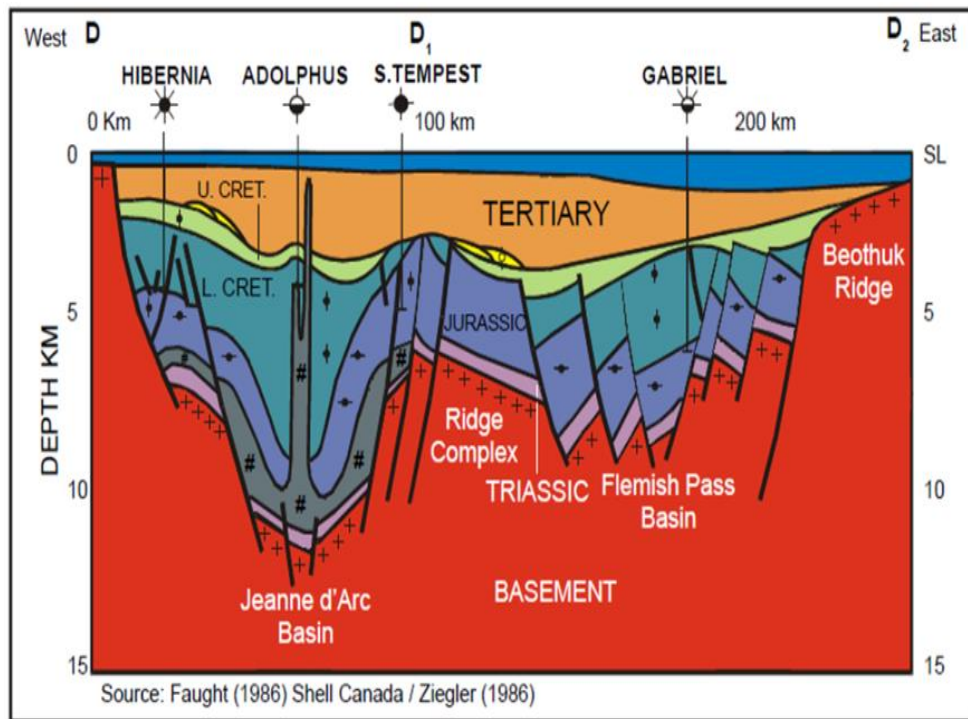


Figure 13: Schematic Cross Section based on seismic line (NL Department of Mines and Energy, 2000)

2.5.3 Other Sedimentary Basins

Many of the other sedimentary basins in the Grand bank are recently discovered through ongoing exploration work. The other sedimentary basins in the Grand banks, though, have been drilled but haven't resulted in any significant discovery to date. These basins include Orphan, Carson, Horseshoe, Whale, South Whale and Laurentian.

2.6 Geology of the Niger Delta

The geology of the Niger Delta Basin had been well studied in previous literatures (Short and Stauble, 1967; Evamy et. al, 1978; Ejedawe, 1981; Knox and Omatsola, 1989; Doust and Omatsola, 1990). It is situated in the Gulf of Guinea in equatorial West Africa, between latitudes 3-degrees N and 6-degrees N and longitudes 5-degrees E and 8-degrees E (Reijers et al, 1996). The Niger Delta is bounded on the northwest by a subsurface continuation of the West African Shield, the Benin Flank. The eastern edge of the basin coincides with the Calabar Flank to the south of the Oban Masif (Murat, 1972).

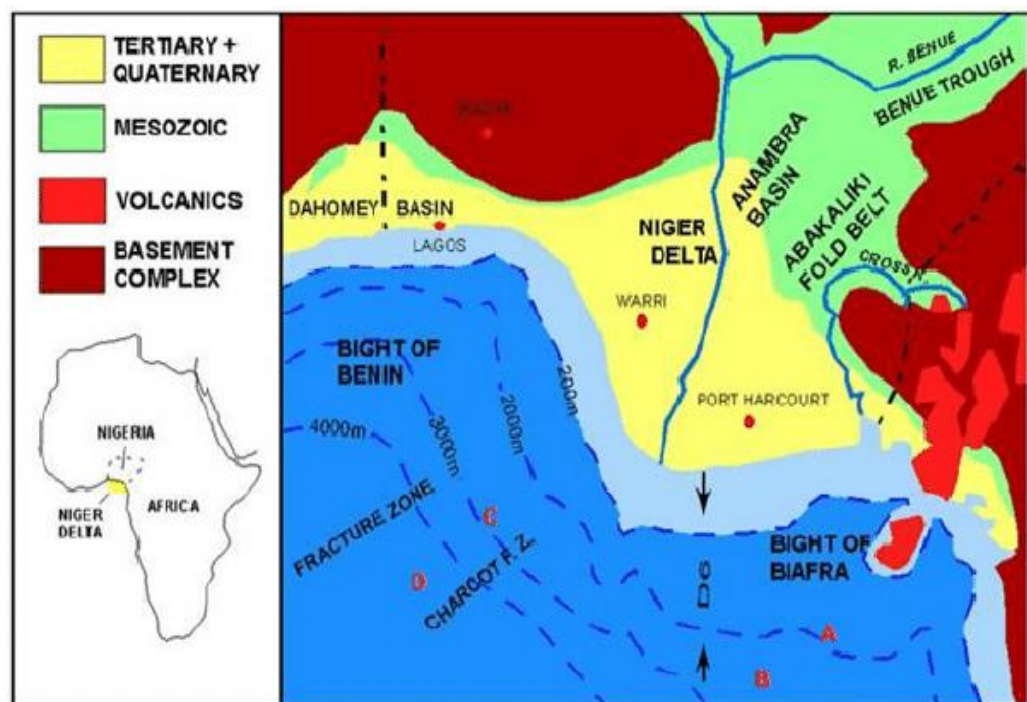


Figure 14: Geologic Map of the Niger Delta (Ajayi and Okosun, 2014)

Well sections through the Niger Delta generally display three vertical lithostratigraphic subdivisions: an upper delta top facies; a middle delta front lithofacies; and a lower pro-delta lithofacies (Reijers et al, 1996). The Niger Delta Basin is divided into three gross lithofacies: (a) marine claystones and shales of unknown thickness, at the base; (b) alternation of sandstones, siltstones and claystones, in which the sand percentage increases upwards; (c) alluvial sands, at the top (Doust 1990). These range from the oldest to the youngest, the Akata, Agbada and Benin formations all of which are strongly diachronous. These three major lithofacies are usually distinguished by their sand–shale proportion. It is known to cover a surface area of over 100,000 square-kilometers and is composed of an overall regressive clastic sequence that is as much as 12 kilometres in thickness (Nwozor et. al, 2017).

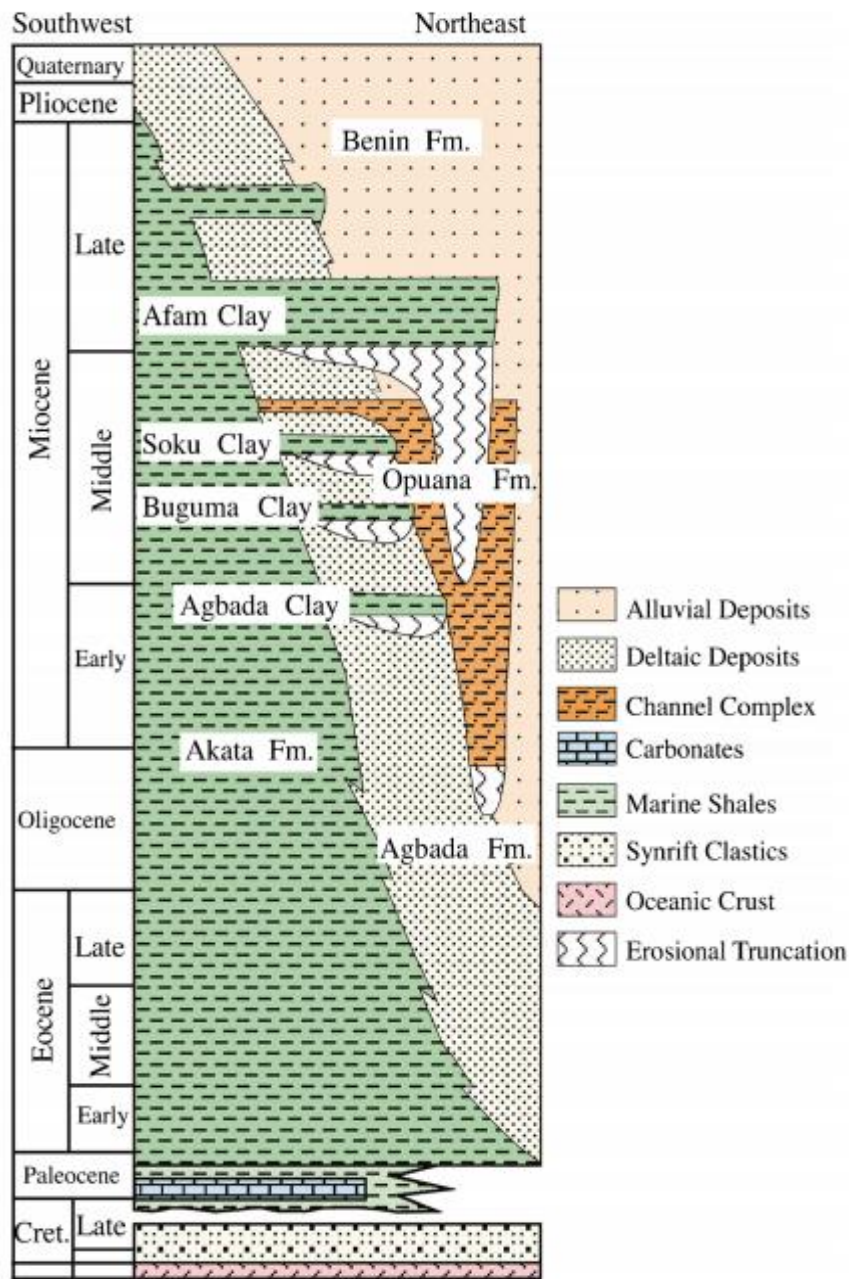


Figure 15: Stratigraphy Column of the Niger Delta.

2.7 Chapter Summary

The chapter provides an insight into efforts made in the past to develop and improve elastic properties correlation to aid efficient well planning and for effective subsurface characterization. It summarizes the elastic properties correlations applied to petroleum exploration. It emphasizes on the fact that most of these correlations are region-specific which make their application to fields in other regions produce erroneous results in many cases. This has often thrown up questions to their general applicability. The chapter reviewed past studies of fracture pressure correlation and its determination from Poisson's ratio as well as pore pressure correlations. The chapter introduced and explored the concept of Excess Pressure (EP) relative to fluid density which is used to interpret fluid contacts and evaluate reservoir compartments.

Chapter 3

Prior Bulk Density Model Calibration

3.1 Bulk Density from Compressional Velocity

Accurate estimation of formation bulk density is a significant part of reservoir characterization and field development. Bulk density have been found to be a better differentiator of hydrocarbon rocks from other rock types as well as to be a very important acoustic indicator of shale.

It is a common practice to have the Gardner et al. model adapted directly to estimate formation bulk density for wells. The Gardner model was derived and found to work specifically well for the Gulf of Mexico. Some studies done for wells located offshore Grand Banks have shown that the Gardner equation failed to predict density accurately in a combination of sand and shaly formations. This chapter attempts to calibrate the Gardner et al. model in order to evaluate its' applicability to the region under study. The chapter elaborates the steps taken to calibrate the Gardner equations in deriving coefficients that could possibly be applied to wells drilled offshore Grand Banks for bulk density estimation in sands and shales.

3.1.1 Data Quality Control

Data from various wells were analyzed. Among few wells data available, the ones which met the requirements of this research objectives were selected and analyzed. Separating high quality data from noise is essential in successful data analyses and conclusions. In order to identify and remove noise data, the bulk density correction (dRho) was looked at to identify very high negative or positive corrections which could be indicative of low data quality. More so, since elastic sonic logs are affected by borehole quality, the caliper log (dCal) was monitored to identify if the hole size is smaller possibly due to buildup of mud cake or bigger possibly due to caving. Since the measurement depth of the density log is shallow in some cases, mud filtrate invasion effect was monitored using resistivity logs as this could affect the measurement.

3.1.2 Lithology Separation

For the purpose of our analyses, there is need to create a cut-off for differentiating lithology. From the Gamma Ray in certain instances, it is generally observed that shale is the dominant lithology from the stratigraphic column with interbedded sandstones for the wells. This was used as lithology

differentiator which enables the estimation of values for the constants A and B in the Gardner equation. For lithology separation, Gamma Ray cut-off values are treated differently on a well-by-well basis.

3.2 RhoB – V_p Relation

A well with very good sonic data, gamma ray data and resistivity data was selected as the calibrating well for this section. The calibrating well is further quality-controlled as described above. Using the lithology separation, sand is separated from shale and a plot of compressional wave velocity and formation bulk density was made from which a power law model fit was established. After this was established, the coefficients from the power law model was taken back to fit the density values from the log to the measured data.

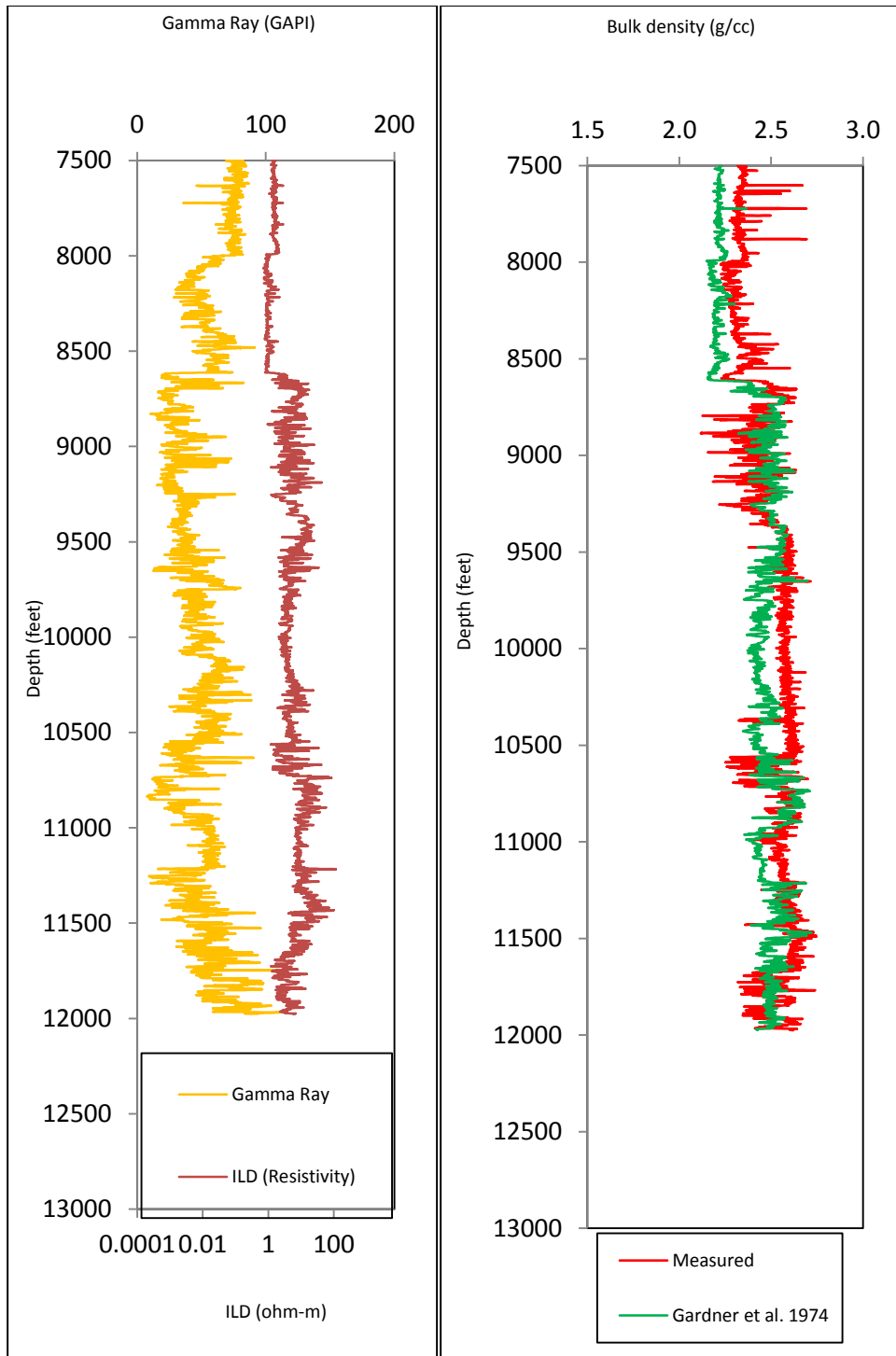


Figure 16: Calibrating Well GB1 - Measured and Gardner Model comparison with GR and Resistivity logs

Figure 16 shows how the Gardner model predicted the formation bulk density for the calibrating well. The gamma and resistivity logs also enable us to view and differentiate sections of the well which can be classified as sand and sections of the well which are categorized as shale. As such, we are able to view how the Gardner model prediction behaves for sandy and shaly formations.

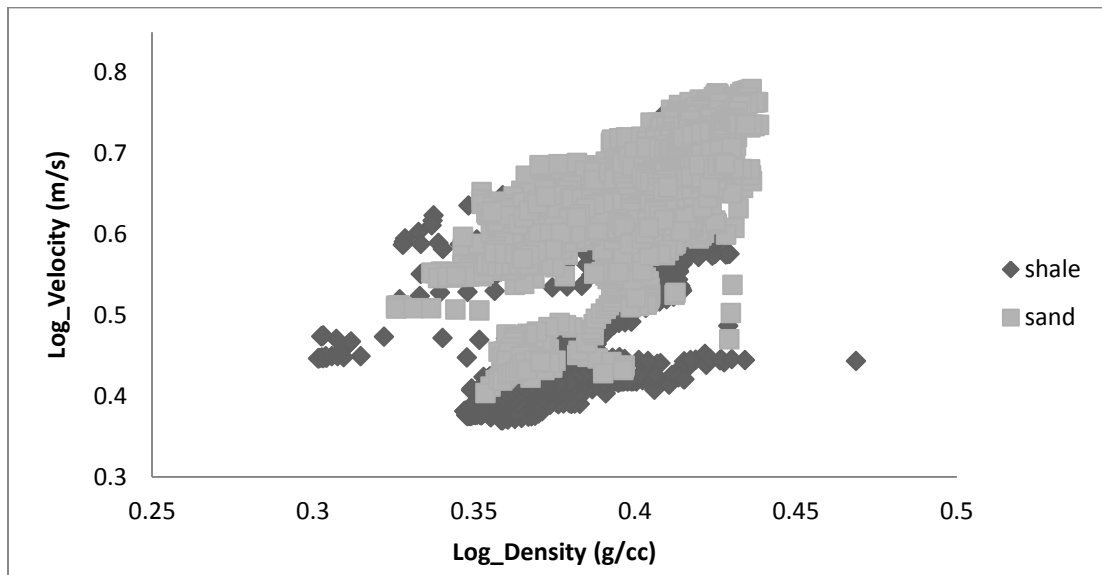


Figure 17: Distinct Sand and Shale on a Density-Velocity Log Plot for a Grand Bank well

Figure 17 is a plot of the logarithm of density and the logarithm of velocity. This provides the understanding that wells in this area are prone to have formations which are not purely sand nor shale but could be classified as shaly-sand, making prediction of the formation bulk density much more tricky.

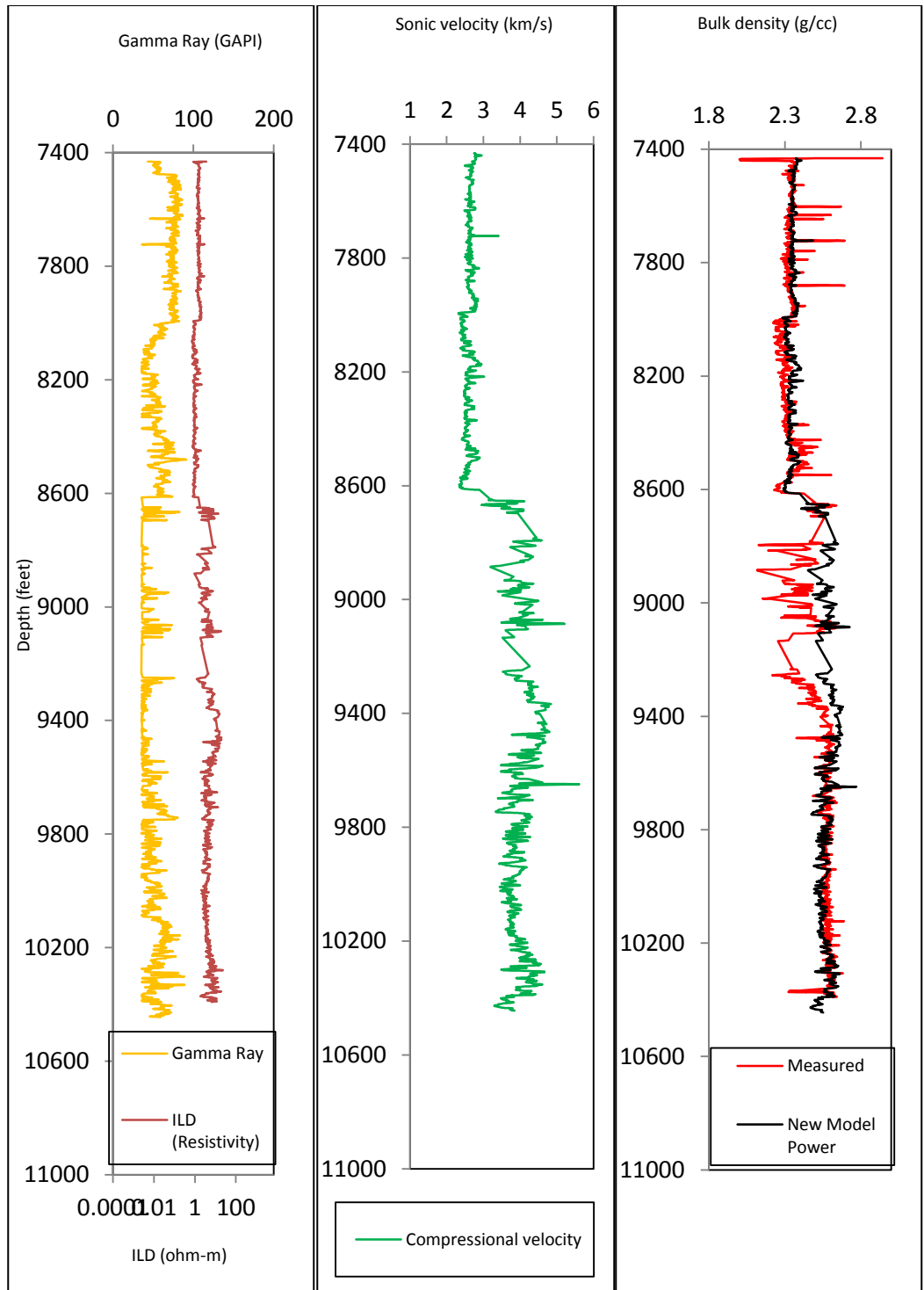


Figure 18: Shale Calibration from the Calibrating Well GB1 with GR and Resistivity logs

Since the Gardner model could not predict the formation bulk density well in a shaly-sand region, an algorithm was created to separate the sandy formations from the shaly formations, from which two separate Gardner-type models could be developed with different coefficients for sands and shales.

As can be seen from figure 16 above, there is a discrepancy between the measured density and that predicted by Gardner. Attempt was made to separate sand and shale intervals in order to be able to effectively derive the values of constants A and B needed for sand and shale density prediction. Shale and sand were filtered as discussed in the lithology separation. Using least squares method, fitting coefficients (A and B) were derived for both the sand and shale intervals.

Figure 18, which depicts the shale calibration, shows results of calibration done for the different shale intervals. Noticeably, very good match were found in the clearly identified shale intervals (7500-8000 ft and 8500-8580 ft). Sections with different shale stringers also show very good match. Figure 19 also displays measured versus estimated density values as well as the deviation from normal plot which, as can be seen is reliable with bulk of the readings at the zero mark. Similar analysis goes for the sand intervals from figure 20 which shows the bulk density match and figure 21 which shows the measured versus estimated density

plots as well as the deviation plot. It should be noted that all acquired data from this well were utilized in developing the calibration.

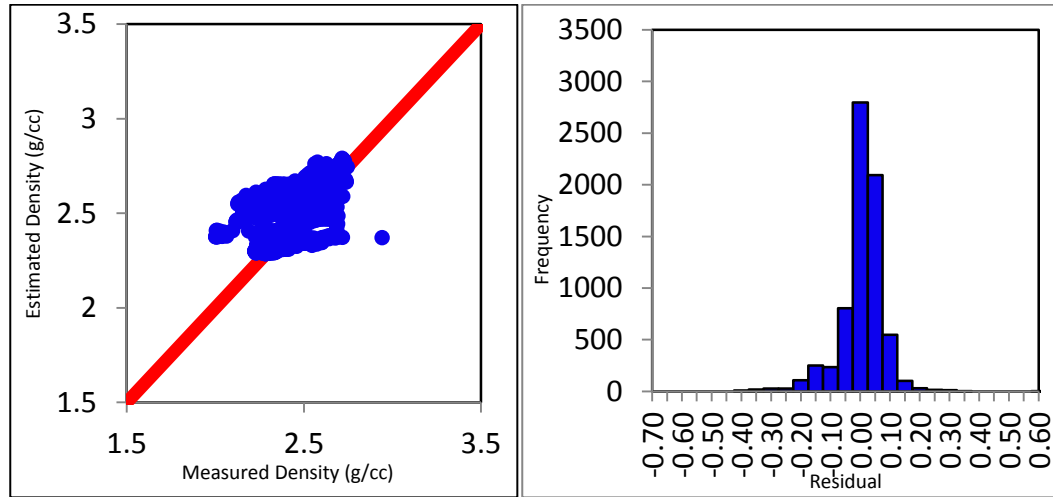


Figure 19: Comparison of estimated and measured (log) p-wave wave velocities for well GB1 Shale Interval

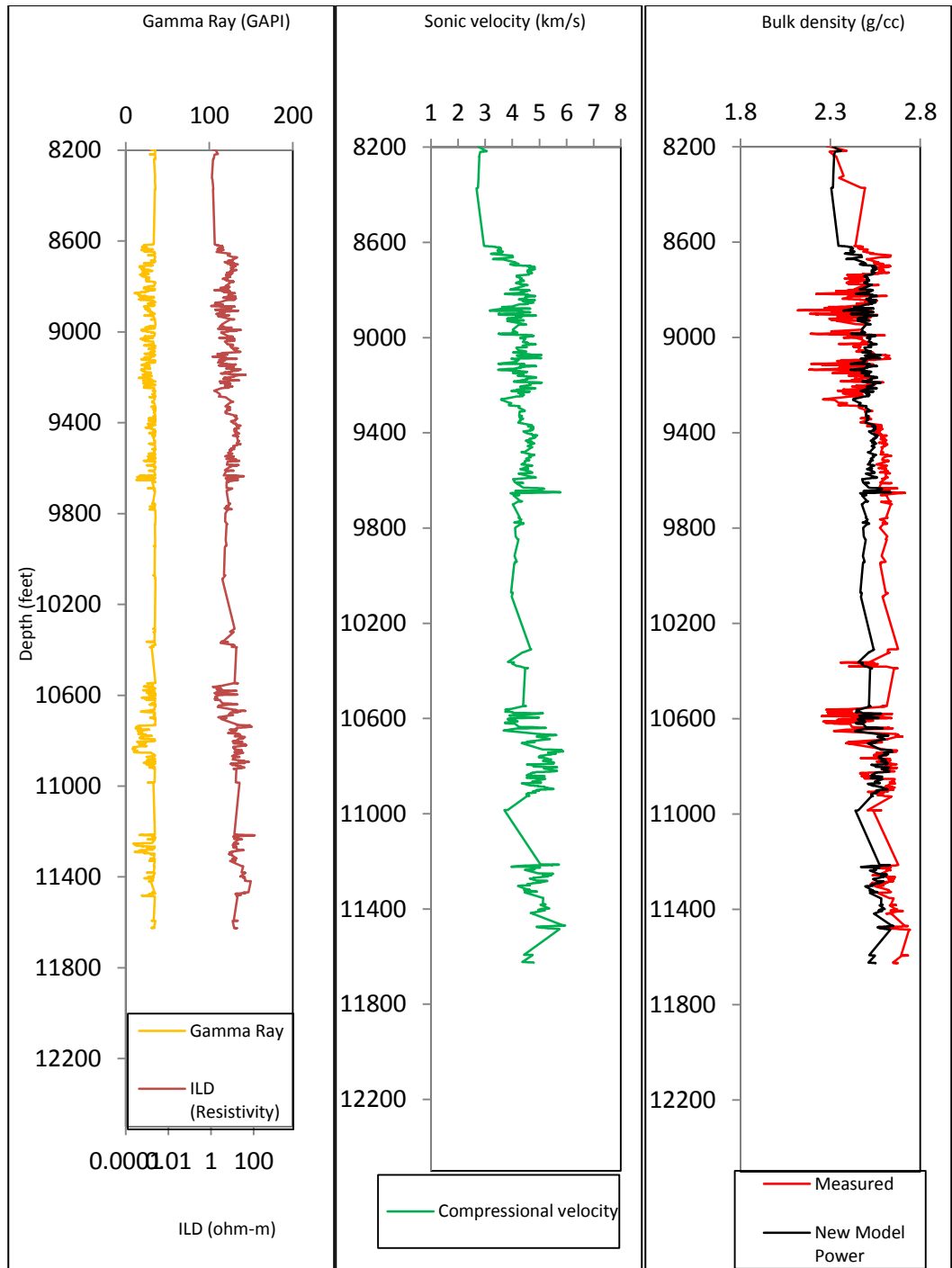


Figure 20: Sand Calibration from the Calibrating Well GB1 with GR and Resistivity logs

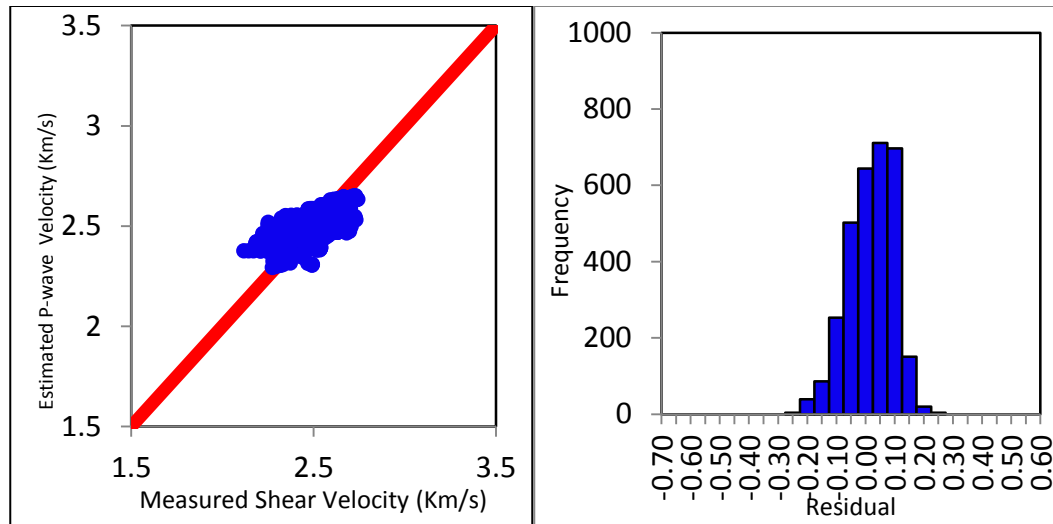


Figure 21 : Comparison of estimated and measured (log) p-wave wave velocities for well AA Sand Interval

The resulting Gardner-type equation for sand and shale are shown below:

Calibrated Sand Equation:

$$\rho = 1.907 V_p^{0.184} \quad (3.1)$$

Calibrated Shale Equation:

$$\rho = 1.9035 V_p^{0.2095} \quad (3.2)$$

3.3 Discussion of Calibration Methodology

The coefficient of determination (R-square) and the RMSE for the calibrated models and the original Gardner model are listed in the tables 1 and 2.

Table 1: RMSE Comparison - Calibrated Model and Gardner Model

RMSE (%)		
	Shale Section	Sand Section
Gardner et.al	0.123136	0.077561
Calibrated Models	0.074799	0.07698

Table 1 above displays the Root Mean Square Error (RMSE) for the original Gardner equations and for the calibrated equations for the Grand Banks well. The calibrated equations were found to predict the sand and shale intervals better than the original Gardner equation. Table 2 shown below displays the R-Square values of the calibrated equations for sand and shale intervals. This value is found to be very good for the shale but somewhat average for the sand intervals even though it is generally better suited for the Grand Banks as compared to the original Gardner models. This prompted the question of the short-comings of Gardner et al. models for predicting formation bulk density in this area.

Table 2: R-squared Comparison - Calibrated Models: Sand and Shale

	R²
Calibrated Model – Shale Section	0.842
Calibrated Model – Sand Section	0.546

The shortcoming of this calibrated model approach is the fact that it probably has to be repeated for every geologic area within a single basin if there are wide variations in the geology from one end of the basin to the other, which is very typical for this area. This prompted the need to develop a more comprehensive single model applicable to varying lithology and varying depth. The next chapter dealt with this problem by taking mixed lithology and micro-cracks into account.

3.4 Chapter Summary

The chapter attempts to show some of the limitations of the prior formation bulk density prediction models. Since the Garner et al. model does not provide a satisfactory formation bulk density prediction along the length of the well column, a calibrated form of the equation was derived for sand and shale sections. Although the calibrated models are fairly good in predicting formation bulk density for sand and shale separately, they will not be able to predict bulk density in mixed lithology which is a typical occurrence in this area.

Chapter 4

A New Formation Bulk Density Model

4.1 The New Formation Bulk Density Prediction Technique

Part of this chapter had been published. As previously explained, the formation bulk density is one of the most important rock properties required for subsurface evaluation during the exploration, drilling and production phases of a field development. In reservoirs where the formation bulk density logs are not acquired, the current practice is to estimate the formation bulk density from the compressional wave velocity. Several empirical relationships have been developed to estimate the formation bulk density from the compressional wave velocity but these relations have shortcomings as explained in previous sections. Two new model development approaches, Model Method 1 and Model Method 2 are presented. In this chapter, the training data set are different from the validating data set.

4.2 Model Method 1 Development

Laboratory investigations by Tosaya (1982), Tosaya and Nur (1982), Kowallis et al. (1984), Castagna et al. (1985) and Han et al. (1986) have shown that Shear and compressional wave velocities can be expressed as functions of formation effective porosity (\emptyset) and clay volume (V_{sh}) as presented in Equations 4.1 and 4.2, where A, B, C, X, Y and Z are regression coefficients.

$$V_p = A - B\emptyset - CV_{sh} \quad (4.1)$$

$$V_s = X - Y\emptyset - ZV_{sh} \quad (4.2)$$

Although the regression coefficients vary from one author to another, they generally follow the same trend. Equations 4.1 and 4.2 are then combined to produce Equation 4.3, where Q, R and D are new set of constant parameters.

$$V_s = QV_p + R\emptyset - D \quad (4.3)$$

For liquid-filled shaly sand formations, effective porosity can be expressed as functions of formation bulk density, sand matrix density, shale matrix density, saturating fluid density and shale volume fraction (Equation 4.4).

$$\emptyset = \left[\frac{\rho_{ma}}{\rho_{ma} - \rho_{fl}} \right] - \left[\frac{1}{\rho_{ma} - \rho_{fl}} \right] \rho_b - \left[\frac{\rho_{ma} - \rho_{sh}}{\rho_{ma} - \rho_{fl}} \right] V_{sh} \quad (4.4)$$

Equation 4.4 then reduces to equation 4.5 below by simplification:

$$\emptyset = A - X\rho_b - CV_{sh} \quad (4.5)$$

Substituting equation 4.5 into equation 4.3 and solving for density gives equation 4.6 shown below which is the newly proposed formation bulk density prediction relation which incorporates mixed-lithology.

$$\rho_b = AV_P - BV_s + CV_{sh} + D \quad (4.6)$$

4.2.1 Model Method 1 Calibration

Using the Least Square Method, the model is calibrated using laboratory data from Han et al. (1986) at 5, 10, 20 and 30 MPa compressive stresses. Figures 22 to 25 detailed the result from the calibration of the new model using these sets of laboratory data. The left hand side plot of each figure shows the predicted formation bulk density plotted against the measured formation bulk density

values while also displaying the R-square values. The right hand side plots highlights residual error ranges.

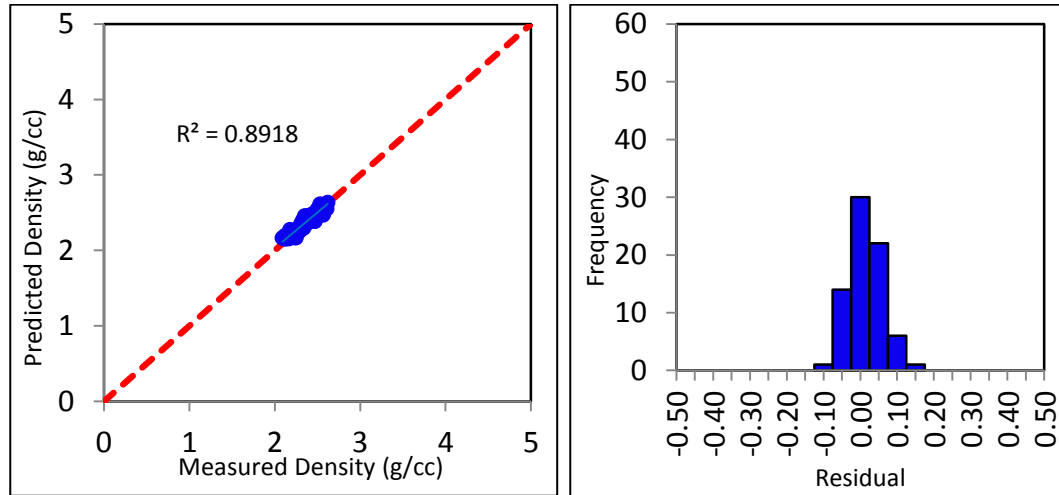


Figure 22: New Density Prediction Model Calibration using Hans et. al. Laboratory data at 5 MPa

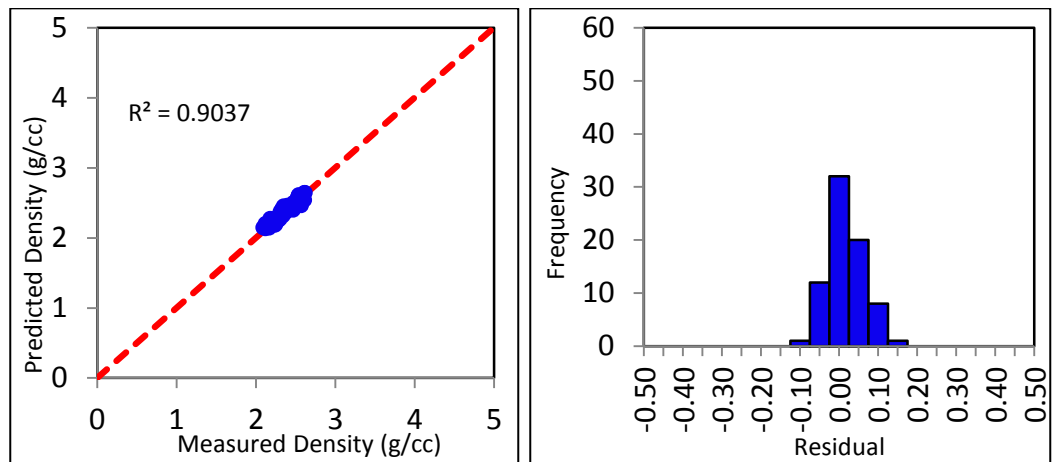


Figure 23: New Density Prediction Model Calibration using Hans et. al. Laboratory data at 10 MPa

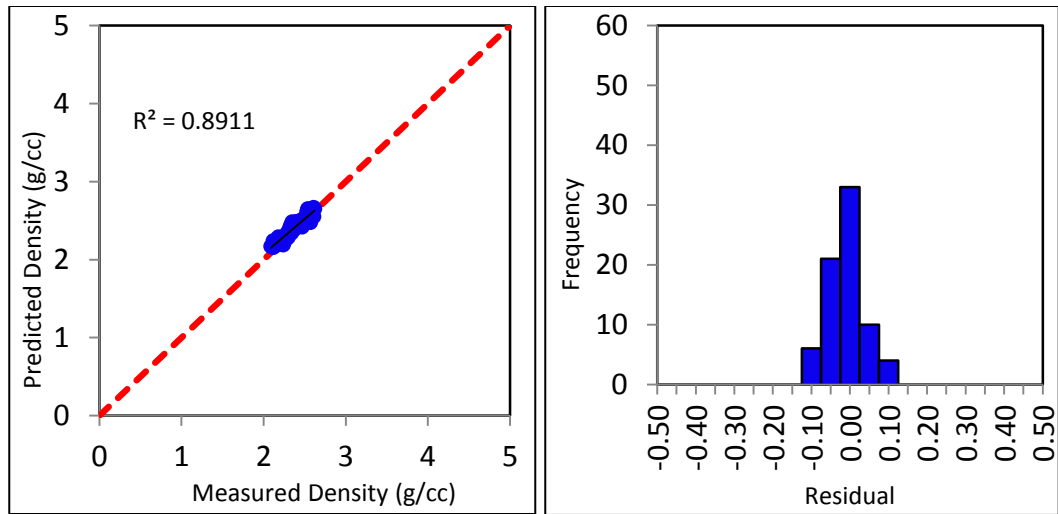


Figure 24: New Density Prediction Model Calibration using Hans et. al. Laboratory data at 20 MPa

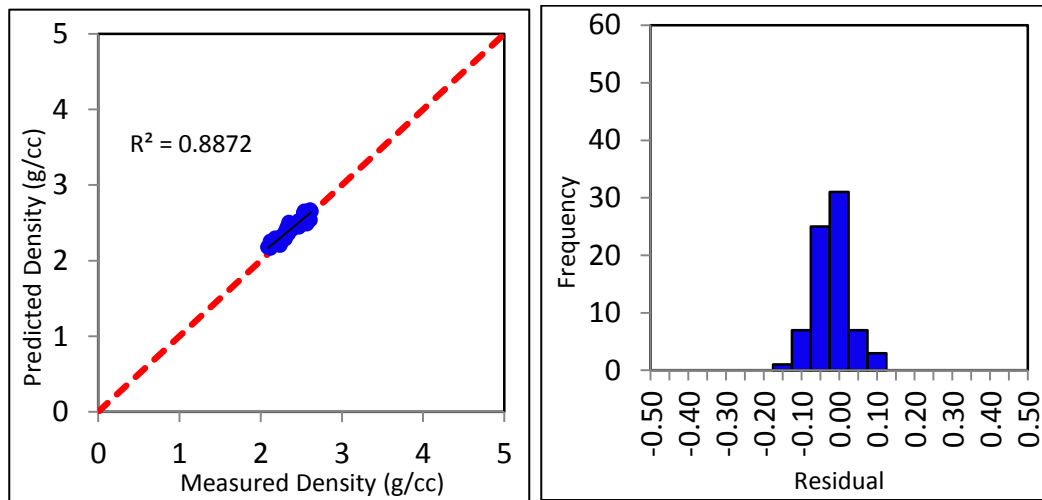


Figure 25: New Density Prediction Model Calibration using Hans et. al. Laboratory data at 30 MPa

In all four model calibration plots, it can be observed that the predicted formation bulk density values match the measured bulk density values very well with reasonably high coefficient of determination values in all instances. Also, the residual error in the four compressive stress instances is within $\pm 10\%$ which is a very acceptable range with bulk of the data falling on zero in all cases.

Using Han's laboratory experimental results with compressive strength of 5, 10, 20, 30 MPa, the resultant new density prediction equation which is a function of the compressional wave velocity, shear wave velocity and volume of shale is given by equation 4.7 below.

$$\rho_b = 0.38V_p - 0.21V_s + 0.5V_{sh} + 1.28 \quad (4.7)$$

4.2.2 Validation of the Model Method 1

In order to validate the model, the same set of laboratory data used in calibrating this model (Han et. al, 1986) were also applied to the Gardner et. al. (1974) density prediction model at the same compressive stresses of 5, 10, 20 and 30 MPa. Figures 26 to 29 display the measured versus predicted density and the residual error ranges.

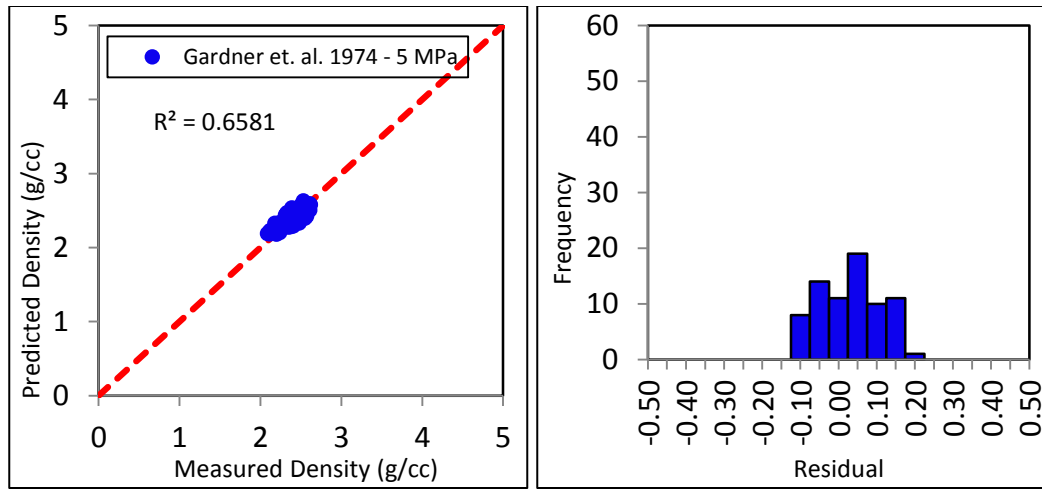


Figure 26: Gardner et al. Model for density prediction using Hans et al. Laboratory data at 5 MPa

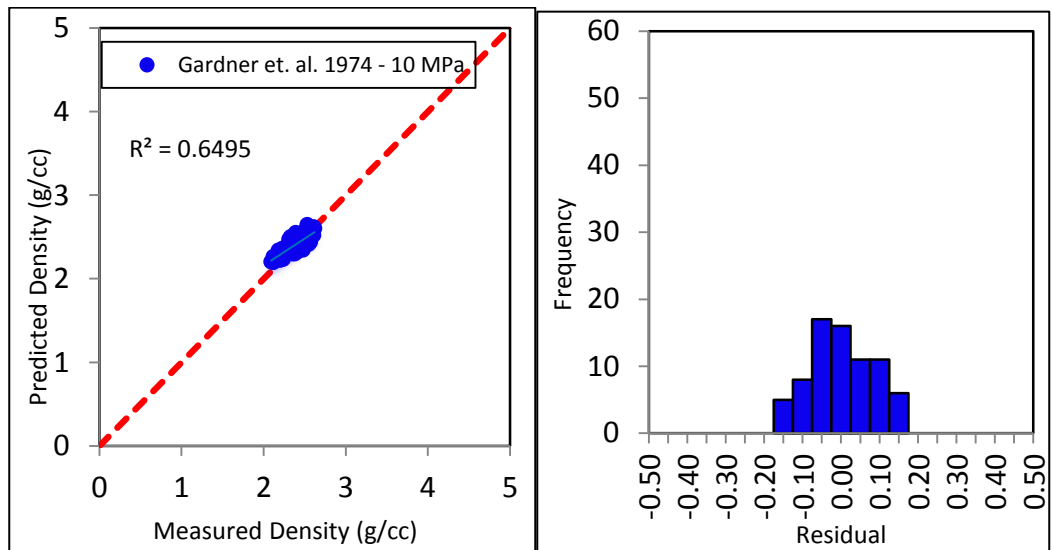


Figure 27: Gardner et al. Model for density prediction using Hans et al. Laboratory data at 10 MPa

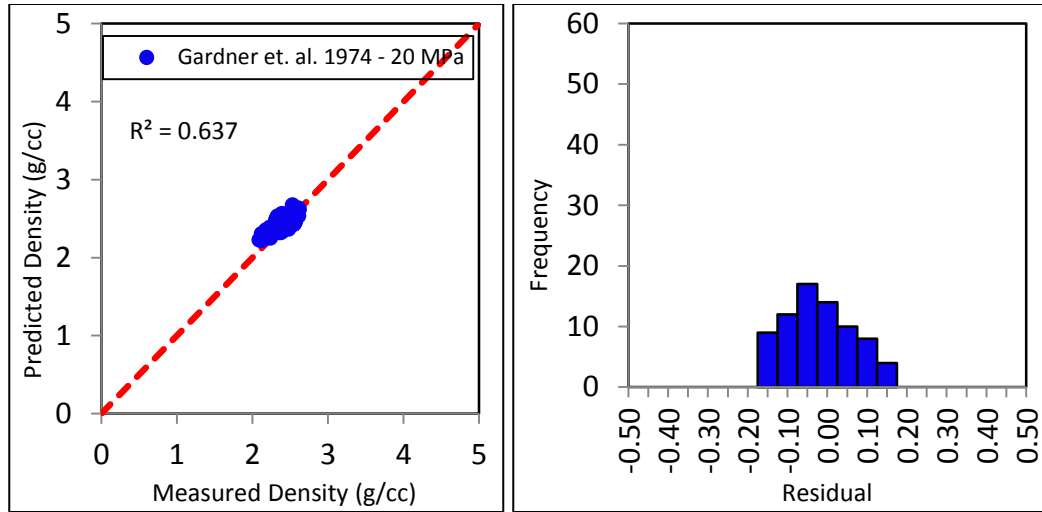


Figure 28: Gardner et al. Model for density prediction using Hans et al. Laboratory data at 20 MPa

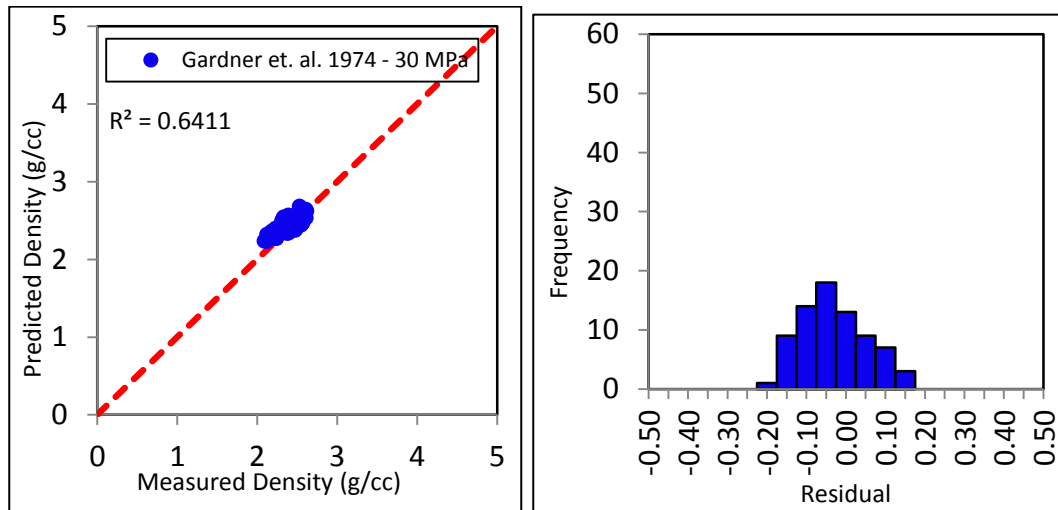


Figure 29: Gardner et al. Model for density prediction using Hans et al. Laboratory data at 30 MPa

When compared to outputs from the new density prediction model, it can be observed that the Gardner model produces a less accurate prediction of the formation bulk density with lower R-square values and highly dispersed residual errors in the four studied scenarios. Table 3 below gives a breakdown of the comparison of the R-square values of the new density prediction model and predictions from Gardner et al model.

Table 3: Model Validation's R-Square Values Comparison

	New Density Model	Gardner et. al. Model (1974)
5 Mpa	0.8918	0.6581
10 Mpa	0.9037	0.6495
20 Mpa	0.8911	0.637
30 Mpa	0.8872	0.6411

The new density prediction model is further validated using field well examples from the Grand Banks as well as the Niger Delta's tertiary deltaic basin in order to prove that this new model can be applied to other basins.

4.2.3 Grand Banks Basin Example for Model Method 1

The model was applied using the same well example in section 3.2 (GB1) while calibrating the Gardner equation. Figure 31 shows the sand and shale intervals from the gamma ray and resistivity logs as well as the caliper logs signifying no recorded hole problems. Figure 32 shows graphically how very well the new model is able to predict the formation bulk density for the entire span of which there is acquired density data. Using this in combination with the gamma ray log and resistivity logs which help indicate the sand and shale intervals, it can be found that the new model is able to predict the density well in both sand and shale intervals as well as those intervals that could be classified as shaly-sands (mixed lithology) intervals.

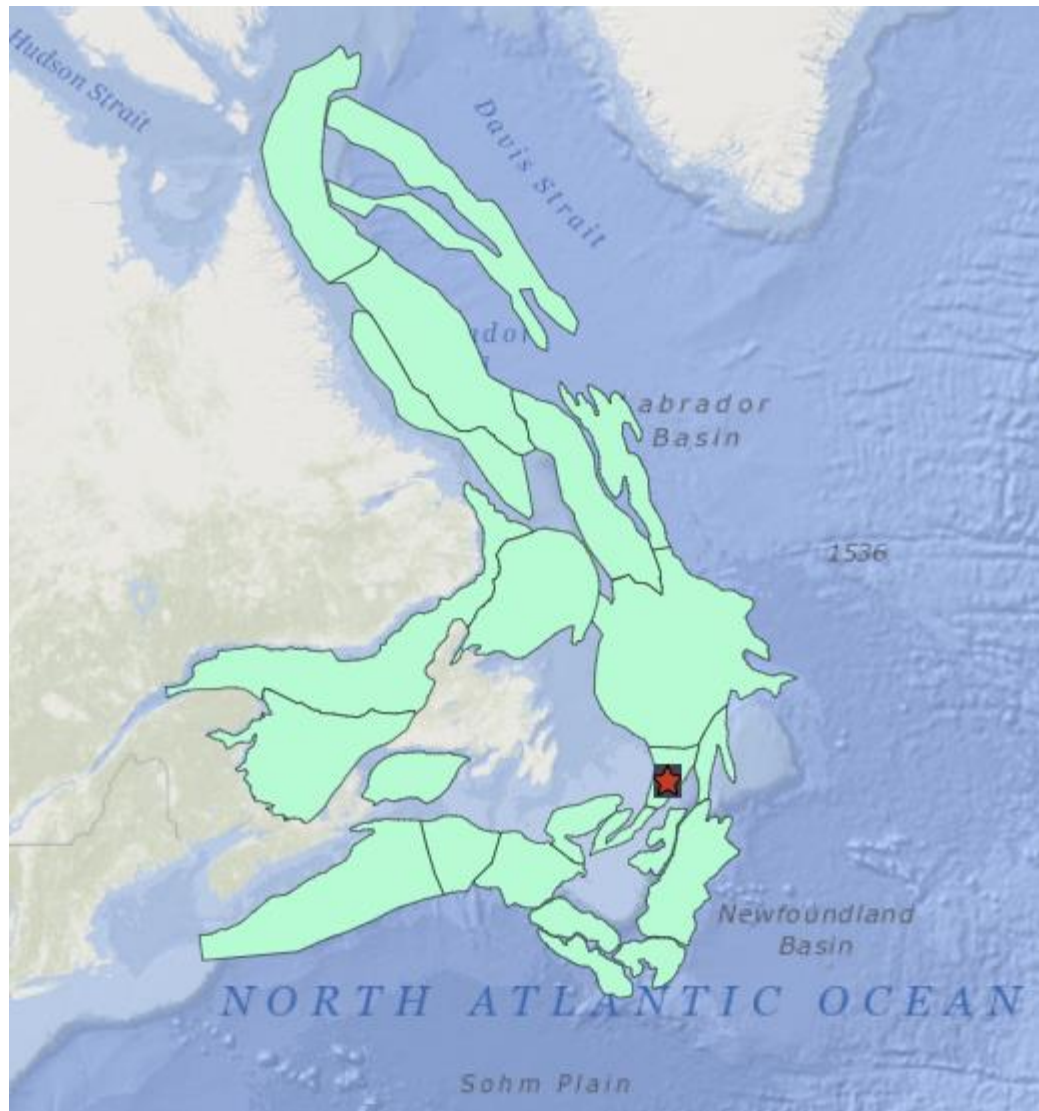


Figure 30: Approximate GB1 Well Location (NESS, 2019)

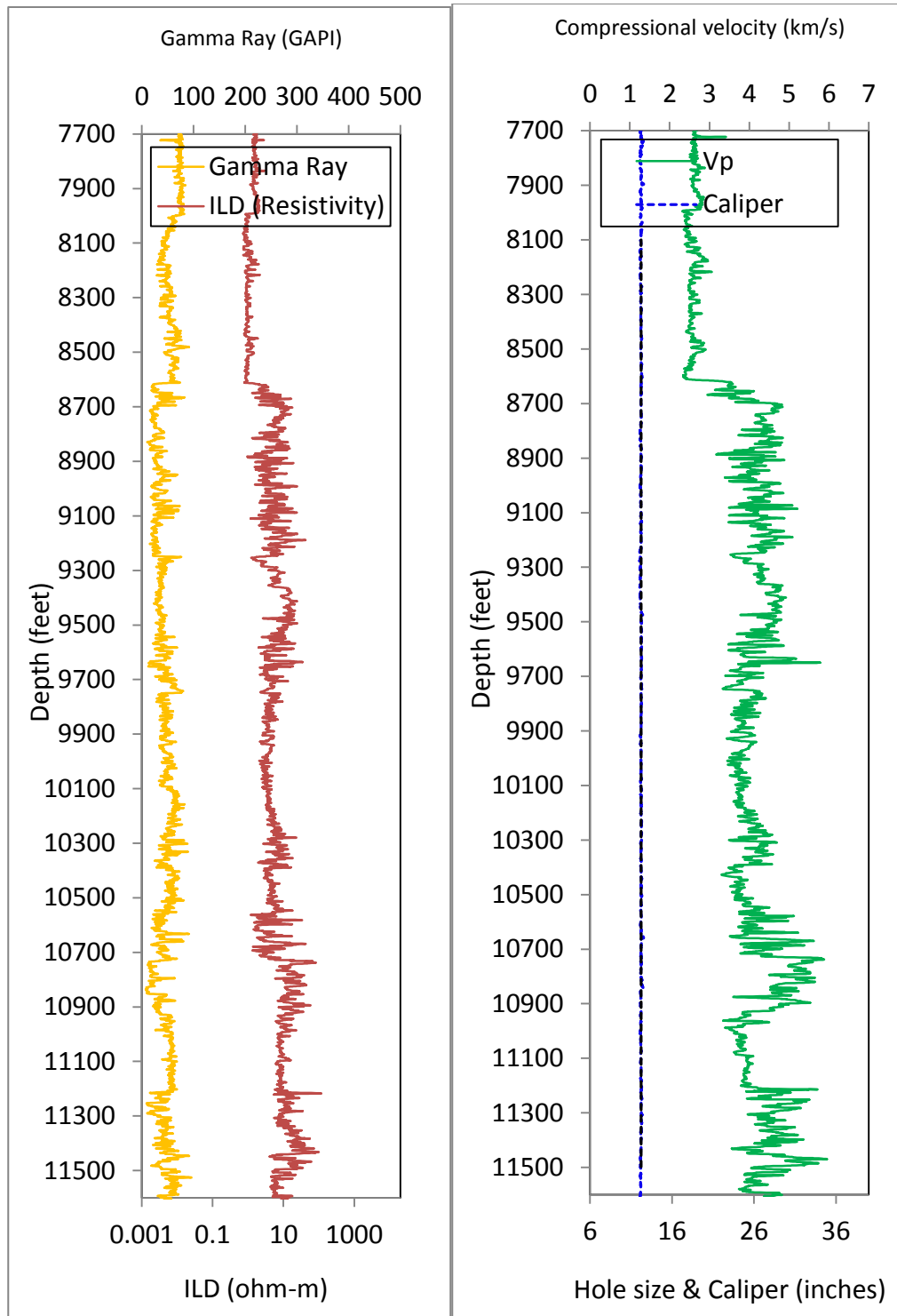


Figure 31: (a) Gamma Ray and Resistivity Logs (b) Compressional velocity and Caliper log readings for GB1 well.

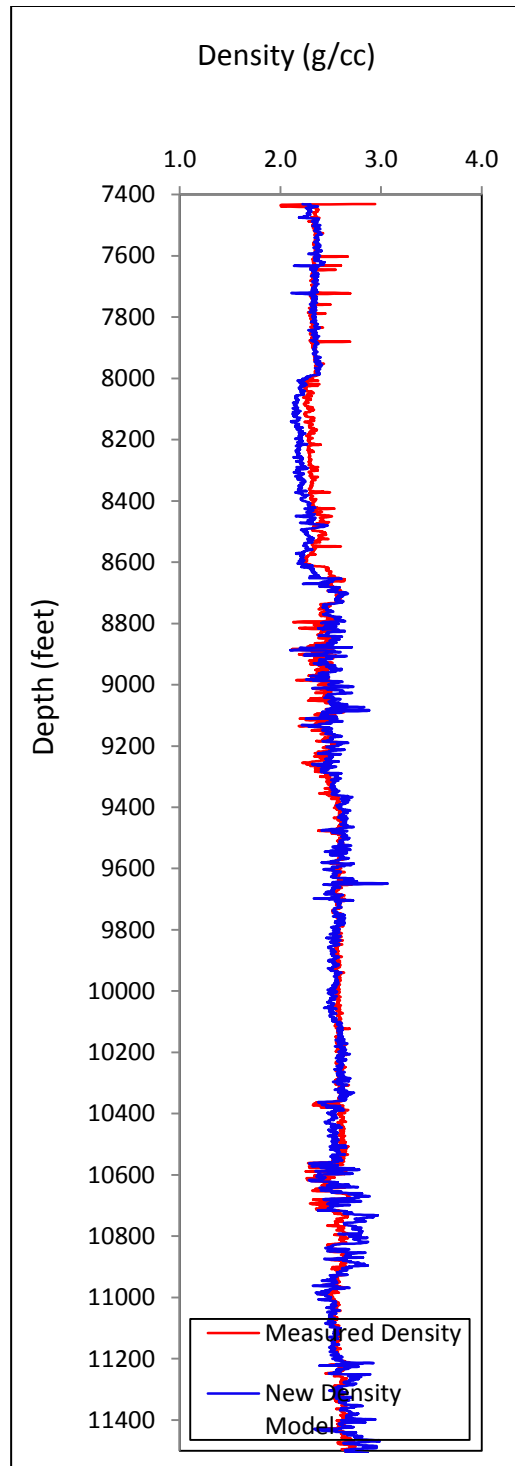


Figure 32: Measured versus predicted formation bulk density using the model method 1 for GB1 well.

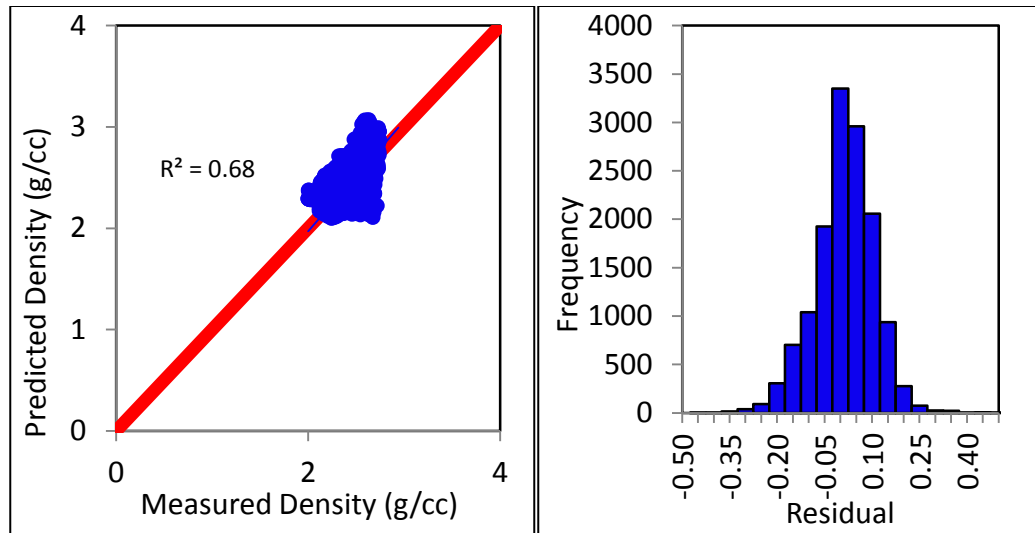


Figure 33: Model Method 1 Density Prediction validation for GB1 well

4.2.4 Niger Delta Basin Example for Model Method 1

The model was thereafter applied to a Niger Delta well (ND1) in the same manner as carried out for the Grand Banks well. Figures 35 to 37 displays readings from the gamma ray logs to indicate and be able to separate sand and shale intervals, caliper logs for drilled hole issues identification, the prediction obtained using the new model as well as the plot of measured versus estimated formation bulk density readings.

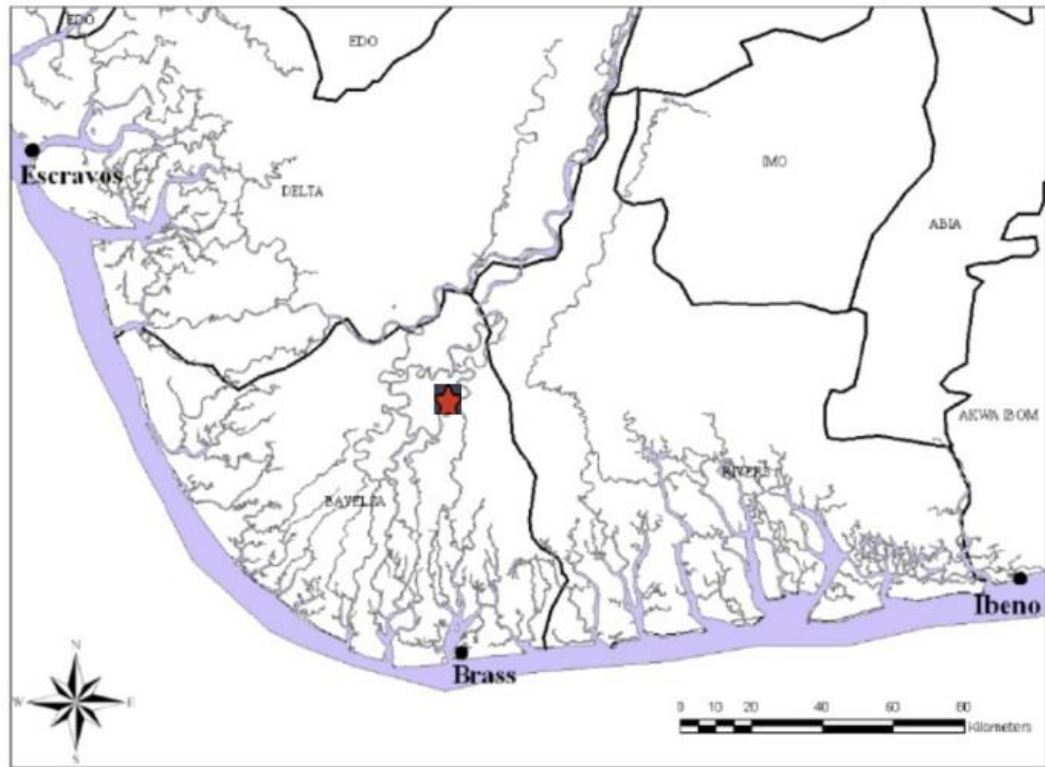


Figure 34: Approximate ND1 Well Location (Adegoke et al., 2010)

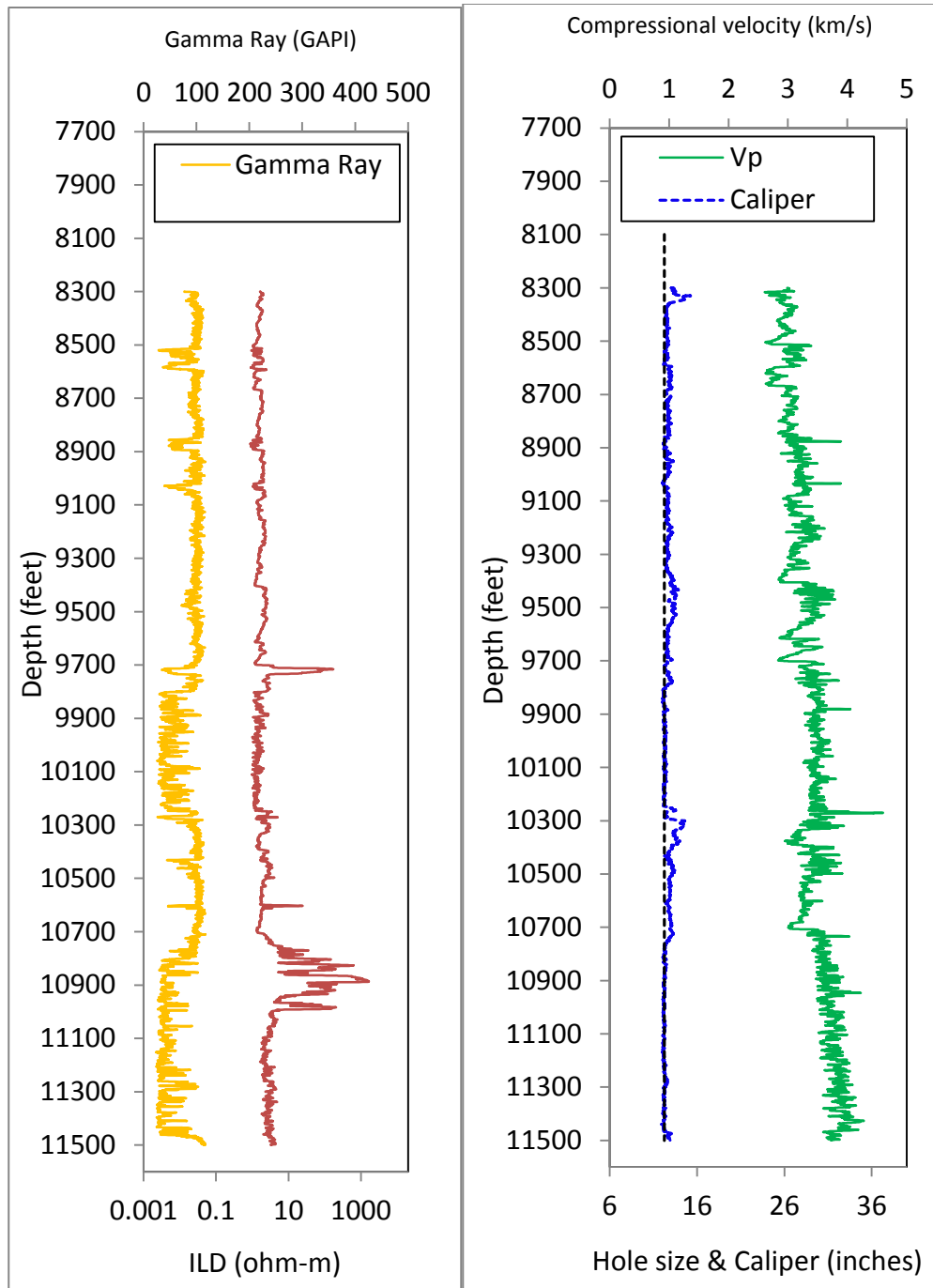


Figure 35: (a) Gamma Ray-Resistivity (b) compressional velocity and caliper log plots for ND1 well

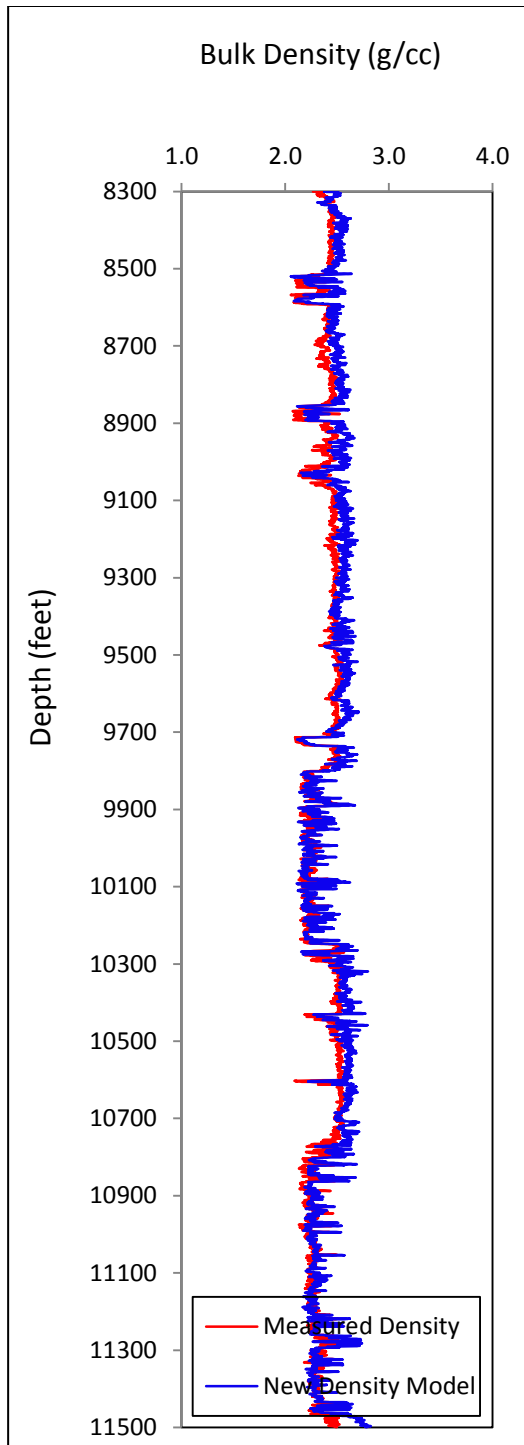


Figure 36: (a) Vp - Caliper plots (b) New density model match with measured density for ND1 well

As can be seen from figure 37, the prediction from model method 1 for the Niger Delta well is found to give a very good prediction of formation bulk density. The R-square value is high with acceptable residual error values.

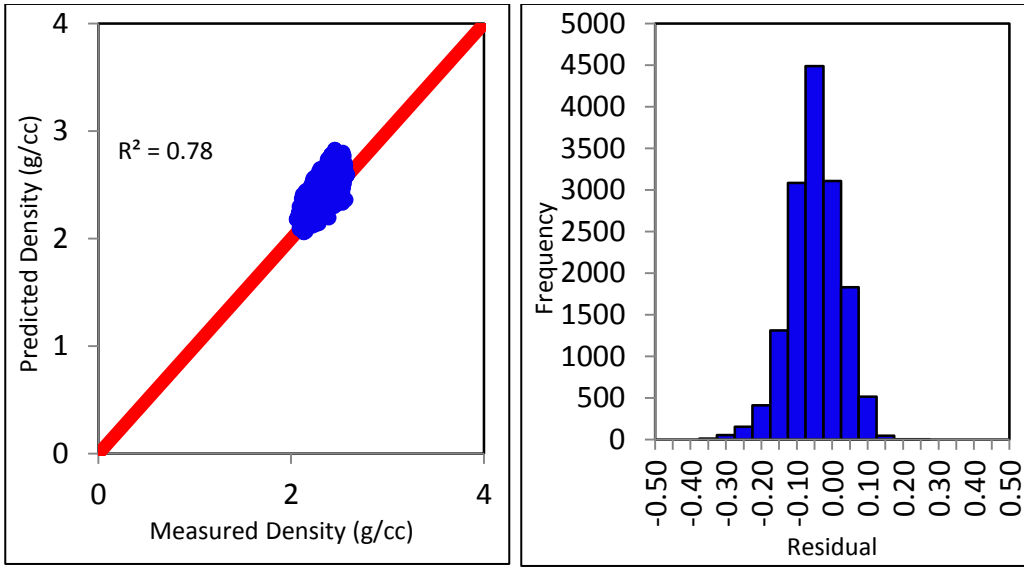


Figure 37: Model Method 1 Density Prediction validation for ND1 well

4.3 Model Method 2 Development

4.3.1 Model Method 2 Methodology

As briefly described initially, in seismic prospecting, Gardner's model is arguably the most widely used empirical relationship (Castagna and Backus 1993). Therefore, the starting point for the model method 2 development, which incorporates the concept of micro-cracks and mixed lithology is the generalized form of the Gardner's model given below.

$$\rho_b = A V_p^B \quad (4.8)$$

where A and B are regression coefficients. To be applicable to any type of formations in siliciclastic environments, a shale volume factor (V_{sh}) is required to normalize the Gardner's model for lithology effects as given by equation 4.9 below.

$$\rho_b = A[V_p + CV_{sh}]^B \quad (4.9)$$

where A, B and C are constant parameters. In consolidated rocks that contain micro-cracks, changes in effective stress will cause significant changes in compressional and shear wave velocities with little or no changes in formation porosity/bulk density until all the micro-cracks are closed. Therefore, equation

4.9 is considered inadequate to describe rocks that contain micro-cracks. Since compressional and shear wave velocities are affected by micro-cracks/fractures in similar manner and magnitude (Han et al. 1986; Eberhart-Phillips et al. 1989; Pan et al. 2017), incorporating shear wave velocity into the equation 4.9 will negate the effect of micro-cracks on compressional wave velocity. This results in equation 4.10 shown below.

$$\rho_b = A[V_p - V_s + CV_{sh}]^B \quad (4.10)$$

where **A**, **B**, **C** and **D** are constant parameters.

Literally, equation 4.10 is consistent with laboratory and field observations. The difference between the compressional and shear wave velocities is a function of porosity/bulk density and shale volume (Castagna et al. 1985; Han et al. 1986).

Equation 4.10 is somewhat different from other formation bulk density prediction models in that it combines both compressional and shear wave velocities in empirical correlations 2.11 and 2.12. In these models (unlike the newly developed model), the effects of micro-cracks on compressional wave velocity are not negated by the shear wave velocity due to the way in which the compressional and shear wave velocities are combined. For instance, equations 2.11 and 2.12 wrongly imply that the presence of micro-cracks will significantly

reduce the formation bulk density because of the reduction in both the compressional and shear wave velocities.

4.3.2 Validation of Model Method 2

To be applicable to any types of lithology and rocks that contain micro-cracks/fractures in siliciclastic environments, the calibration data must contain a mixture of sands and shales in various proportions and rocks with micro-cracks. The laboratory data provided by Han et al. (1986) meet the above conditions. Han et al. (1986) conducted laboratory ultrasonic experiments on brine-saturated sandstone core samples obtained from quarries in the USA and Gulf of Mexico wells. The laboratory experiments were conducted on both clean and non-clean consolidated formations, representing a wide range of formations with the rock porosities varying from 3% to 30% and the volume of shale varying between 0% to 51%. The experimental studies were also conducted at various values of effective stresses corresponding to gradual closure of micro-cracks with relatively little or no changes in rock porosity/bulk density until the micro-cracks are closed. Table 4 and Figure 38 show the relationship between differential pressure/effective stress, compressional wave velocity, shear wave velocity, porosity and sonic velocity difference for samples #1 and #2 (Han et al.

1986). Readers are referred to Han's paper for more details on the experimental procedures.

Table 4: The laboratory data for samples #1 and #2 (Han et al. 1986).

Differential pressure (Mpa)	Sample #1				Sample #2			
	V_p (km/s)	V_s (km/s)	Porosity (fraction)	$V_p - V_s$ (km/s)	V_p (km/s)	V_s (km/s)	Porosity (fraction)	$V_p - V_s$ (km/s)
5	4.26	2.53	0.1846	1.73	4.08	2.39	0.2006	1.69
10	4.44	2.69	0.1838	1.75	4.27	2.54	0.2001	1.73
20	4.58	2.84	0.1831	1.74	4.34	2.66	0.1996	1.68
30	4.64	2.89	0.1825	1.75	4.40	2.70	0.1992	1.70
40	4.66	2.91	0.1821	1.75	4.42	2.72	0.1989	1.70

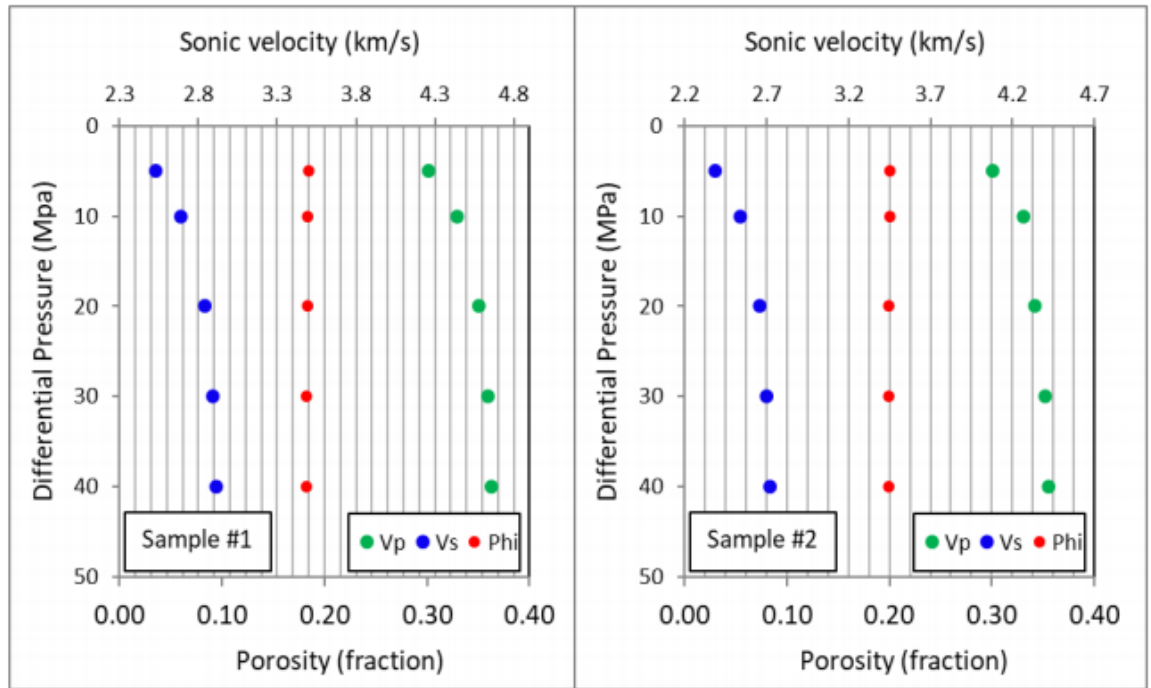


Figure 38: The differential Pressures, Sonic Velocities and Porosities for samples #1 and #2

In sample #1, while the compressional wave velocity increases from 4.26 km/s at 5 MPa differential pressure to 4.66 km/s at 40 MPa, the differential pressure and the shear wave velocity increases from 2.53 km/s to 2.91 km/s over the same differential pressure range, the rock porosities (formation bulk densities) are relatively constant. The same trend is also observed in sample #2. For the samples #1 and #2, the micro-cracks appear to be closing between 30 - 40 MPa differential pressures because there is no appreciable increase in compressional and shear wave velocities with increase in differential pressure/effective stress.

By calibrating equation 4.10 to the compressional wave velocity, formation bulk density, shear wave velocity and shale volume data provided by Han et al. (1986) at 5, 10, 20, 30 and 40 MPa differential pressures for shaly sandstone core samples, the values of the constant parameters A, B and C are determined to be 1.859, 0.205 and 0.503 respectively. Hence, the new formation bulk density prediction model based on equation 4.10 is given by equation 4.11 below.

$$\rho_b = 1.859[V_p - V_s + 0.205V_{sh}]^{0.503} \quad (4.11)$$

The above model is designed to work for multiple lithology in siliciclastic environments for intact rocks and formations that contain micro-cracks. In fact, using the quartz matrix properties with zero porosity (compressional wave velocity = 6.05 km/s; shear wave velocity = 4.09 km/s; grain density = 2.649 g/cm³; shale volume is equal to zero) and illite (shale) matrix properties with zero porosity (compressional wave velocity = 4.32 km/s; shear wave velocity = 2.54 km/s; grain density = 2.66 g/cm³; shale volume = 1.00) (Greenberg and Castagna, 1992), the new formation bulk density prediction model (equation 4.11) is able to excellently and remarkably predict the matrix densities of quartz and illite within an accuracy of less than 1.6% (<±0.042 g/cc). This

demonstrates the applicability of the new model in intact rocks with no pore spaces. When applying Gardner and Brocher models over the same data set, the two models grossly underestimate in illite and over-estimate in quart. The reason could be due to the fact that V_p decreases in the presence of shale which may not necessarily reduce the density.

The new density prediction model is further validated using field well examples from the Grand Banks (well GB1). In order to prove that this new model can be applied to other basins, the model was also tried for a well from the Tertiary Deltaic Basin of the Niger Delta Basin (well ND1).

4.3.3 Grand Banks Basin Example for Model Method 2

The model was applied using the same GB1 well section. The following two figures displays how well the predicted bulk density model matches measured bulk density from the field as well as the R-square value and the residual errors distribution.

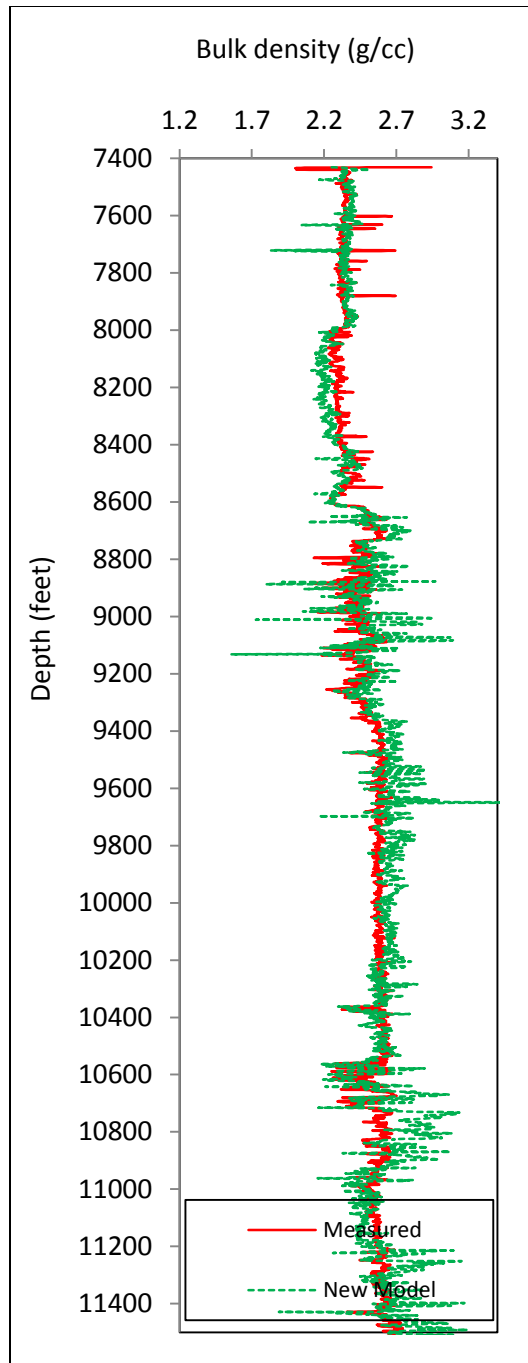


Figure 39: Measured versus predicted formation bulk density using the model method 2 for GB1 well.

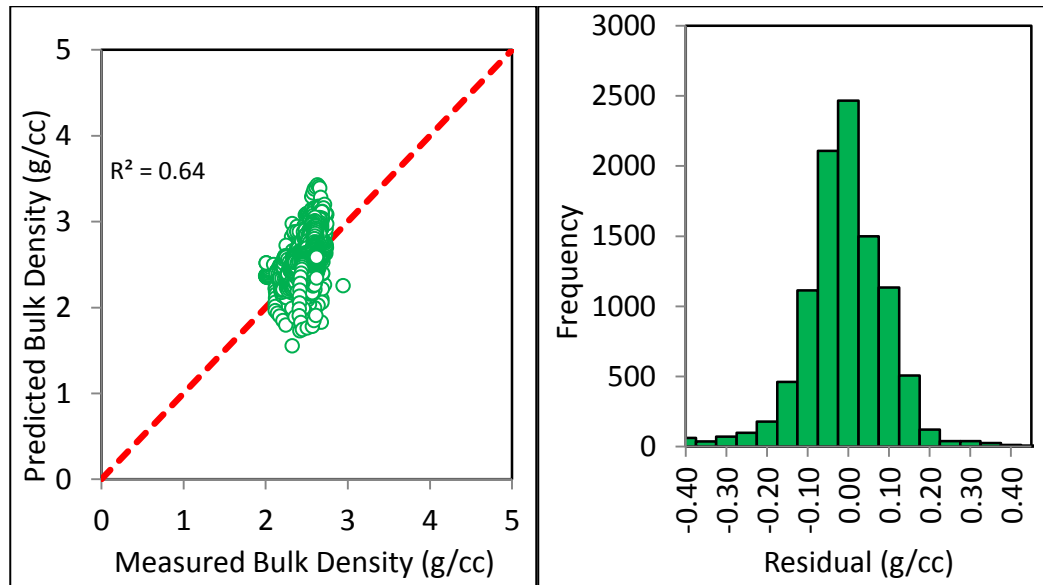


Figure 40: Model Method 2 Density Prediction validation for GB1 well

4.3.4 Niger Delta Basin Example for Model Method 2

The model method 2 was applied to the same ND1 well used for Model method 1. Figures 41 shows the measured bulk density prediction plotted with the predicted bulk density. Figure 42 shows the spread of the residual error as well as the R-square value.

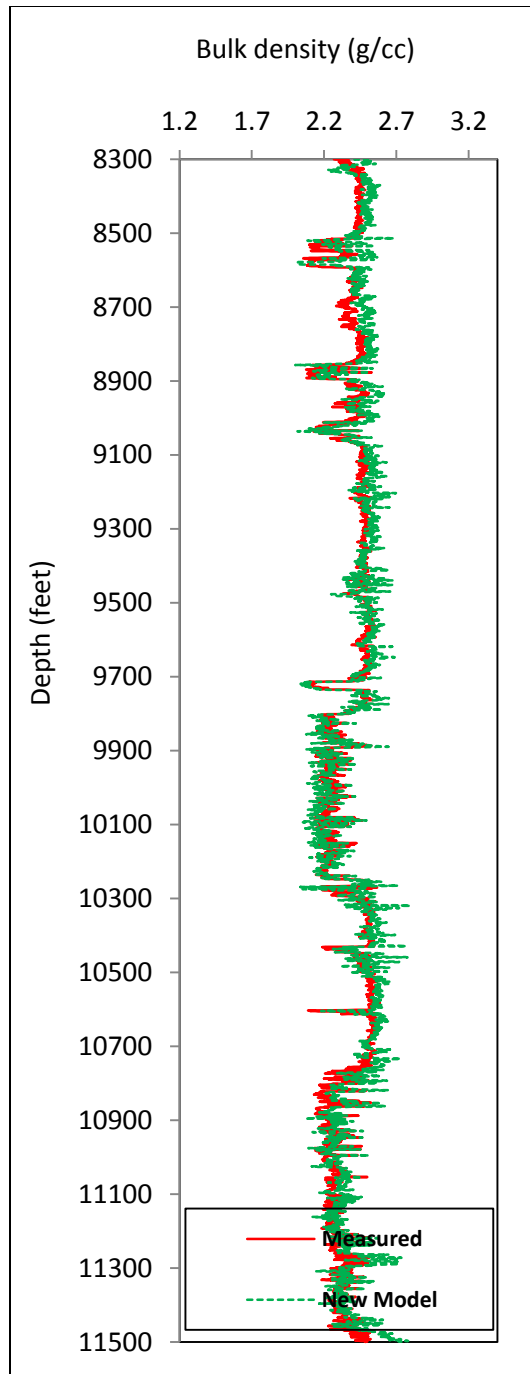


Figure 41: Measured versus predicted formation bulk density using the model method 2 for ND1 well.

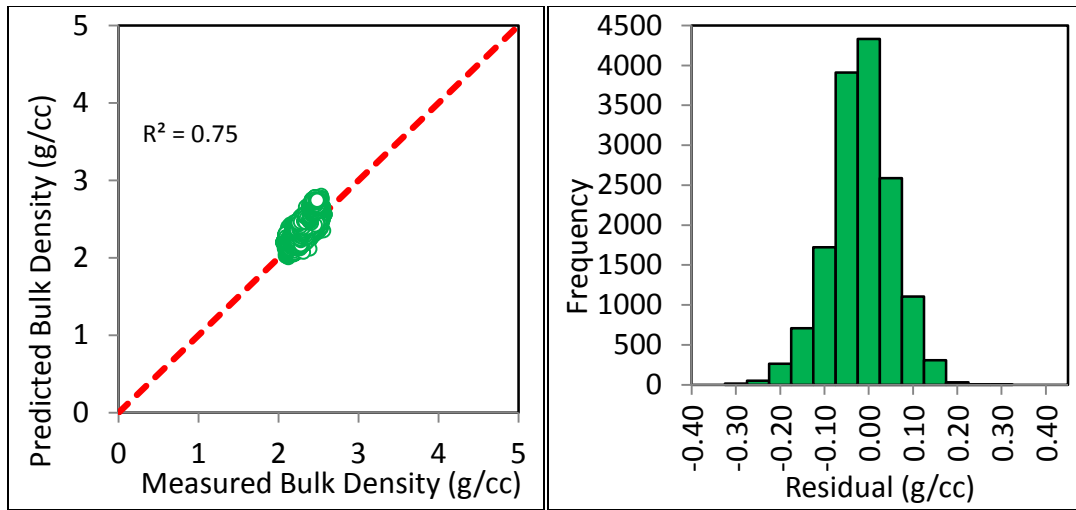


Figure 42: Model Method 2 Density Prediction validation for ND1 well

4.4 Discussion of Model Methods 1 and 2 Results

Two model development approaches have been introduced. The two approaches which are data driven are expected to work very well in predicting formation bulk density for formations with micro-cracks and have proven to be robust ways of prediction using well examples from two different geological settings. Using the R-square values as a comparison metrics, model method 1 produces a value of 0.68 for GB1 and 0.78 for ND1 while model method 2 gave a value of 0.64 for GB1 and 0.75 for ND1. These values are acceptable within the limit of offshore environments. While model method 1 was generally developed, model method 2 was derived with siliciclastic geologic settings in

mind. In order to further verify the robustness of model method 2 in purely siliciclastic environments, an additional well example with a siliciclastic geologic formation characteristics was selected for analysis. A similar analytical approach was undertaken from which results of the model method 2 prediction was compared to those of prior models for formation bulk density prediction.

4.5 Model Method 2 for Siliciclastic Formations

To further validate the applicability of the new formation bulk density prediction model method 2 (equation 4.11), an onshore exploratory well located about 70 km northwest of Port Harcourt in the Niger Delta basin was considered as the case study well. Figure 43 displays the wireline logs acquired in the 8 ½” hole section of the well which was drilled with water-based mud. The well logs consist of shear wave velocity, compressional wave velocity, neutron, gamma ray, bulk density, caliper, micro resistivity, medium resistivity and deep resistivity. As part of conducting quality checks, the well log data have been corrected for all the necessary environmental effects such as mud cake thickness, actual hole size, tool stand-off, mud type, mud weight, temperature and pressure. The caliper log readings indicates that the downhole conditions

under which the logging operations were conducted has no excessive washouts which signifies a good hole condition.

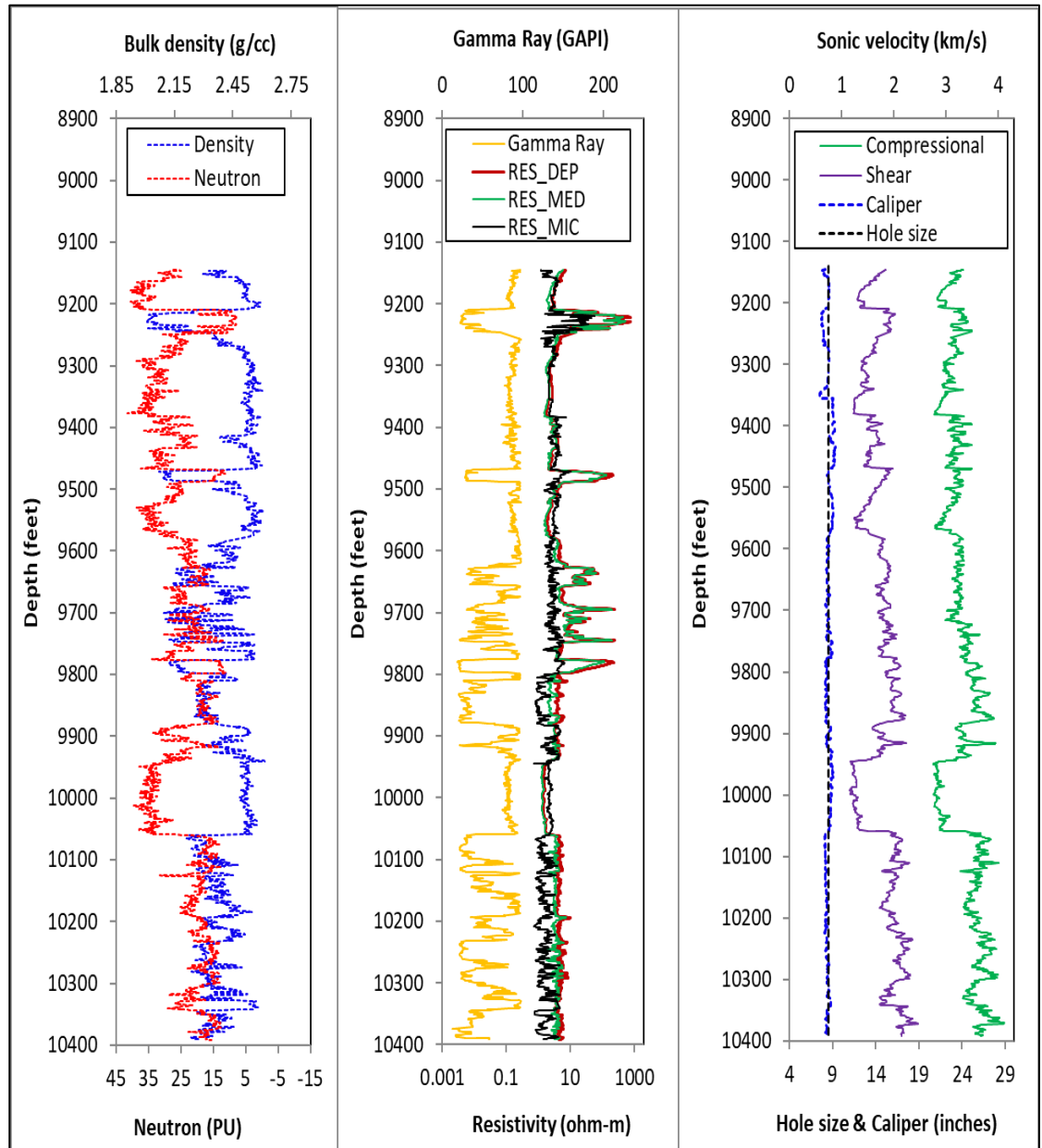


Figure 43: The well logs for well ND2 showing the petrophysical properties of the penetrated rocks.

Figure 44 displays the density-depth plots showing the comparison of the predicted and measured formation bulk densities for the well under consideration. The formation bulk densities are computed using equation 4.11 (model method 2), Gardner's equation and Brocher's equation. For comparison purposes, the formation bulk densities are computed using Gardner's and Brocher's models because they are the most widely used empirical relationships developed to date to work for a wide range of lithology. For the Niger Delta sediments, field observations by the author have shown that the shale volume is linearly correlated to gamma ray index. Hence, the shale volume factor (in fraction) is computed using equation 4.12.

$$V_{sh} = I_{GR} = \frac{GR_{log} - GR_{min}}{GR_{max} - GR_{min}} \quad (4.12)$$

where GR_{log} is the gamma ray reading at any given depth; GR_{min} is the sand line gamma ray reading. Depending on the geographic area or rock age, there are other non-linear empirical relationships between volume of shale and gamma ray index (Larionov 1969; Stieber 1970; Clavier et al. 1971; Assaad, 2008).

Figure 44 clearly shows the advantage of including the shale volume factor into the formation bulk density prediction models. A good agreement exists between the predicted and measured formation bulk densities using the model method 2. The new model works well for various formations in siliciclastic environments (clean sands, clean shales and formations that contain a mixture of sands and shales in any proportion) because the shale volume term normalizes the sonic velocities for lithology effects. The Gardner's and Brocher's models fail to produce reasonable estimates of formation bulk densities across some intervals. They grossly underestimate formation bulk densities in clean shale intervals. This clearly demonstrates that any empirical correlation that relates the formation bulk density to only compressional wave velocity will likely produce erroneous results in some intervals when applied over a lithological column that consist several stratigraphic units in siliciclastic environments. Since overburden pressure is estimated from surface to the depth of interest along the well path, care should be taken in using any formation bulk density prediction model that is based on only the compressional wave velocity to estimate pre-drill formation bulk density for overburden pressure determination. This can lead to inaccurate pore and fracture pressure predictions which can lead to well control and loss circulation incidents during drilling.

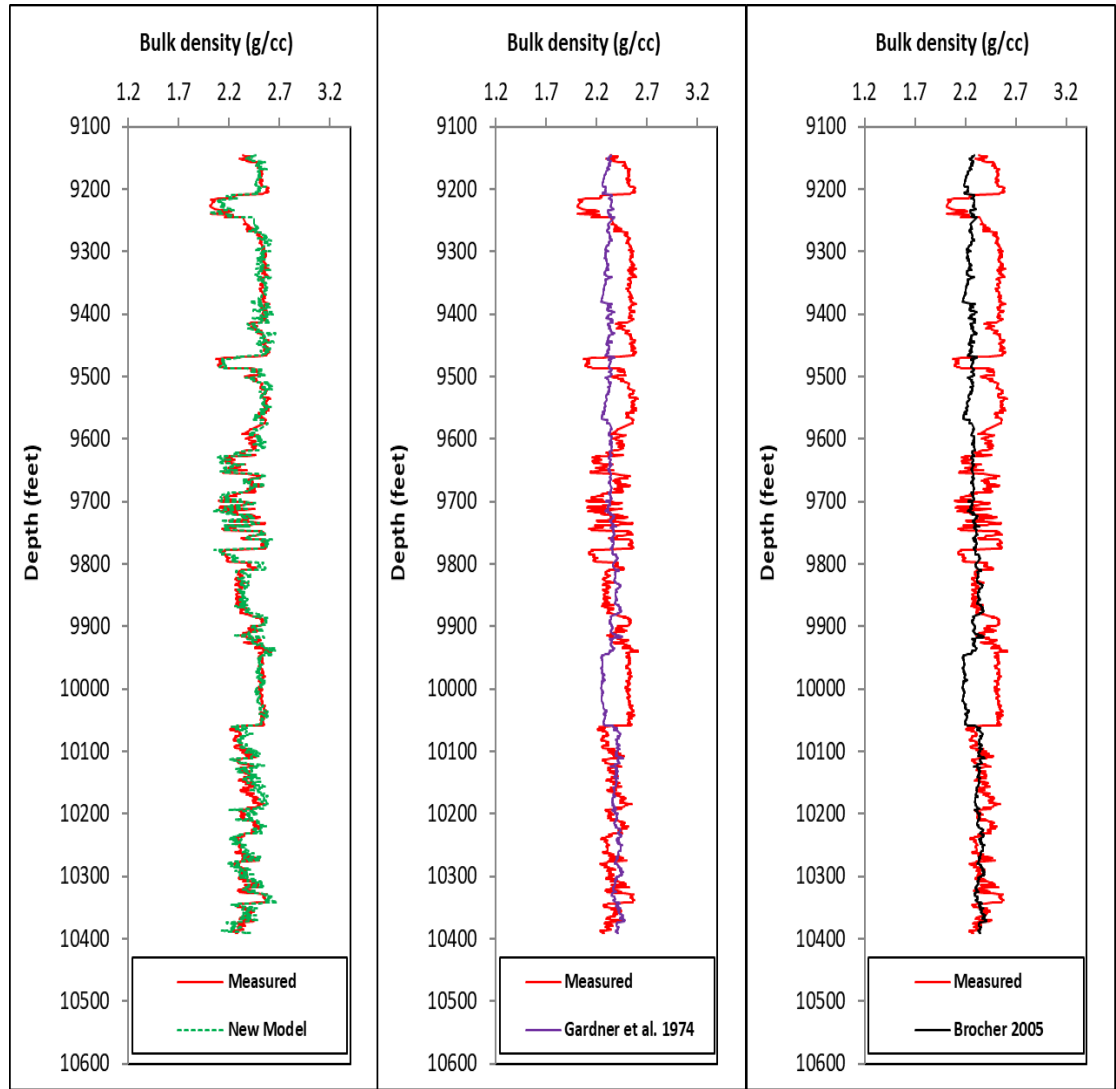


Figure 44: The comparison of predicted and measured formation bulk density for various models under consideration for well ND2.

Figure 45 displays the cross-plots of predicted and measured bulk density along with the histograms of the residuals associated with various estimation methods.

The residual error value is computed from the difference between the measured and predicted formation bulk densities. The model method 2 outperforms the most widely used empirical relationships. While the new model shows the normal error distribution curve, the Gardner's and Brocher's models show great bias toward under-prediction. More than 97% of the data points fall between the residual values of -0.1g/cc and $+0.1\text{g/cc}$ using the model method 2. However, less than 40% of the data points fall between the residual values of -0.1g/cc and $+0.1\text{g/cc}$ using Gardner's and Brocher's models. The model method 2 produces the lowest root mean square error (RMSE) and least maximum deviations when compared to the most widely used empirical relationships. The RMSEs for model method 2, Gardner's model and Brocher's model are 6%, 18% and 21% respectively. The coefficient of determination (R^2) values for the new model, Gardner's model and Brocher's model are 0.81, 0.27 and 0.27 respectively.

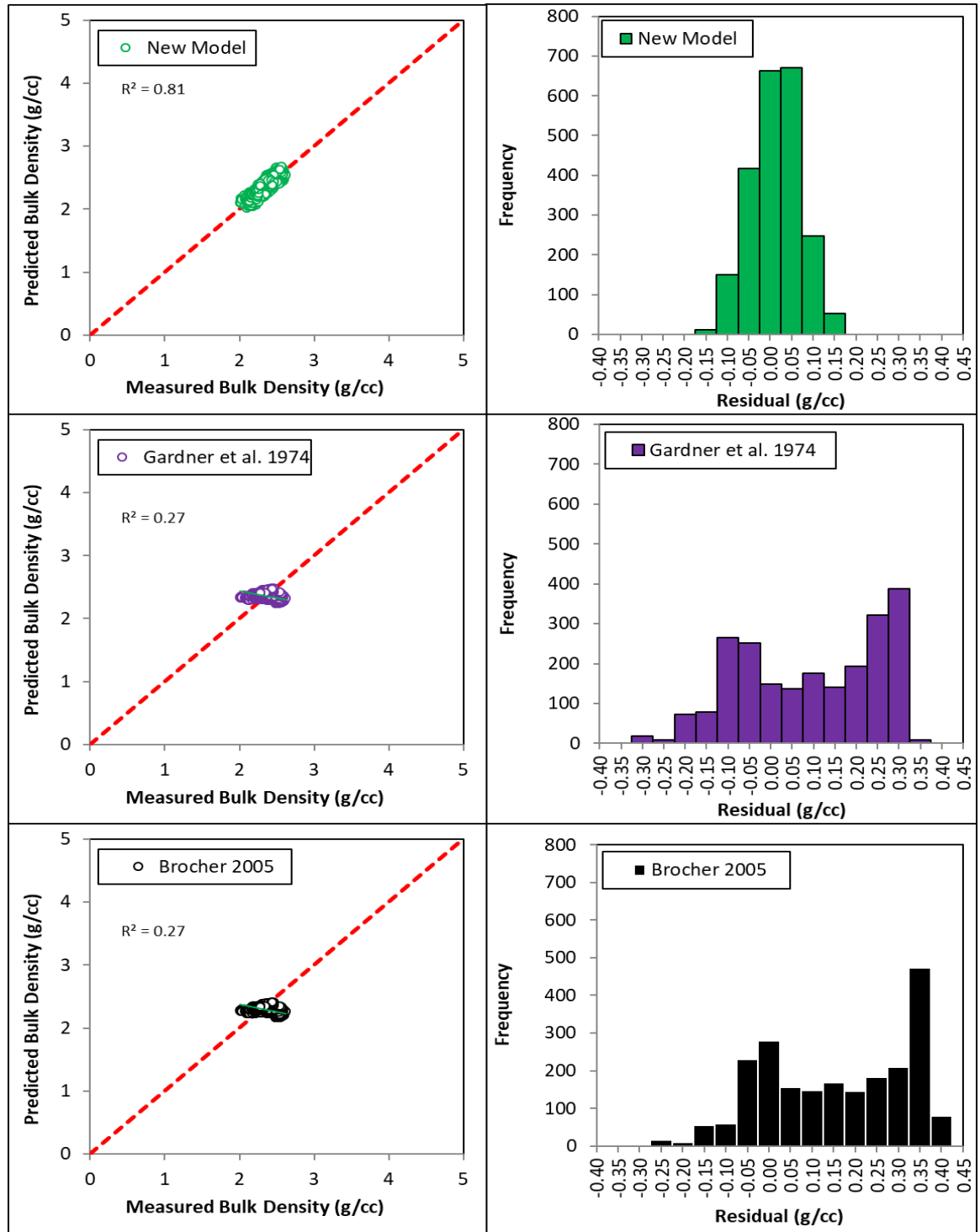


Figure 45: The cross-plots of predicted and measured bulk density with histograms for Well ND2.

Laboratory and field data from different sedimentary basins have been used to develop and validate the new density log prediction technique for siliciclastic rocks. In the new model method 2, formation bulk density is expressed as a function of sonic velocity difference and shale volume. The new model is applicable to clean sands, clean shales, a mixture of sands and shales in any proportion, intact rocks and formations that contain microcracks/fractures. The statistical analysis shows that the accuracy of the new formation bulk density prediction model is higher than the most widely used relations (lower RMSEs, lower residuals and better error distributions). However, just like any of the existing empirical relationships, the new model may not be suitable for gas filled rocks. While the new model is expected to work well in any siliciclastic settings, it does not cover carbonate and evaporite environments. The generalized form of the new model method 2 can be calibrated to regional carbonate and evaporite rocks to obtain the new set of models for these environments. Predictability of model method 1 and 2 will be similar for general wells consisting of various lithology. However, for wells with micro-fractures in a siliciclastic environment, model method 2 will give a better prediction of formation bulk density.

4.6 Chapter Summary

The chapter introduces a new formation bulk density prediction models (model method 1 and model method 2) which are found to be applicable to formations with mixed lithology and micro-cracks. The two models were validated with field examples using wells from the Grand Banks and the Niger Delta. Formation bulk density prediction from the two model methods were found to be very acceptable within the operating limit of an offshore/onshore environment for formation bulk density prediction. Model method 2 was further tested with a field well example exhibiting siliciclastic formation characteristics and was found to out-perform the two most widely used models in the oil and gas industry (Gardner and Brocher models) for formation bulk density prediction. The newly derived formation bulk density models are robust and recommended for use in varied geologic basins since they incorporate the concept of mixed lithology and micro-cracks. The generalized forms of these models could be adapted and calibrated to work for other regions.

Chapter 5

A Shear-Wave Velocity Model

5.1 Shear Velocity from Compressional Velocity

For some of the wells drilled to date offshore Grand Banks as an example, there is no shear wave velocity (V_s) data acquired. In these instances, shear wave velocity will have to be derived from compressional wave velocity (V_p) data. V_p - V_s regression will usually require data to be taken from a combination of consolidated and unconsolidated formation. Low velocity rocks in shaly formation (slow formation) are not necessarily accompanied by low density which makes V_s to be underestimated. Therefore, there is a need to develop an all-inclusive shear velocity model.

5.2 Previous V_s Models Preview

One of the most commonly used models for predicting shear wave velocity from compressional wave velocity is a linear model proposed by Castagna et al. (1985).

$$V_s = AV_p - B \quad (5.1)$$

Where $A = 0.862$ and $B = 1.172$.

Han et al. (1986) proposed a model similar to that of Castagna's by using cores to perform several laboratory ultrasonic experiments on brine saturated and shaly sandstone samples. In Han's model, $A = 0.79$ and $B = 0.85$

Brocher (2005) gathered data for a wide variety of common lithology including well logs, laboratory, vertical seismic profiling (VSP) as well as field tomography to come up with a nonlinear polynomial equation. This equation mainly requires values of compressional velocity to estimate shear wave velocity.

$$V_s = 0.7858 - 1.2344V_p + 0.7949V_p^2 - 0.1238V_p^3 + 0.0064V_p^4 \quad (5.2)$$

5.3 The Proposed Vs Model Development

The new developed model which incorporates a density term into the equations is proposed. Laboratory investigations on brine saturated porous rocks have shown that V_s is directly related to V_p . From elastic theory, V_s is inversely proportional to $\sqrt{\rho}$ (Hamada, 2004).

Combining the above two conditions, shear wave velocity is expressed as a function of $V_p/\sqrt{\rho}$. In general, shear wave velocity increases with $V_p/\sqrt{\rho}$.

To be applicable to any type of formation strengths, a power law relationship is proposed between the shear wave velocity and $V_p/\sqrt{\rho}$ since majority of empirical relations between rock strength and rock petrophysical properties follow either a power law or exponential relationship (Chang et. al. 2006).

$$V_s = A \left[\frac{V_p}{\sqrt{\rho}} \right]^m \quad (5.3)$$

Generally, when $V_p=0$, $\rho=0$. When $V_s=0$ (fluids), V_p & ρ will have non-zero positive values. In order to account for the above two conditions, a modified power law relationship is proposed as below:

$$V_s = A \left[\frac{V_p}{\sqrt{\rho}} \right]^m - B \quad (5.4)$$

The new developed model which incorporates a density term into the equations is shown above. This model is usable in predicting shear wave velocity for wells at the Grand Banks and results compared to the previous models shows

remarkable improvement in shear wave velocity prediction. The validity of the equation diminishes as bulk density approaches zero.

5.4 The Proposed V_s Model Calibration

The new equation is calibrated to experimental data by Han et al. (1986) at 5 and 30 Mpa differential pressure and Hossain et al (2012) at 3 and 7 Mpa confining pressure. This allows the proposed model to cover a wide range of effective stresses usually found in shallower and deeper depths of a sedimentary basin.

Using the Least Square Method, the values of **A**, **B** and **m** were found to be 2.41, 2.35 and 0.98 respectively and as such the final equation reduces to:

$$V_s = 2.41 \left[\frac{V_p}{\sqrt{\rho}} \right]^{0.98} - 2.35 \quad (5.5)$$

The newly derived shear wave velocity model is further tested and validated with three separate Grand Banks wells for which there are needed acquired data. This is further compared to the widely used prior models (Brocher, Castagna and Han et al. models) as described in the following sections.

5.5 Field Wells Validation

The following sections show the application of the developed shear wave velocity equation (equation 5.5) to three field wells (GB2, GB3 and GB4) located offshore Grand Banks.

5.5.1 Well GB2 Shear Wave Velocity Validation

The analysis below applied the developed model to wells offshore Grand banks and compared with Han et. al. model, Castagna model and Brocher model for shear wave velocity prediction. The GB2 well has shear wave velocity data acquired from about 3600 ft to approximately 5750 ft. Equation 5.5 was applied to predict the shear wave velocity which was then compared to the acquired measured velocity. Similarly, Brocher, Castagna and Han et al. models were also applied to predict the shear wave velocity for this well. Figures 46 to 50 shows the result of this exercise.

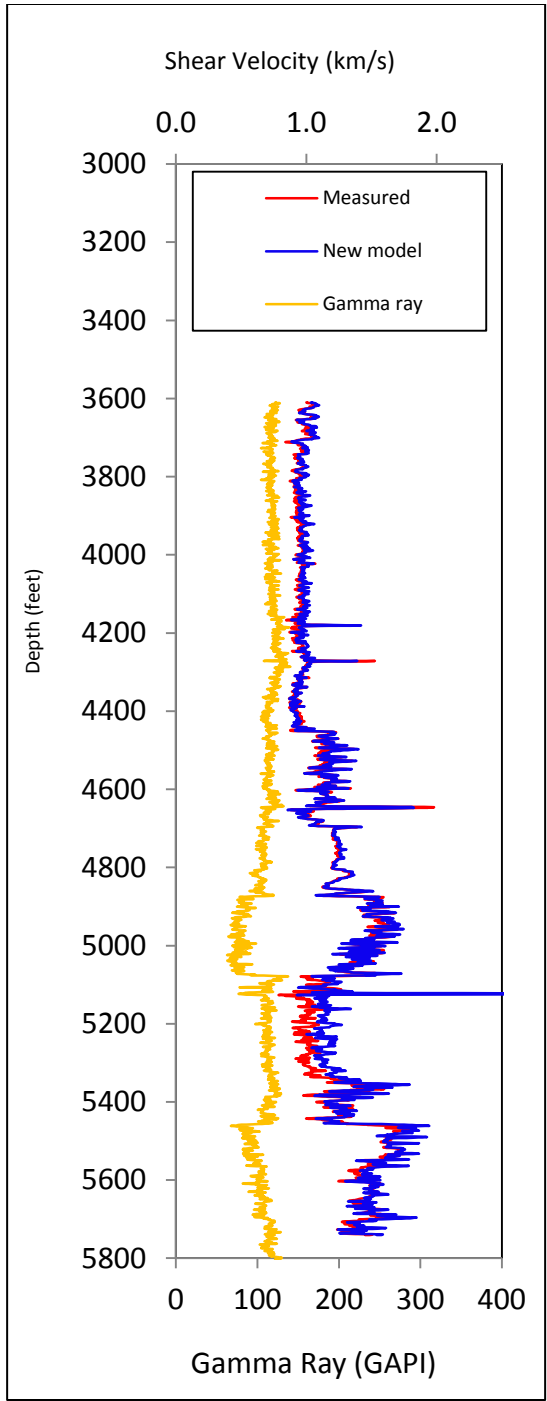


Figure 46: Well GB2 - Matching plots of new model with measured data with GR plot

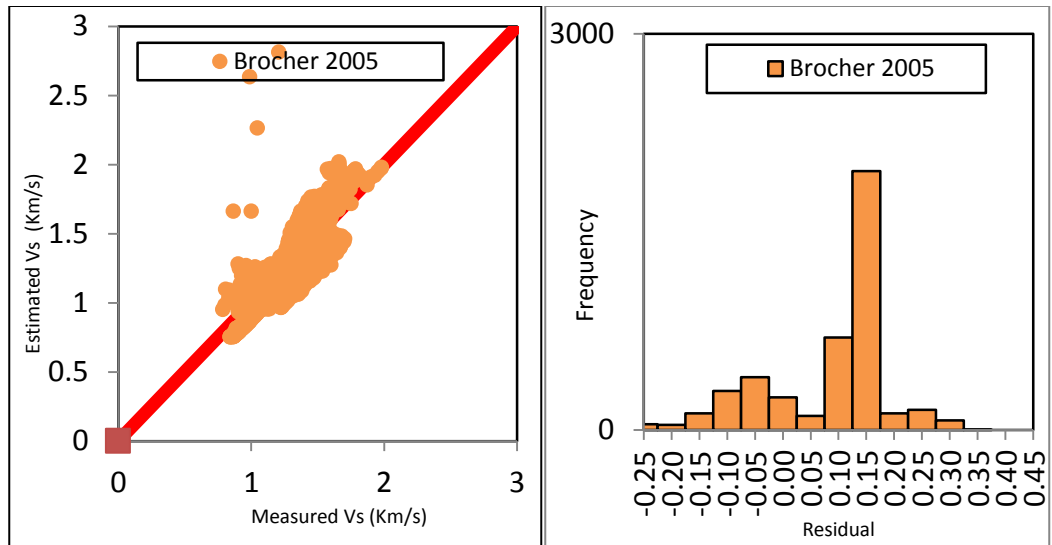


Figure 47: Well GB2 - Measured and Estimated Vs with Residual frequency for Brocher model

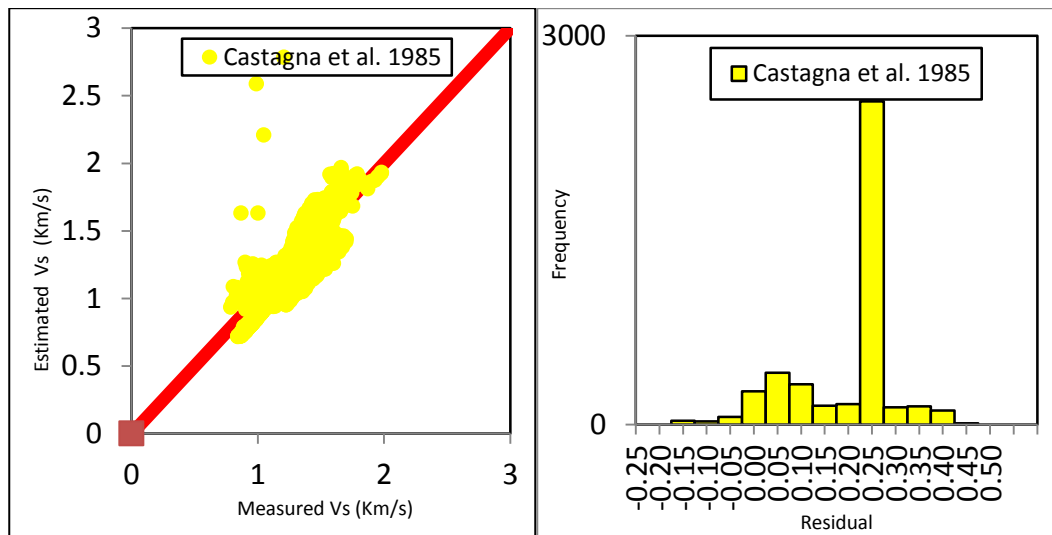


Figure 48: Well GB2 - Measured and Estimated Vs with Residual frequency for Castagna model

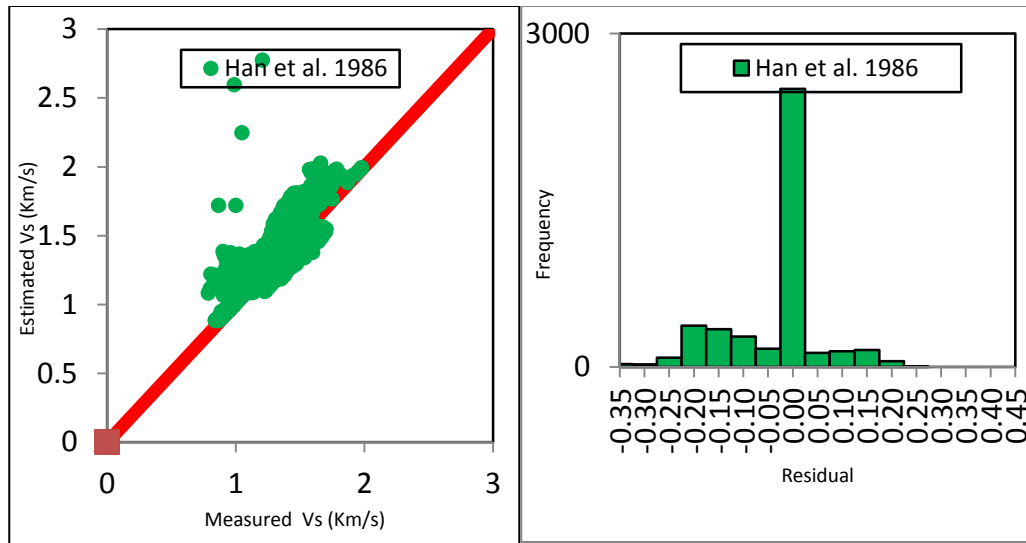


Figure 49: Well GB2 - Measured and Estimated Vs with Residual frequency for Han model

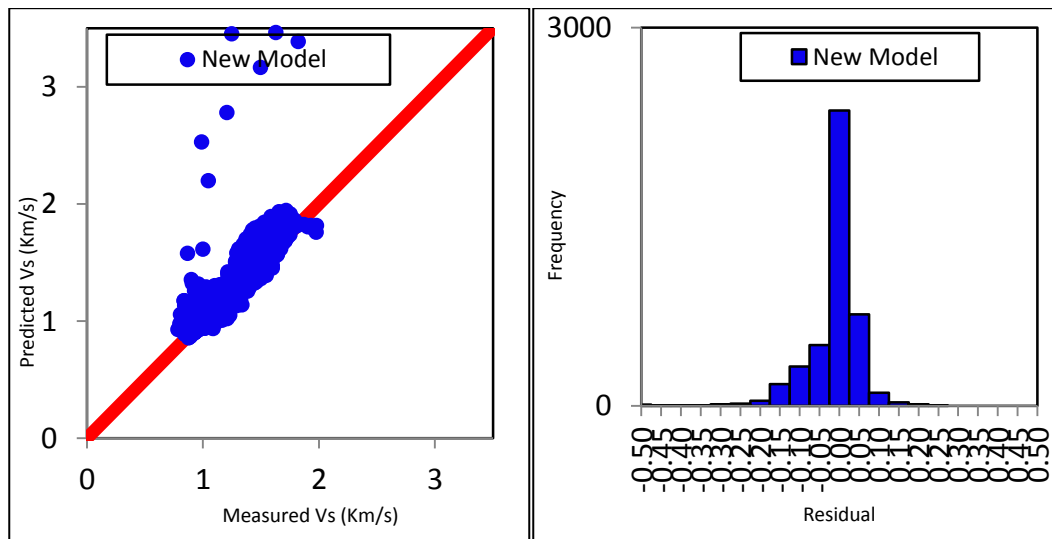


Figure 50: Well GB2 - Measured and Estimated Vs with Residual frequency for New model

Figure 32 shows a very good match of measured field Vs and that predicted by the new model. Figures 33, 34 and 35 shows the results of the statistical analyses using Brocher, Castagna et. al. and Han et al. models respectively. Comparing these outputs to that of the newly developed Vs model shows the later is a better predictor of the shear wave velocity. This is further confirmed by the RMSE values shown in table 4.

5.5.2 Well GB3 Shear Wave Velocity Validation

As done with the last section, the GB3 well also has shear wave velocity data acquired from about 4250 ft to approximately 6500 ft. Equation 5.5 was also applied to predict the shear wave velocity which was then compared to the acquired measured velocity. Similarly, Brocher, Castagna and Han et al. models were also applied to predict the shear wave velocity for this well. Figures 51 to 55 show the results of this exercise.

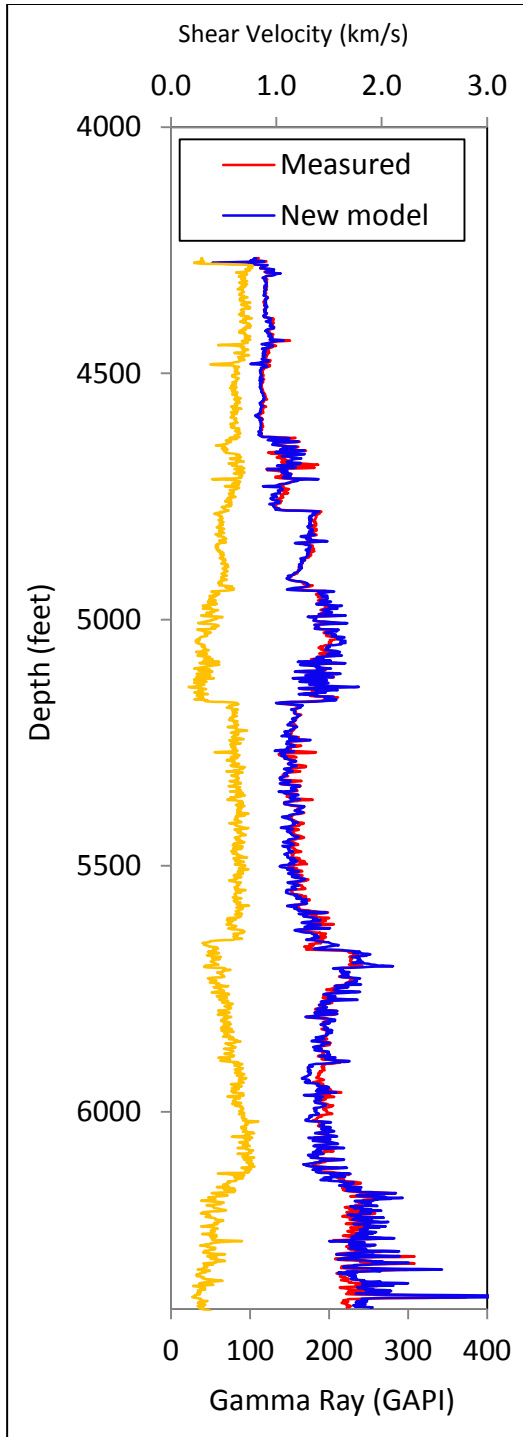


Figure 51: Well GB3 - Matching plots of new model with measured data with GR plot

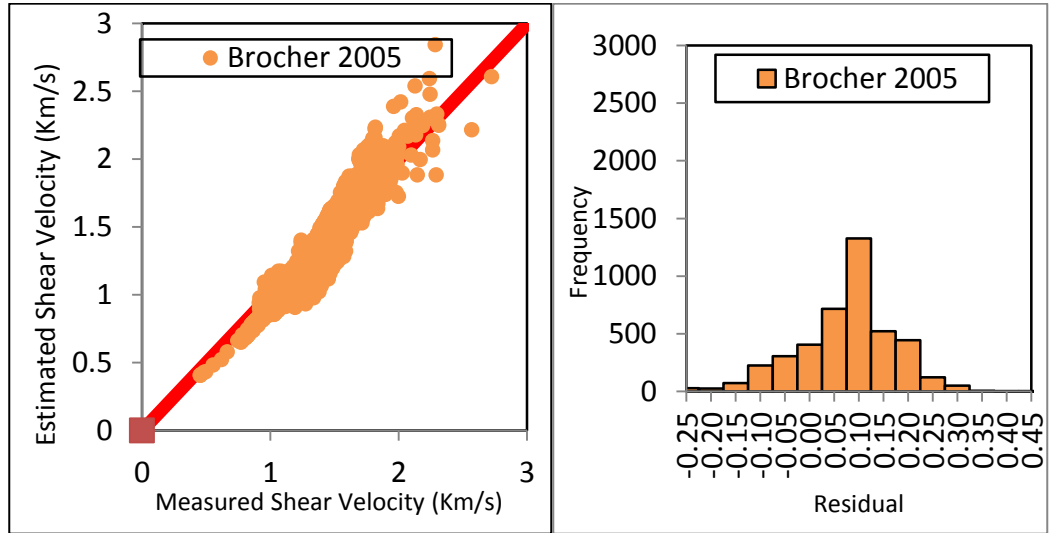


Figure 52: Well GB3 - Measured and Estimated Vs with Residual frequency for Brocher model

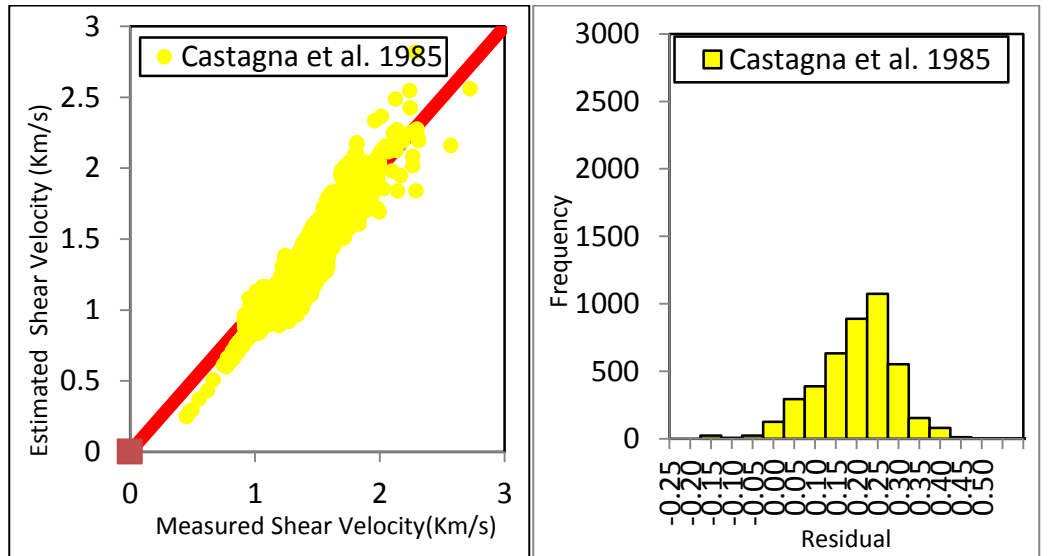


Figure 53: Well GB3 - Measured and Estimated Vs with Residual frequency for Castagna model

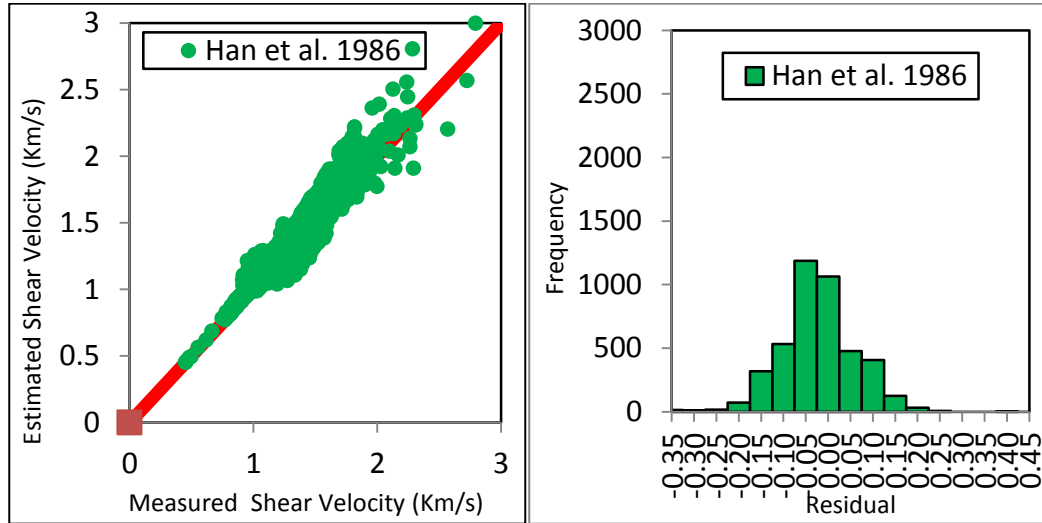


Figure 54: Well GB3 - Measured and Estimated Vs with Residual frequency for Han model

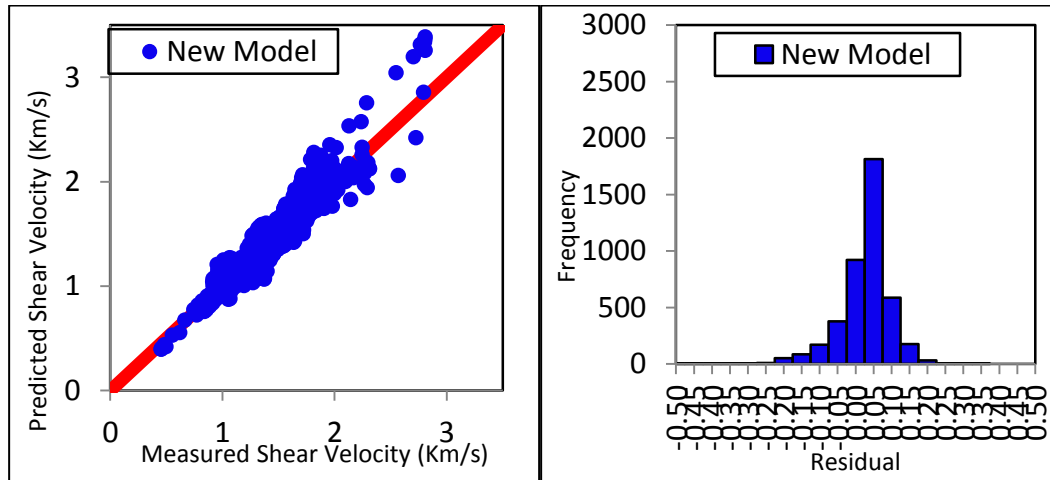


Figure 55: Well GB3 - Measured and Estimated Vs with Residual frequency for New model

5.5.3 Well GB4 Shear Wave Velocity Validation

The third selected well, GB4 well also has shear wave velocity data acquired from about 7450 ft to approximately 8900 ft. Equation 5.5 was also applied to predict the shear wave velocity which was then compared to the acquired measured velocity. Similarly and as done with previous two sub-sections, Brocher, Castagna and Han et al. models were also applied to predict the shear wave velocity for this well. Figures 56 to 60 shows the result of this exercise.

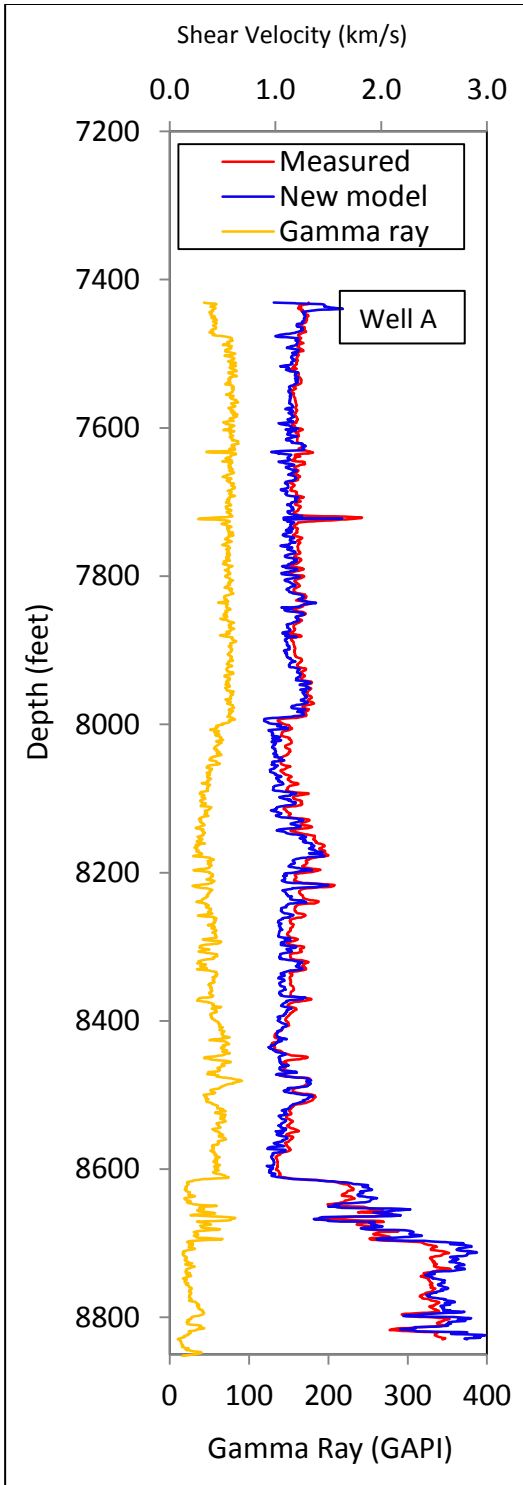


Figure 56: Well GB4 - Matching plots of new model with measured data with GR plot

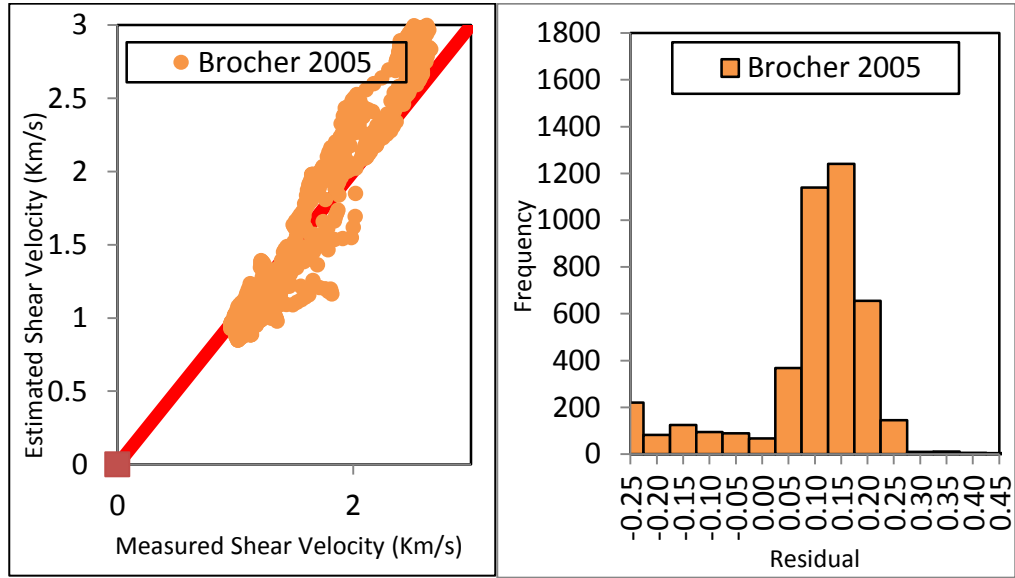


Figure 57: Well GB4 - Measured and Estimated Vs with Residual frequency for Brocher model

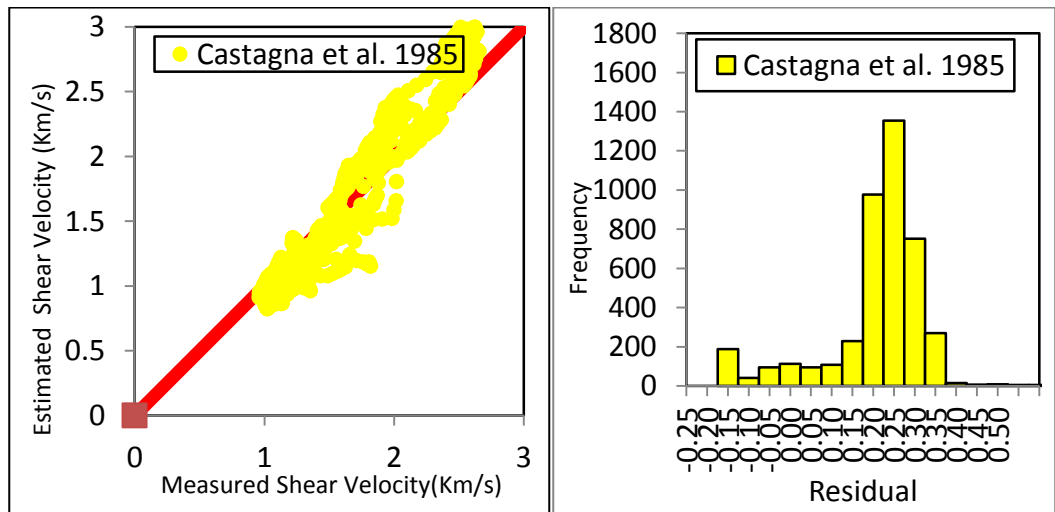


Figure 58: Well GB4 - Measured and Estimated Vs with Residual frequency for Castagna model

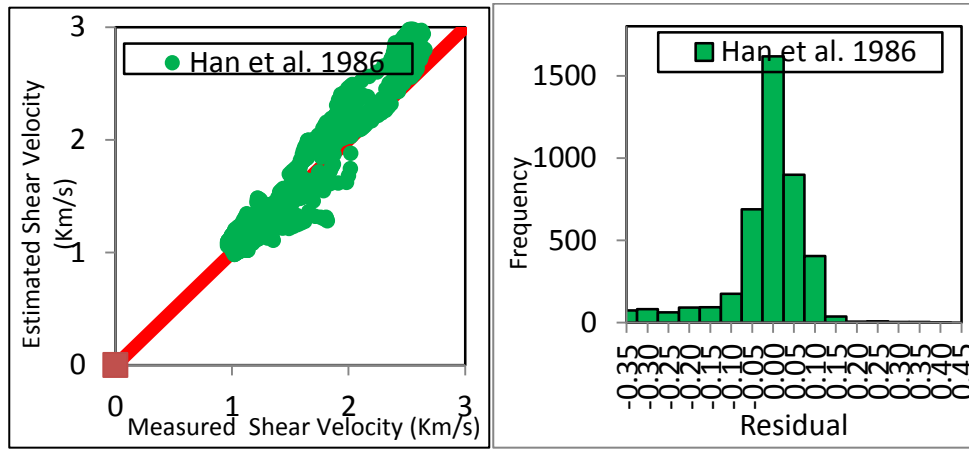


Figure 59: Well GB4 - Measured and Estimated Vs with Residual frequency for Han model

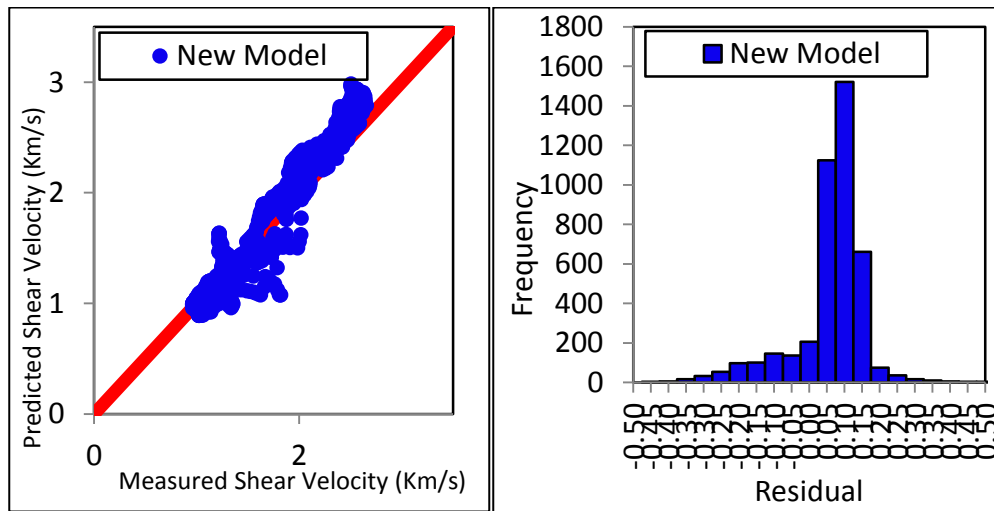


Figure 60: Well GB4 - Measured and Estimated Vs with Residual frequency for New model

5.6 Shear Wave Velocity Model Results Discussion

From the three well examples studied, it can be found that the developed shear wave velocity model outperform the prior models used for shear wave velocity prediction. The Root Mean Square error values from the three well examples were compared to the prior models as shown in table 5 below. From this table, it is evident that the empirically developed shear wave velocity model came out on-top with a better predicting power than the Han's, Brocher's and Castagna's models.

Table 5: RMSE Comparison - Developed Shear Wave Velocity Model and Prior Models

RMSE				
Wells	Developed Model	Han et al. (1986)	Brocher (2005)	Castagna et al. (1985)
GB2	0.098781	0.131038	0.139506	0.147665
GB3	0.07485	0.09751	0.11452	0.12279
GB4	0.11238	0.10567	0.15216	0.15391

5.7 Chapter Summary

The chapter showcases the steps and procedure taken in the derivation of the proposed shear wave velocity model for predicting the shear wave velocity when the compressional wave velocity data is acquired. Contrary to the previously used models which tend to derive shear wave velocity (V_s) prediction primarily from compressional wave velocity (V_p) data, the proposed empirical model incorporates the density term which makes the model much more robust in the prediction of the shear wave velocity. The results and analysis proved that in deriving V_s , the combination of V_s and ρ is more important than whether the formation is consolidated or unconsolidated. The new derived shear wave velocity model is found to be superior in prediction for the Grand Banks area when compared to Han et al. model, Brocher model and Castagna model.

Chapter 6

Poisson's Ratio Profile for the Grand Banks

6.1 Poisson's Ratio Correlation

Drilling engineers often obtain Poisson's ratio values from correlation derived from other areas around the world, which in some cases could be too high or too low depending on the region. The major aim of this chapter is to derive a Poisson's ratio correlation below the mud line for the sedimentary basins offshore Grand Banks. In this chapter, calculated Poisson's ratios are from V_p and V_s which were measured in the field from well logs.

Fracture pressure gradient predictions together with pore pressure gradient prediction are key elements for a successful casing design. They both dominate the applied load pressure. One of the main functions of a drilling engineer at the well design stage is to correctly predict the fracture pressure gradient (FPG) before designing any casing string.

Eaton's formula for fracture gradient calculation is given by the following equation:

$$FPG = \frac{\mu}{1-\mu} (G_{ob} - G_{pp}) + G_{pp} \quad (6.1)$$

where *FPG* is the formation fracture pressure gradient (psi/ft), G_{ob} is the overburden pressure gradient (psi/ft), G_{pp} is the pore pressure gradient (psi/ft), μ is the Poisson's ratio (dimensionless).

Poisson's ratio can be derived once the compressional and shear wave velocities (V_p & V_s) are known using the formula below.

$$\mu = \frac{V_p^2 - 2V_s^2}{2(V_p^2 - V_s^2)} \quad (6.2)$$

The Poisson's ratio in the equation must be determined precisely for the prospective area in order to effectively estimate the fracture pressure gradient. The higher the value of the Poisson's ratio of the sediment, the more the vertical matrix stress is transmitted in the horizontal direction, and therefore, the higher the fracture pressure gradient.

A generalized curve of Poisson's ratio profile for offshore Grand Banks area will be established below the mud line. In order to establish such, analyses was done using V_p and V_s data from dipole sonic Log data, Gamma Ray Log to separate

sand from shale sections, formation bulk density data for deriving the overburden gradients, as well as pore pressure data and Leak-off test (LOT) data.

6.2 Eaton Poisson's Ratio Profile Comparison

Three wells from three different basins were selected for this exercise. The Poisson's ratios as measured in the field for the three wells were plotted against depth. Poisson's ratio was estimated from shear wave velocity (V_p) and compressional wave velocity (V_s) as shown in equation 6.2 and then plotted together with the Eaton (1969) originally derived curve for the GOM as well as the curve later derived by Eaton and Eaton (1997) for deep water GOM. The various μ -D plots for the three cases are shown in figure 61 below. These wells were selected from the Orphan, Jeanne D'Aarc and Flemish Pass basins of the Grand banks.

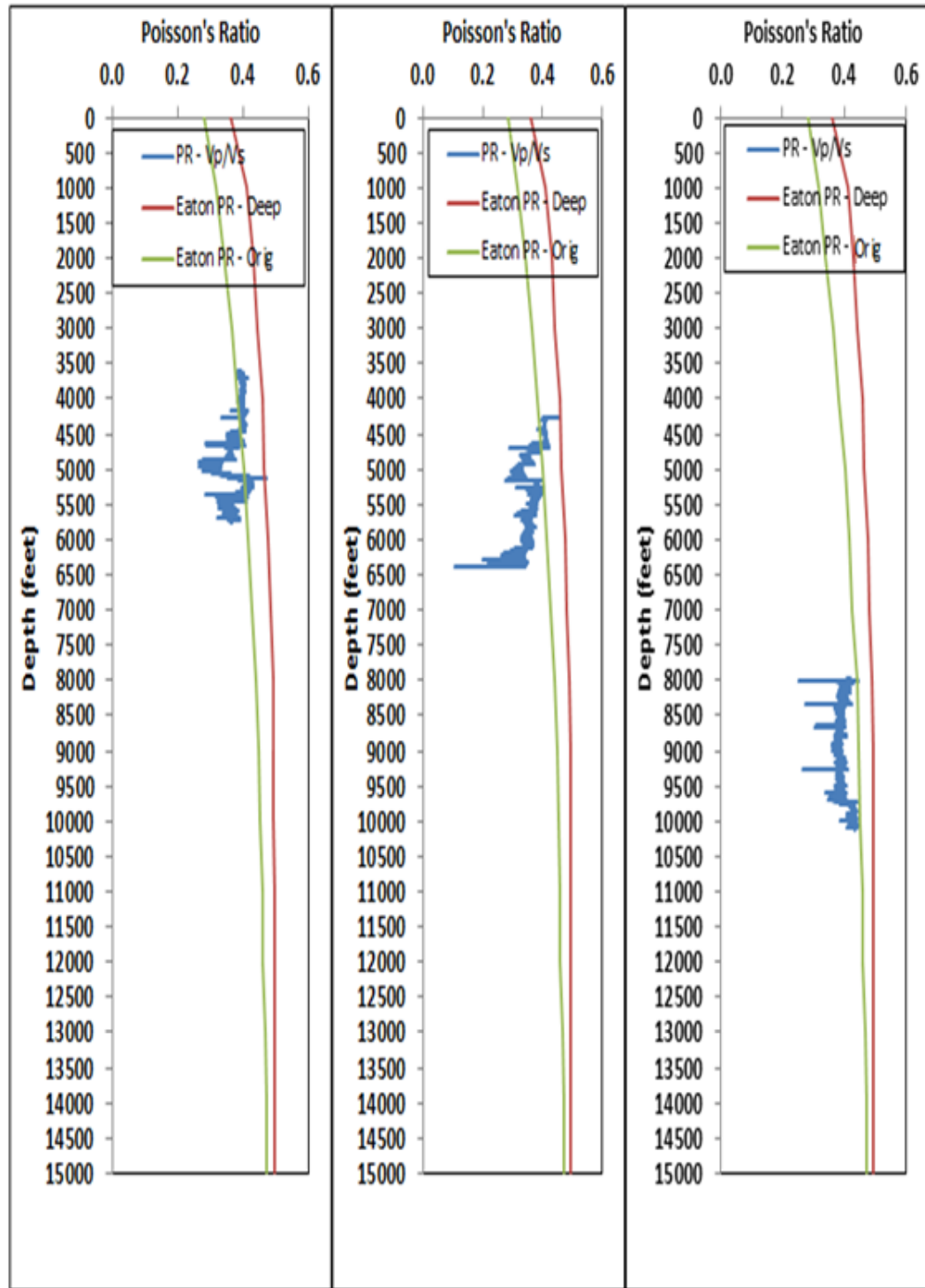


Figure 61: Poisson Ratio from Vp/Vs and Poisson Ratio trend from Eaton method, shown for three GB wells

As can be seen from figure 61, the Eaton curves are not particularly adequate for picking out Poisson's ratio values in a general sense for this offshore area. Also, since it is often expensive to log sonic tools during drilling or logging operations, it is practically impossible to obtain these values for the entire length of the well as can be seen for these three well scenarios. Hence, it is decided that a Poisson's ratio profile be specifically developed for the Grand Banks area ranging from the seabed to total depth (TD).

6.3 GB Regional Poisson's Ratio Profile Derivation

The following procedure, according to Eaton (1969) can be used to derive a Poisson's ratio profile for a specific area:

Step 1. Overburden stress gradient vs depth. Such data can be derived from bulk densities taken from logs, seismic data or shale density measurements. A plot of bulk density vs depth can then be converted to a plot of average overburden stress gradient vs depth.

Step 2. Actual fracture pressure gradients for several depths. These can be lost-circulation or squeeze data or actual fracturing data.

Step 3. Formation pressures that apply to the data in Item 2. (In Items 2 and 3, the depths must correspond.)

With these data and the Poisson's ratio equation, the Poisson's ratio curve for the area can be back-calculated and plotted vs depth. The result will be a curve similar to those developed by Eaton for the Gulf of Mexico (Figure 7). With these curves, fracture gradients can be predicted quite easily and quickly. These values can be plotted as a function of depth and the resulting curves can be used in all the drilling operations planning.

Three wells from different sub-basins with very good formation bulk density data were selected to be used in this analysis, even though it will be sufficient to use a single well. The reason being that it is expected that using wells from different areas will make the derived correlation much more robust and quite representative. With the bulk density data for the aligning wells, a depth-trend for the bulk density at every 100 ft is established from which the overburden pressure and overburden gradient are derived.

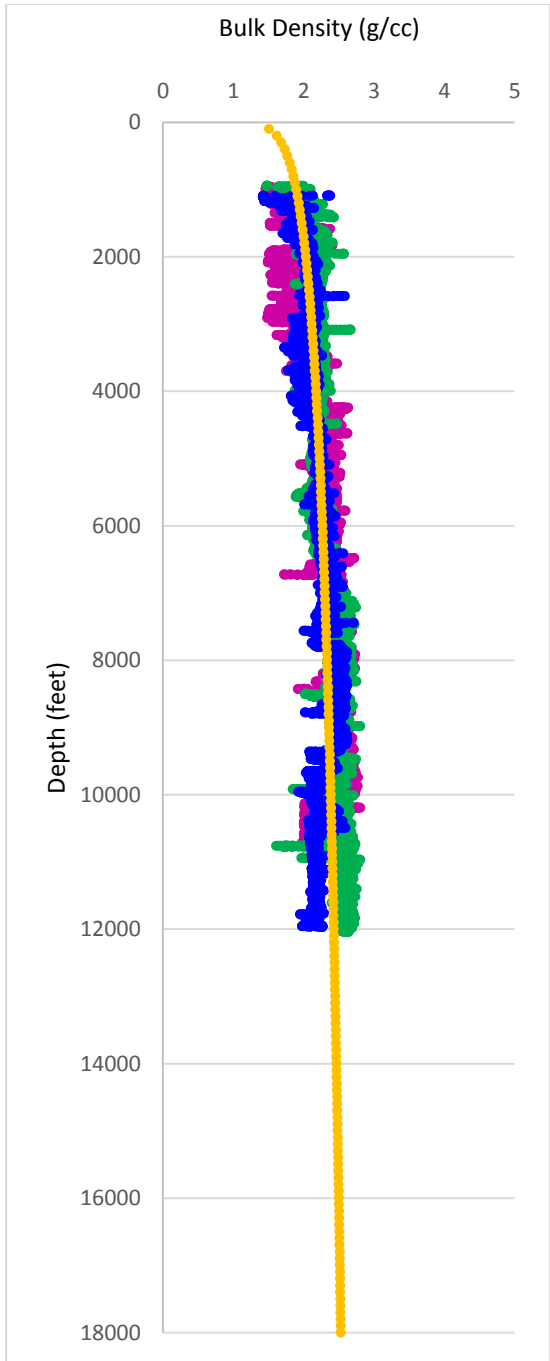


Figure 62: Bulk density trend from three Grand Banks Wells

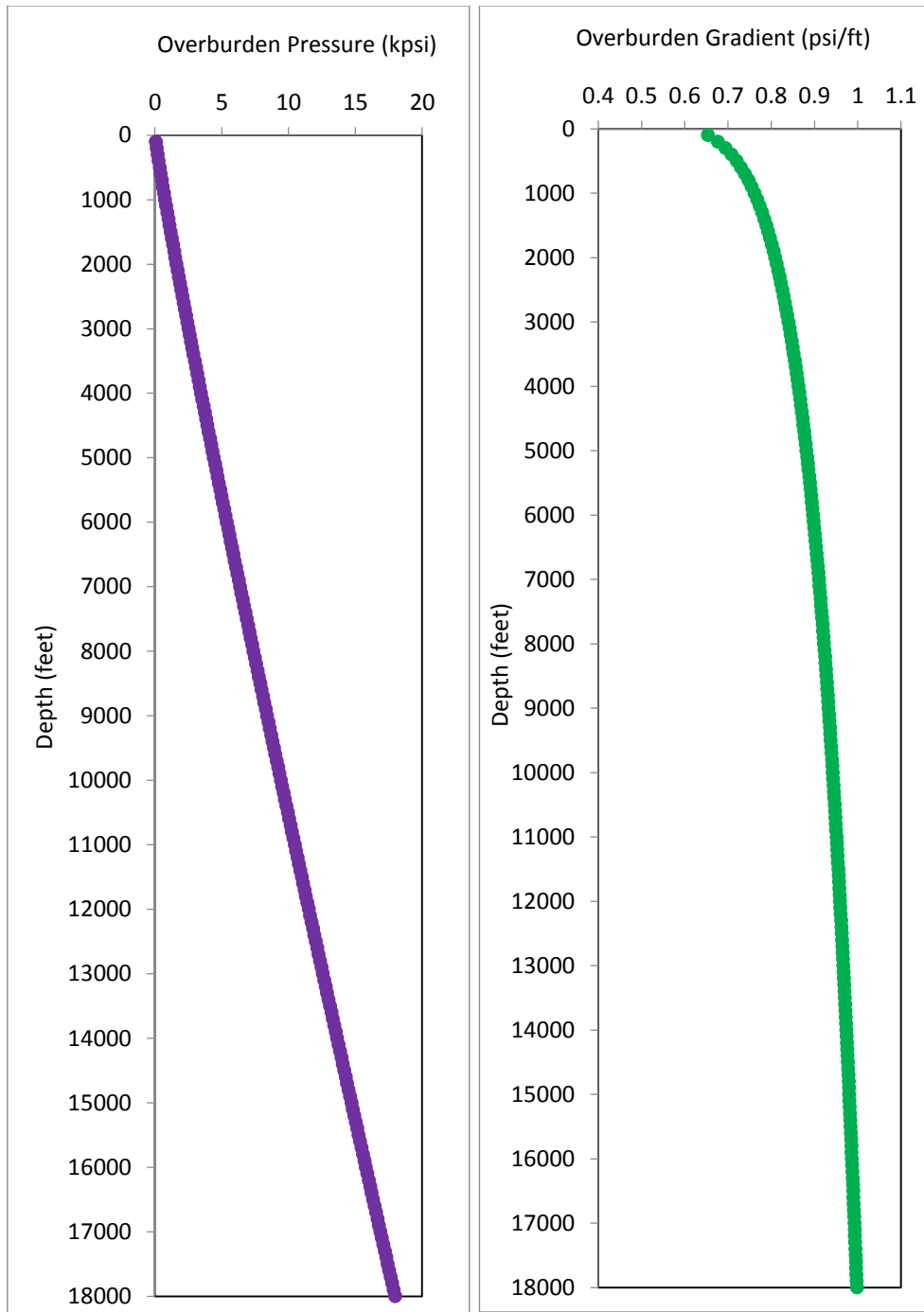


Figure 63: Overburden Pressure and Gradient derived from formation bulk density

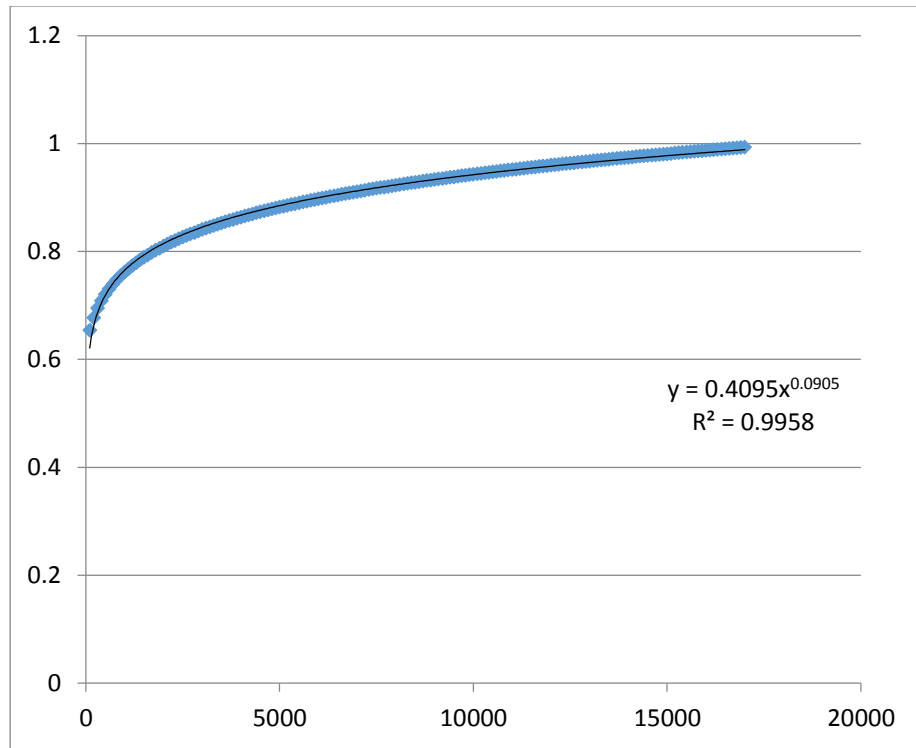


Figure 64: Derivation of Overburden Gradient - R-Squared and Equation

Figure 64 above shows the power law equation corresponding to the derived overburden gradient with very high coefficient of determination. With this equation, it is possible to know the values of the overburden gradient at every 100 ft. By completing steps 2 and 3 above using values of fracture pressure from Leak-Off test and the corresponding pore pressure values at the same depth, a Poisson's ratio trend for the Grand Bank is established as displayed in figure 65. With this and by knowing the values of the overburden gradient and pore pressure gradient, fracture pressure at these depths can be fairly estimated. The

power law model corresponding to the established Poisson's ratio trend is shown in equation 6.3.

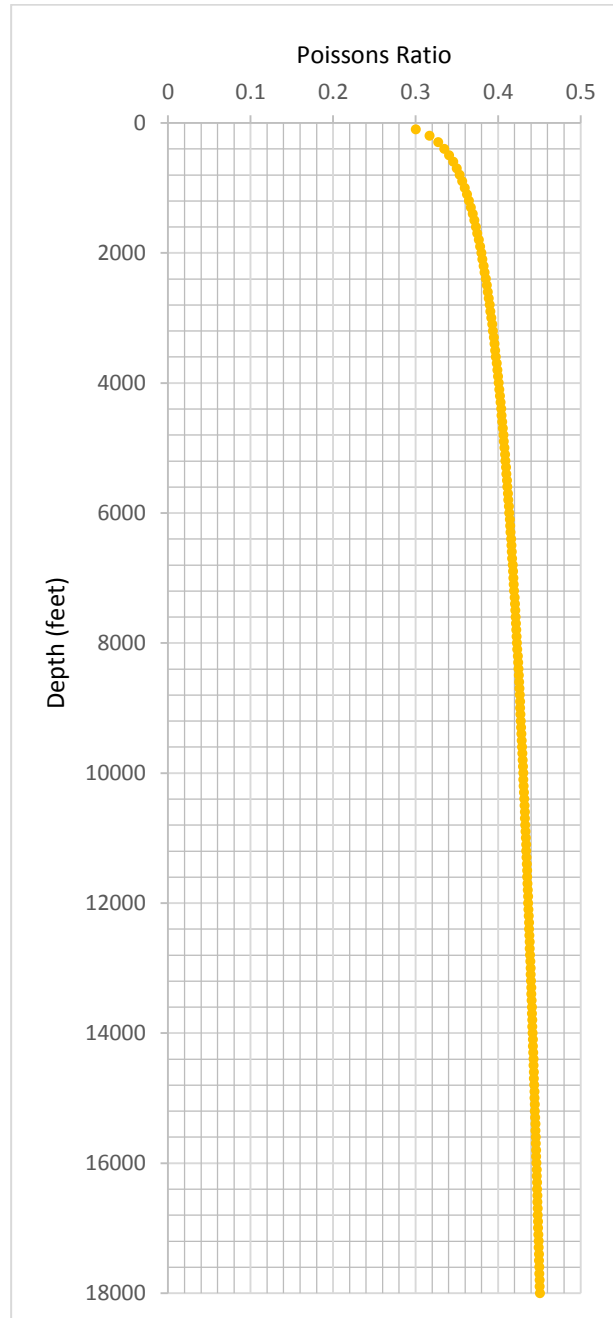


Figure 65: Established Poisson Ratio Trend for the Grand Banks Basins

$$PR = 0.21 D^{0.078} \quad (6.3)$$

where PR is Poisson's Ratio and D is depth in ft.

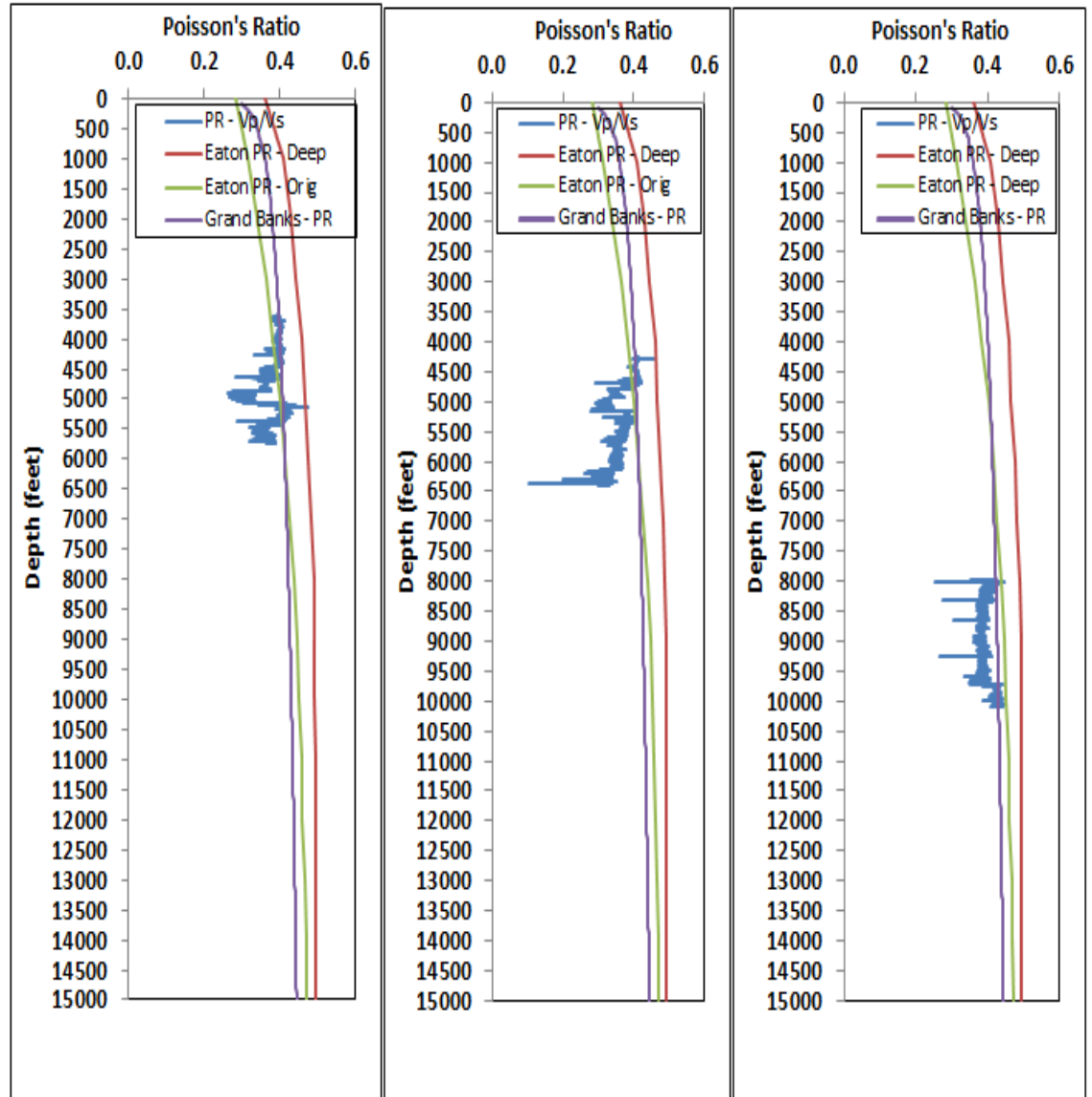


Figure 66: Grand Bank Basins Poisson Ratio trend, Poisson Ratio from V_p/V_s and Poisson Ratio trend from Eaton, shown for three GB wells

6.4 Fracture and Pore Pressure Prediction from Poisson's Ratio

Over the years, Fracture Pressure (FP) prediction for offshore Grand Banks has been based on correlations developed for offshore Gulf of Mexico (GOM). However, LOT data gathered across the basin from several wells signifies possible different trends. In this chapter, a new FP relationship for the Jeanne d'Arc basin, a basin which houses all current field development in the Grand Banks was discovered and presented.

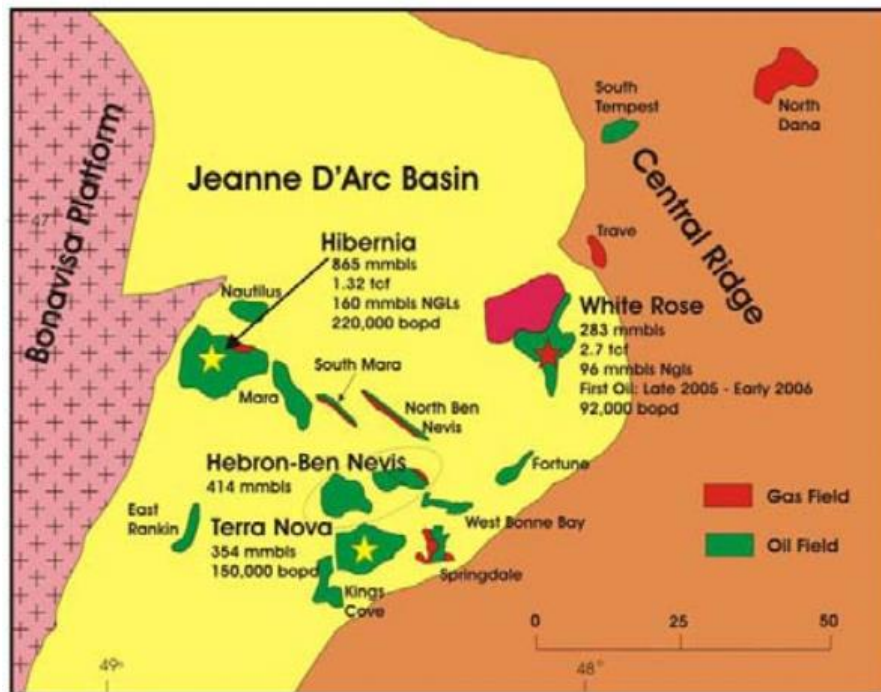


Figure 67: The Jeanne D'Arc Basin (Enachescu M.E., 2005)

This basin hosts all current development in the area and there is sufficient amount of data available to establish a correlation. LOT fracture pressure points and corresponding pore pressure at same depth for 93 offshore wells were utilized in the analysis. Recall from equation 6.1.

$$FPG = \frac{\mu}{1-\mu} (G_{ob} - G_{pp}) + G_{pp}$$

$$\text{Let } \frac{\mu}{1-\mu} = K$$

$$FPG = K (G_{ob} - G_{pp}) + G_{pp}$$

$$FPG = KG_{ob} - KG_{pp} + G_{pp}$$

$$FPG = KG_{ob} - G_{pp}(1 - K) \tag{6.4}$$

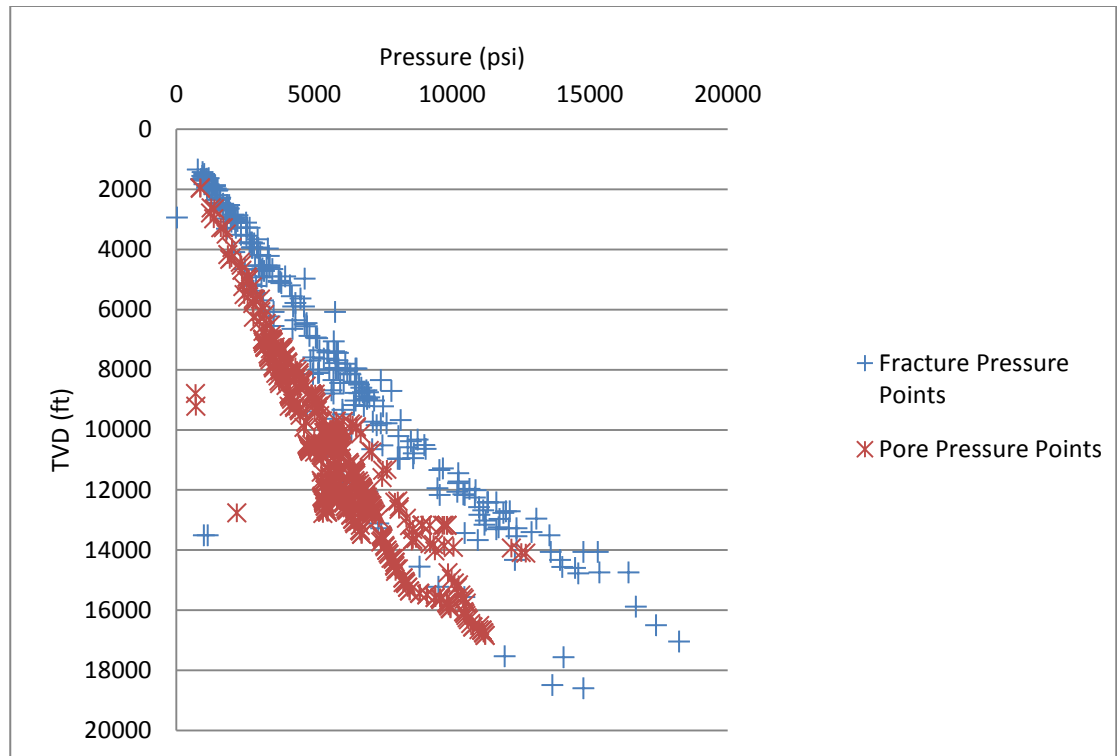


Figure 68: Fracture and Pore pressure data points for some Grand Bank Wells

Where FPG is the fracture pressure gradient, μ is Poisson's ratio, G_{pp} is the pore pressure gradient, G_{ob} is the overburden pressure gradient and K is a constant.

We can therefore establish fracture pressure gradient as a function of the pore pressure gradient and depth as shown in equation 6.5.

$$FPG = A f(D) + BG_{pp} \quad (6.5)$$

6.5 Fracture Pressure Correlation for the Jeanne d’Arc Basin

Pressure data were gathered from data repository available for pressure data for 93 wells. The pressure data were acquired from various wireline tools including RFT, MFT, and MDT. Good pressure data were quality controlled and separated from poor and noisy data before being used in this analysis. Wells from the Jeanne d’Arc basin from which LOT was carried out were gathered. Analysis continued by separating wells that has LOT data while at the same time have pore pressure data acquired at the same depth at which the fracture pressure data were obtained. Remarks from the logging reports were also considered to ensure the completeness of usefulness of each data points. Proceeding further with the ready to use QC data, the difference between the fracture pressure and pore pressure were estimated and plotted on the vertical axis against the depths corresponding to these data points on the horizontal axis as shown in figure 69.

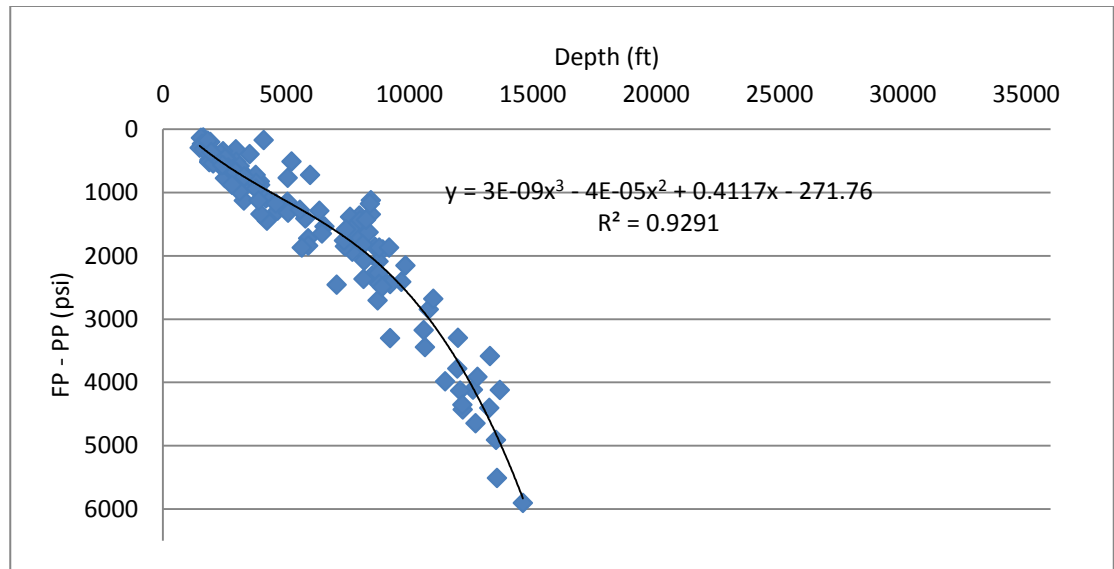


Figure 69: A new correlation for estimating Fracture pressure (FP), given the Pore Pressure (PP) and Depth (D).

From figure 69, in the Jeanne d’Arc basin, once the depth is known, it is possible to estimate the approximate value of the formation fracture pressure since the difference in fracture pressure and pore pressure can be determined. By knowing the pore pressure at those depths from the MDT data acquisition for example, the fracture pressures can be approximated for planning purposes. This relation is applicable to work only for the Jeanne D’Arc basin. The correlation discovered for the Jeanne d’Arc basin is a third order polynomial equation given below:

$$FP - PP = 0.000000003D^3 - 0.00004D^2 + 0.4117D + 271.76 \quad (6.6)$$

where FP is the fracture pressure, PP is the pore pressure and D is depth in ft.

6.6 Chapter Summary

The chapter describes the importance of Poisson's ratio as an elastic property useful in the estimation of fracture pressure gradient knowing the pore pressure gradient and the overburden gradient. Calculating Poisson's ratio from dipole sonic logs from the Grand Banks using readings from V_p and V_s was compared to the Eaton Poisson's Ratio trend. The Poisson's ratio from acquired V_p and V_s seems to vary very much from well to well and have the tendency to be influenced by fluctuating logging tool readings. Combining this with the fact that there appears to be a mismatch between Poisson's ratio from the dipole sonic logs and that from Eaton trend led to the need to establish a Poisson's ratio trend specific to the Grand Banks. The established Grand Banks Poisson's ratio trend match much more closely to that derived from measured V_p and V_s dipole sonic log readings.

The chapter explores fracture pressure and pore pressure data from the Grand banks with the aim of investigating a possible trend suitable for approximating the fracture pressure while knowing the pore pressure, for planning purposes when used in conjunction with other available subsurface information.

Chapter 7

Excess Pressure Methodology

7.1 Excess Pressure Methodology

Part of this chapter had been published. Pressure-depth (P-D) plots have been the standard method used in the petroleum industry for interpreting wireline test data which is used to estimate subsurface reservoir properties. Hydrostatic P-D plot is a plot of stabilized formation pressure and true vertical depth (TVD). This plot is used to evaluate subsurface fluids contacts as well as detect the presence of hydrocarbons. However, these plots can be very difficult to interpret, where sometimes the fluid pressure gradients can be very similar, appearing parallel to each other. Also, from pressure-depth plots, fluid density is often calculated from regression, in which case, pressure barriers or small subtle changes in fluid-density can go unnoticed. Thus, an uncertain fluid-density could be calculated from the trend. The Excess Pressure methodology removes the effect of a chosen fluid density, which improves the visualization of the very fine fluid-density differences or the presence of pressure barriers.

7.2 Field Data analyses

The data were analyzed and quality-controlled (QC'd). The drawdown mobility was looked at for each scenario. Drawdown mobility is the ratio of the permeability of the formation to a fluid, to the fluid viscosity, where the higher the drawdown mobility, the more accurate is the test data (Lyons, 2010)

$$\lambda = \frac{k}{\mu} \quad (7.1)$$

Where λ = mobility, md/cp, k = effective permeability of reservoir rock to a given fluid, md and μ = fluid viscosity, cp.

The good test data was measured using a Repeat Formation Tester (RFT), Final Shut-In (FSI). Accurate pressure measurements were provided by the Crystal Quartz Gauge (CQG). The accuracy of the pressure gauge is believed to be in the range of ± 2.0 psi $\pm 0.01\%$ formation pressure which is approximately ± 13.8 kPa $\pm 0.01\%$. Once the good test data was QC'd using the MDT results, they were then used to create the P-D plot. The following sections will look at two individual wells drilled in the same reservoir, analyze the wells wireline test data as well as discuss the results from the P-D and EP plots.

7.2.1 Well GB5 Analysis

The P-D plot for well GB5 is shown below.

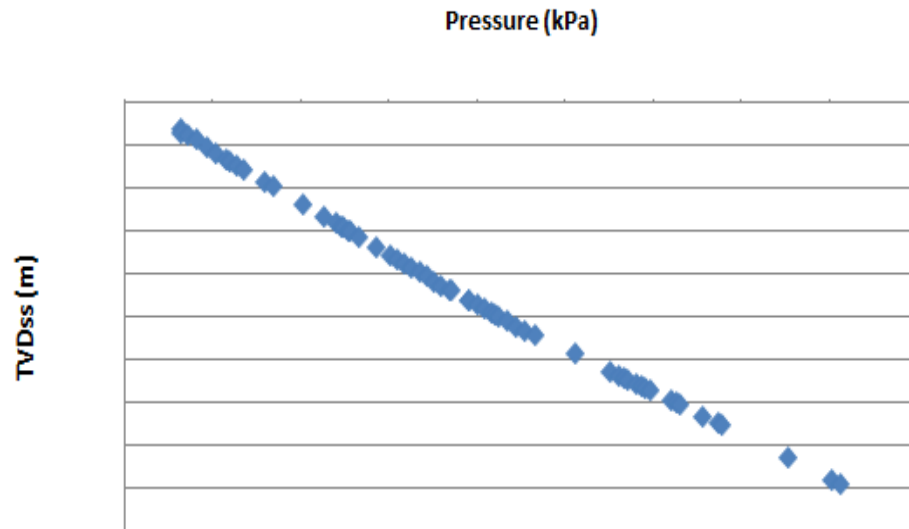


Figure 70: P-D Plot for Well GB5

To better understand the concept of pressure gradients, the first task was to find the hydrostatic gradient of the reservoir. The hydrostatic gradient of reservoir is the pressure exerted by the weight of a static column of the fluid. This was achieved by finding the slope of the line that intersected the oil trend line at the OWC.

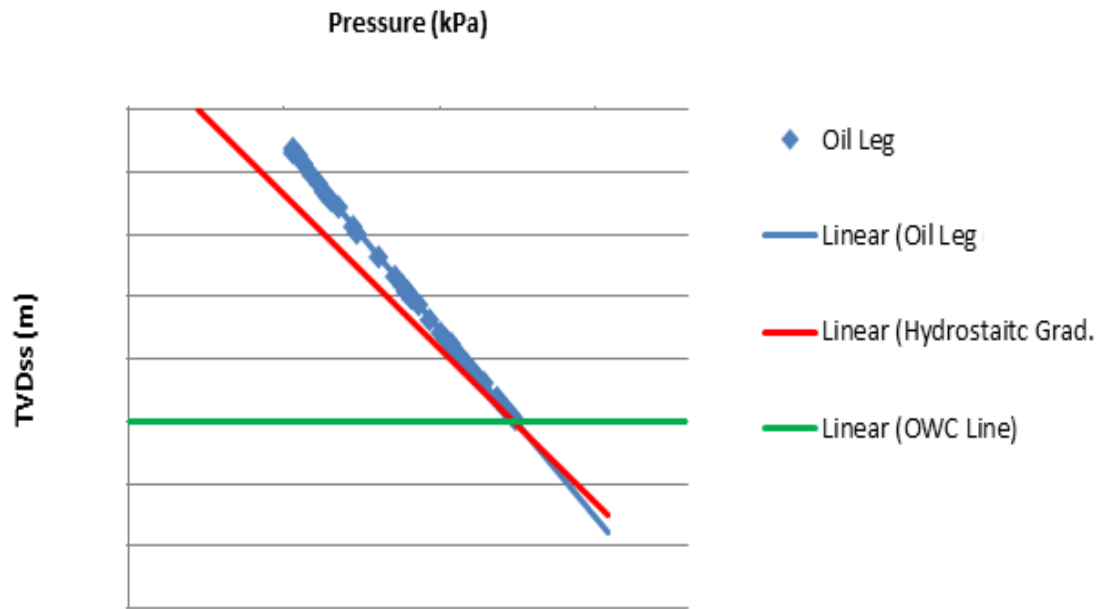


Figure 71: Well GB5 Hydrostatic and Oil Gradient

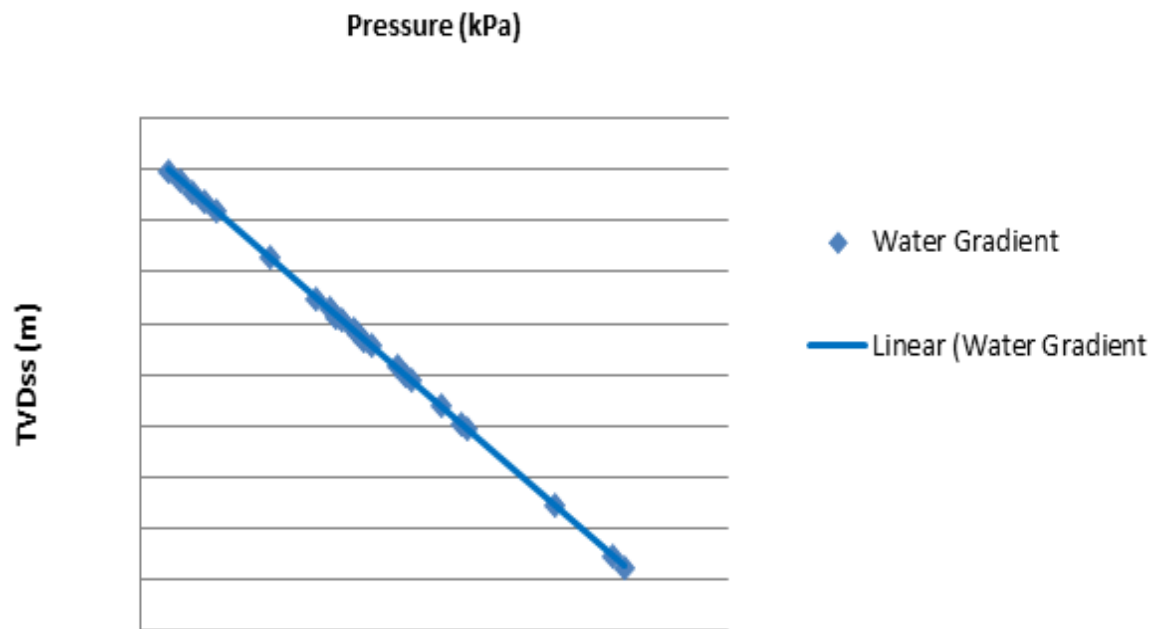


Figure 72: Well GB5 Water Gradient

Now that the oil and water gradient are determined, one is capable of creating the EP plot. In plotting the EP plots, the dominant fluids are either oil or water. First, the Excess Pressure using an assumed gradient of water was used. Once the initial values for Excess Pressure were plotted, density of the assumed pressure was iterated until the water leg created a vertical trend line, which can be seen in Figure 73.

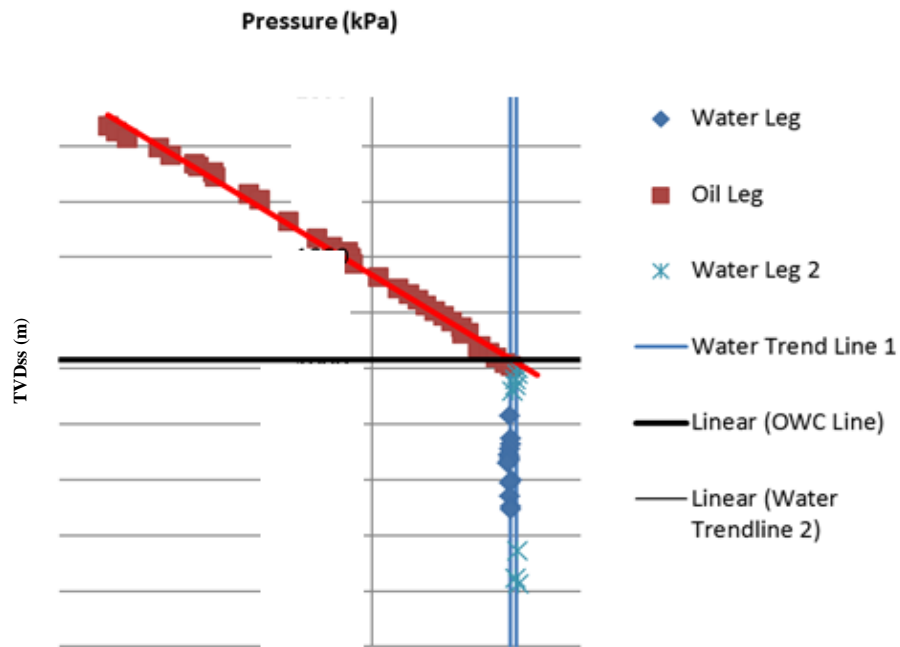


Figure 73: Well GB5 Water EP vs. TVD Plot

The oil leg is the red data points and the water leg is the blue data points. To create a vertical trend of the water leg, density had to be iterated into the calculation. In this case, since there is no separation between the last oil point

and the first water point, the FLW and OWC are assumed to be same. For now, the intersection of the oil and water trend lines will be considered the OWC. In the water leg, two distinct vertical trends can be seen. The difference in pressure between the trends is 2.43kPa. This is very well within the measured accuracy of the test gauge, however there is definitely a noticeable skew of the points, and it therefore should be noted. The two linear trends could represent a possible pressure barrier existing.

The next step was to plot an EP plot using the oil gradient as the assumed gradient. From Figure 74, three different trends can be observed in the oil leg, two of which (Oil Leg 2 and 3) are parallel to each other, again noting another possible pressure barrier.

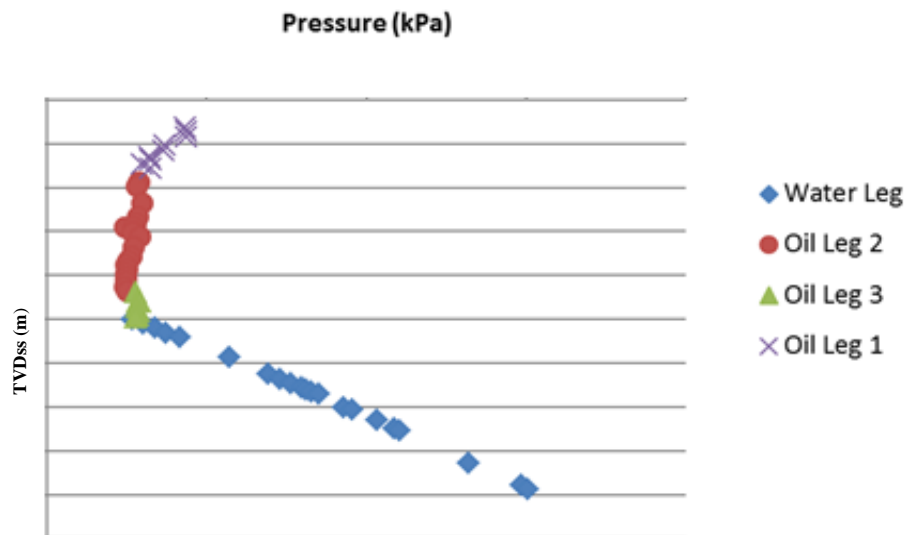


Figure 74: Well GB5 Oil EP vs. TVD Plot

Oil Leg 1 is at a sloped trend. However, this depth range matches up with another area in the reservoir. Plots were then created for Oil Leg 2 and Oil Leg 3 which are shown in Figures 75 and 76 respectively.

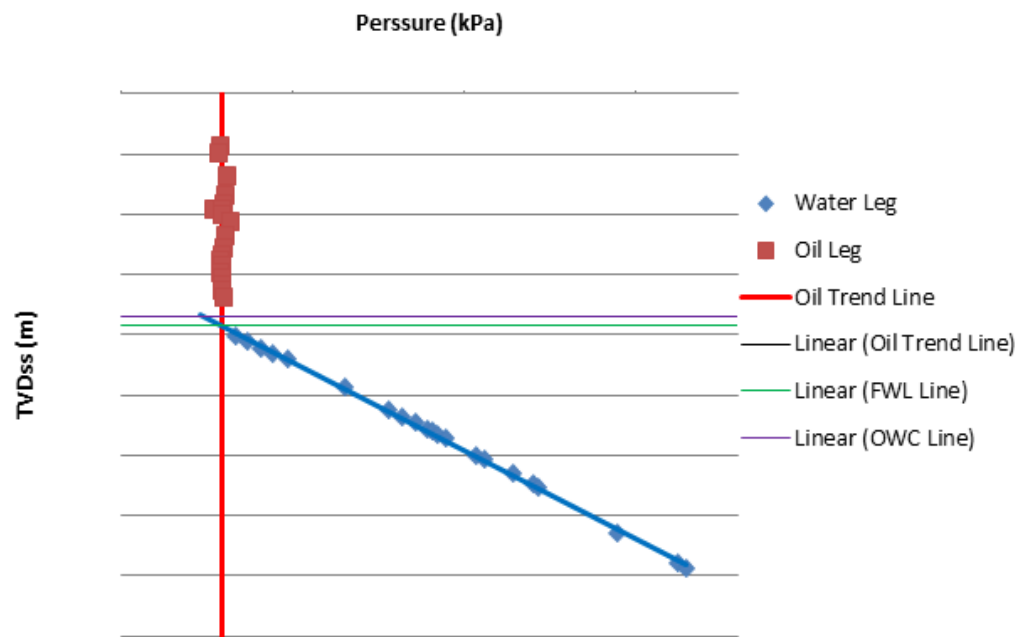


Figure 75: Well GB5 Oil Leg 2 EP vs. TVD Plot

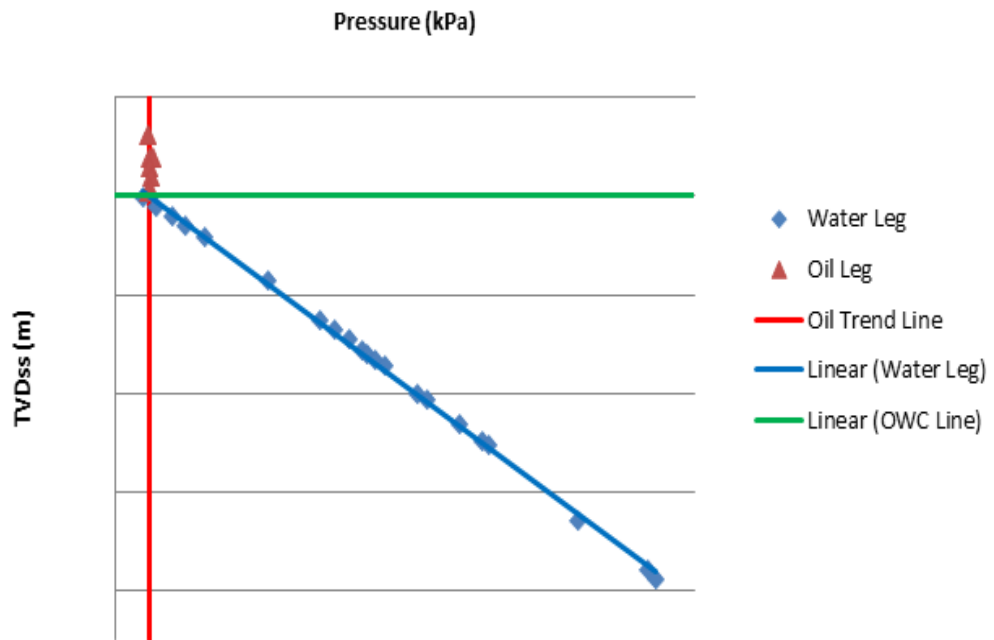


Figure 76: Well GB5 Oil Leg 3 EP vs. TVD Plot

7.2.2 Well GB6 Analysis

From the P-D plot displayed in Figure 77, two separate slopes can be identified. These two intervals were then separated to calculate the oil and water pressure gradients

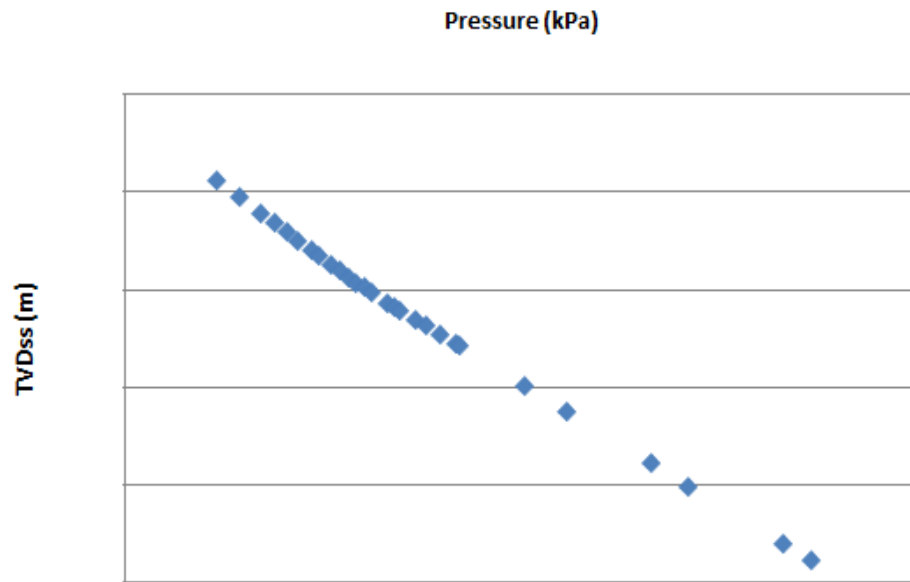


Figure 77: P-D Plot for Well GB6

The first slope data range is visible at the upper part of the P-D plot. This interval is assumed to be the oil leg. Again for the practice of calculating pressure gradients, the hydrostatic gradient was done using the approximate depth of where the two slopes diverge.

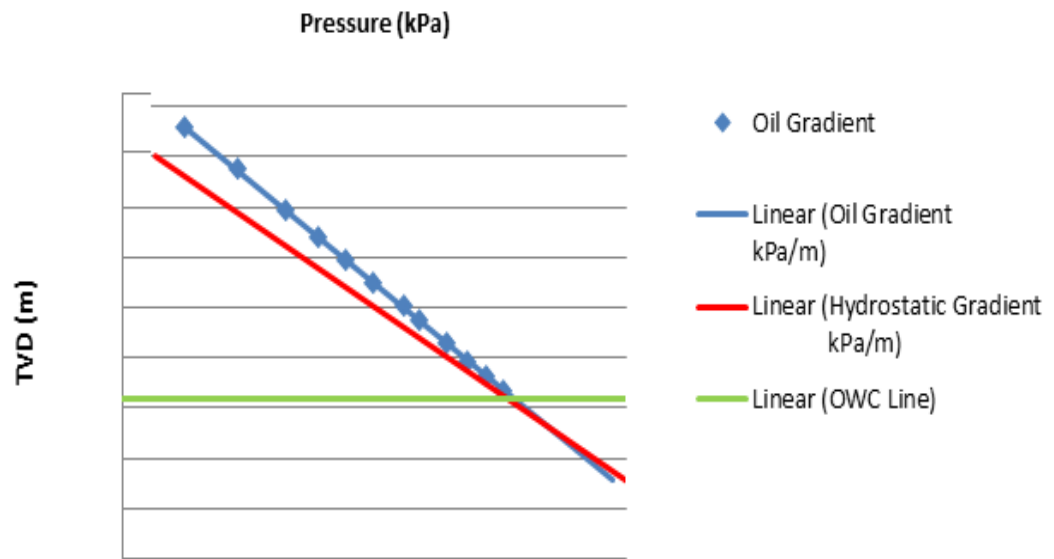


Figure 78: Well GB6 Hydrostatic and Oil Gradient

The water gradient was calculated using the pressure data in the water leg below the OWC.

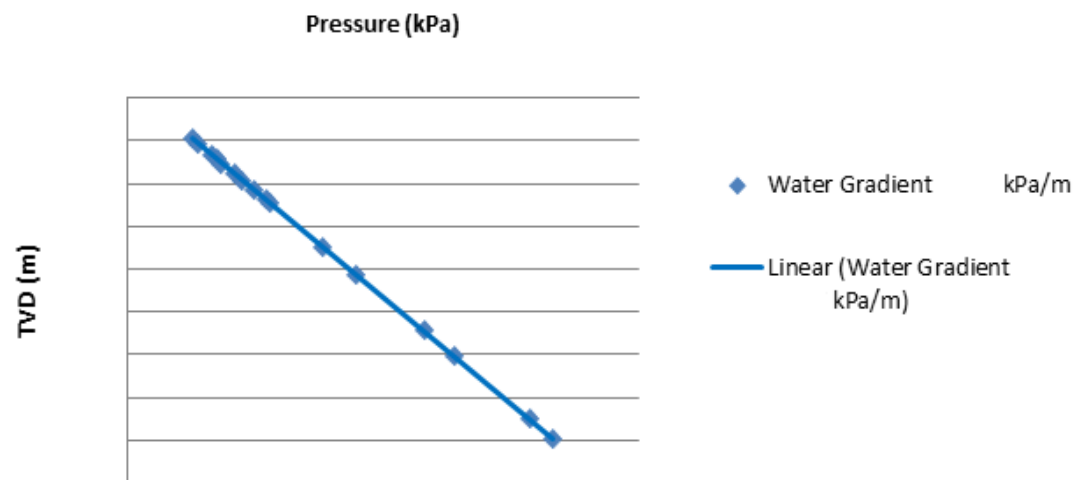


Figure 79: Well GB6 Hydrostatic and Oil Gradient

With the oil and water gradients calculated from the P-D plots, we were able to create the EP plots by the methods previously described. First, the EP plot for water was created which can be seen in Figure 80, using an assumed gradient equal to that of the water gradient from the well. The plot is correct once a vertical trend is created for the water leg.

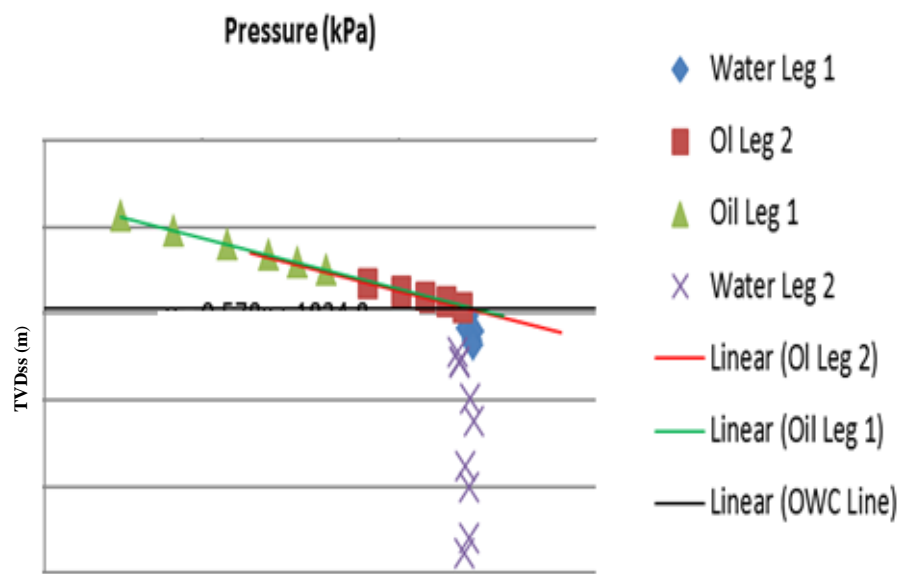


Figure 80: Well GB6 Water EP vs. TVD Plot

In the water leg, a possible pressure barrier may exist, whereby the blue diamond becomes the purple crosses. Here, there is an approximate separation of 3.7 kPa at around that depth interval. This is at a similar depth interval to the pressure barrier seen in the Well GB5 water EP plot. The oil leg was also

separated into two data trends since the oil EP plot showed a possible pressure barrier in the oil leg and it was further analyzed in the oil EP plot.

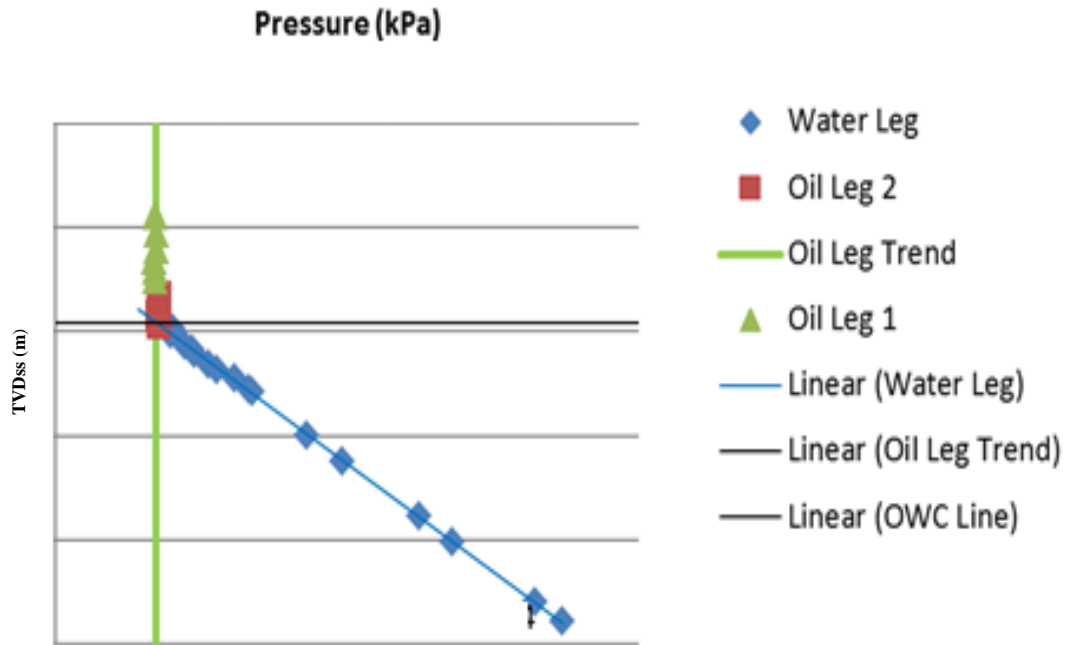


Figure 81: Well GB6 Oil EP vs. TVD Plot

In Figure 81, the two trends are depicted as the green and red data points. There is an approximate separation of 2.2 kPa occurring at mid-depth. This is not a large separation. However, pressure barriers have been identified at separations of less than 5 kPa (Brown, 2003). Again, this depth is very close to the depth of the potential pressure barrier in well GB5.

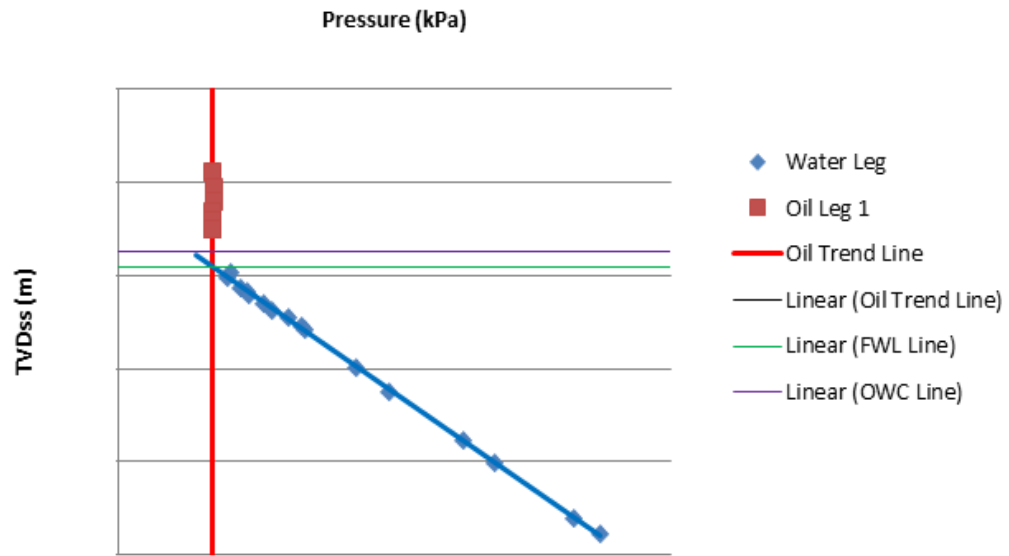


Figure 82: Well GB6 Oil Leg 1 EP vs. TVD Plot

To further analyze the different oil trends, EP plots were created using each oil leg trend. Figure 82 depicts the Excess Pressure plot that uses oil leg 1. From the plot, the water leg trend line and oil leg trend line intersect. This is considered the FWL, whereas the OWC occurs at the depth between the last oil point and the first water points.

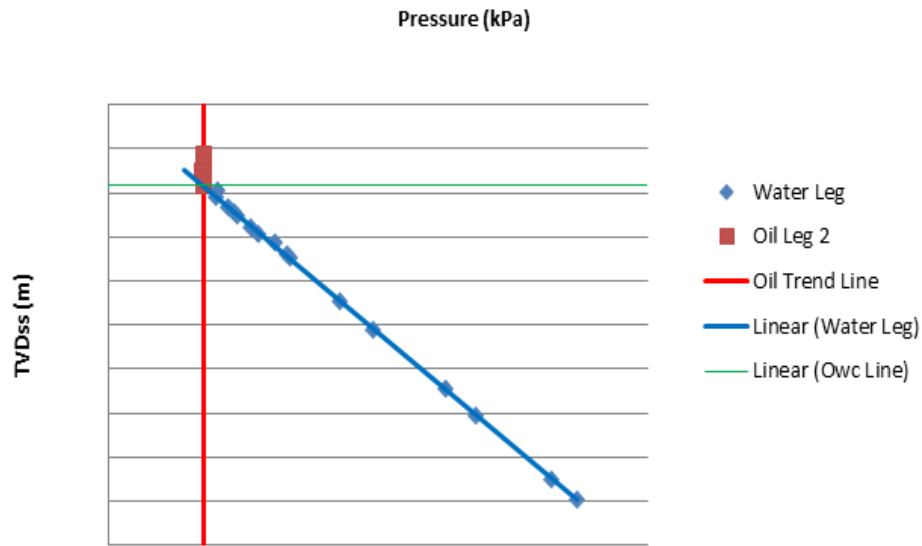


Figure 83: Well GB6 Oil Leg 2 EP vs. TVD Plot

In Figure 83, the trend line for Oil Leg 2 intersects the water trend line. This is considered the OWC since there is no depth between the last oil point and first water point.

7.3 Reservoir Compartmentalization

Since both wells GB5 and GB6 are in the same reservoir and both have good test data, their data were analyzed together to determine if there was any indication of compartmentalization. One way to determine if compartmentalization exists is to plot the oil leg and water leg of both wells on an EP plot. This is achieved by using the oil and water gradient of one of the

wells to calculate the assumed pressure of both wells. For instance, in one of the cases, the plot was created using the oil and water gradient of well GB6. Looking at the water legs of both wells, a difference of 21 kPa can be seen between the maximum and minimum pressure data point. Therefore, for accuracy of the data, one can assume a calibration of approximately 21 kPa. Now, looking at the oil legs for both wells, a difference of 18.2 kPa can be observed. Referring to the calibration found from the water legs, an absolute difference of 2.8 kPa can be determined. This value is within the measurement accuracy of a CQG quartz gauge. However, if the drill test was perfectly accurate, a difference such as this must be considered significant. This could mean possible pressure barrier or slight compartmentalization.

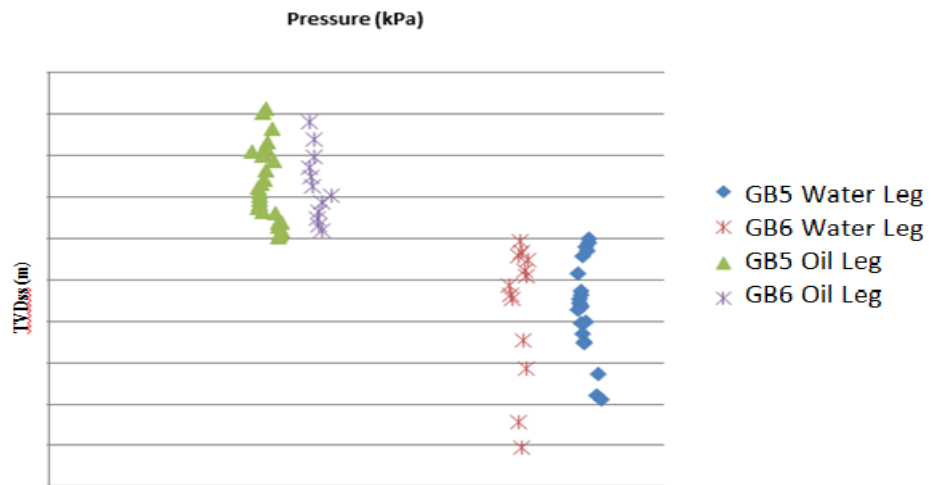


Figure 84: Compartmentalization Plot using Well GB6 gradients

For further analysis, an EP plot using the oil and water pressure gradients of well GB5 was used to test for compartmentalization. From Figure 85 the water legs have a difference of 19.6 kPa. Again, the pressure difference between the two water legs of the wells shall be used as the accuracy calibration value. In the oil legs, a difference of 16.9 kPa was determined between the maximum and minimum values. The absolute difference between these two values is 2.7 kPa. Again, this value could be significant if the drill test worked perfectly and may prove to be possible pressure barriers or compartmentalization.

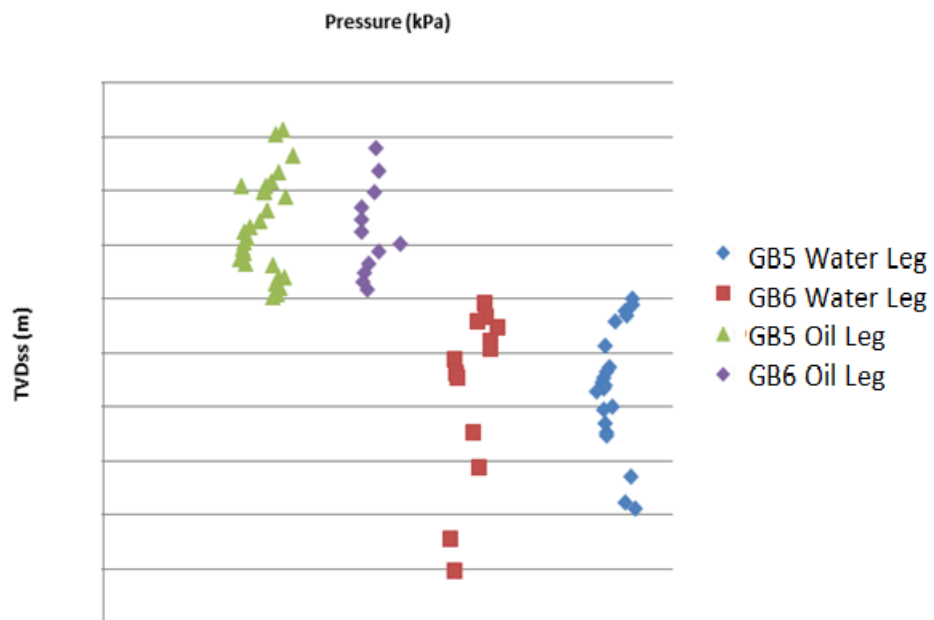


Figure 85: Compartmentalization Plot using Well GB5 gradients

7.4 Chapter Summary

Excess Pressure (EP) plots proved to be a valuable method for interpreting wireline pressure test data. The plots are much more effective in highlighting fluid contacts, pressure barriers, compartmentalization as well as obtaining fluid density. In both of the wells looked at in this chapter, a possible pressure barrier was present in both the oil and water legs, at similar depths. From analysis of compartmentalization, there were subtle pressure differences which could represent possible barriers or compartmentalization. The outputs from the EP plots prove very useful in supporting reservoir analyses, discovering potential new properties as well as providing vital information which could be further used to better characterize the reservoir.

Chapter 8

Conclusions and Recommendations

8.1 Conclusions

In this research, efforts were made to establish empirical models and correlations of elastic rock properties and geo-pressure using field case studies from the Grand Banks and the Niger Delta. It is expected that these models and correlations will lead to better well drilling planning as well as better definition of subsurface reservoir characteristics for effective modeling. In this thesis, the choice of wells and data used for various chapters were deliberate with sufficient considerations given to data availability and quality amongst other factors. The following conclusions can be drawn from this research:

- ❖ The calibrated sand-shale split Gardner-type correlation tested for the Grand Banks shows the need to consider an inclusive formation bulk density model. The fact that we have to rely on two separate equations with fairly low predictability coupled with the low coefficient of determination values and constant calibrations necessitates the need to develop a single robust and inclusive model.

- ❖ Formation bulk density is better predicted by incorporating components of mixed-lithology and micro-cracks. This is proven through the development of new prediction models (model method 1 and model method 2) applicable to mixed lithology and rocks with micro-cracks. Model method 2 was developed with siliciclastic environments in mind.
- ❖ Just like any of the existing empirical relationships, the new compressional velocity model may not be suitable for gas filled rocks. While the model method 2 is expected to work well in any siliciclastic settings, it does not cover carbonate and evaporite environments. However, the generalized form of the new model method 2 can be calibrated to regional carbonate and evaporite rocks to obtain the new set of models for these environments.
- ❖ A shear s-wave velocity model was proposed and found to have a superior predicting power when compared to prior s-wave velocity prediction models. The model which incorporates a density term for the estimation of shear s-wave velocity from compressional p-wave velocity is applicable to the Grand Banks.
- ❖ The Poisson's ratio - Depth trend that can be used to estimate Poisson's ratio values from seabed to total depth (TD) was established for the Grand Banks which enables the estimation of Poisson's ratio for

all drilled sections including sections where V_p and V_s data were not acquired.

The fracture pressure can be approximated from the new trend of fracture-pore pressures difference as a function of depth for well planning purpose for the Jeanne d'Arc basin of the Grand Banks. This can be implemented to other Grand Banks basins whenever more wells have been drilled and more PP and FP data at same depth are acquired.

- ❖ The Excess Pressure methodology for subsurface properties estimation was successfully utilized to highlight the subtle pressure differences which could represent possible pressure barriers or compartmentalization. These plots are useful in supporting reservoir analyses, discovering potential new properties as well as providing vital information which could be further used to better characterize the reservoir

8.2 Recommendations

The following are recommended for future work:

- ❖ A pure physics model which could incorporate principles of rock physics could assist in strengthening the outputs of the empirical models developed for formation bulk density and shear wave velocity.
- ❖ The available experimental data onto which part of the empirical correlation is calibrated where carried out using rock samples for other regions. Since different rock samples from various regions sometimes tend to exhibit differing properties, repeating and expanding such experiments for rock samples acquired from the Grand Banks and Niger Delta will be invaluable.

Appendix A

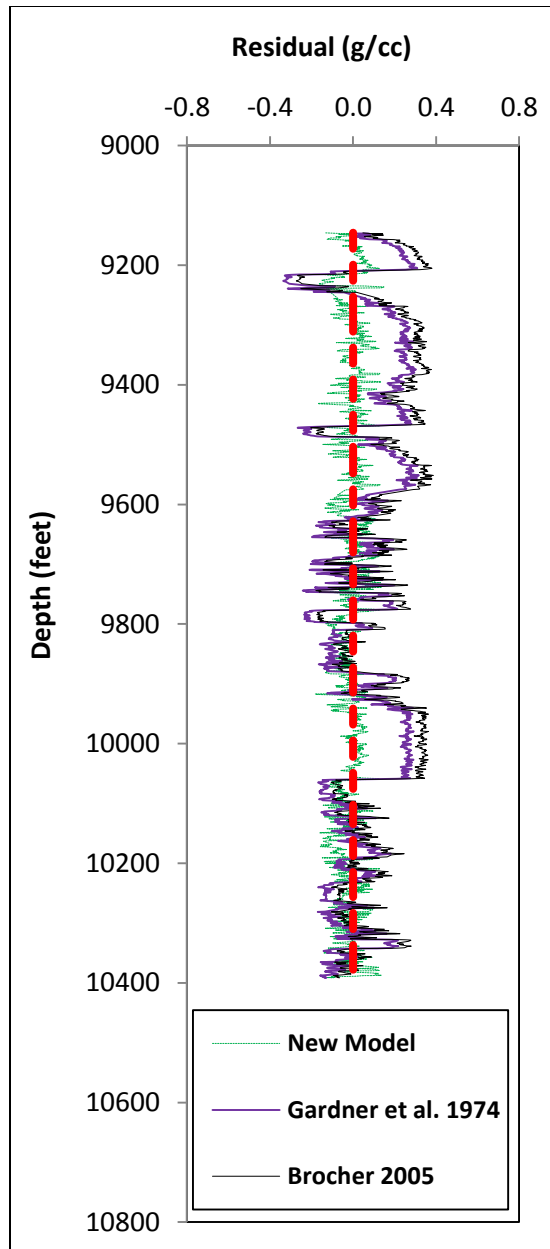
Laboratory Data and Miscellaneous Plots for Vp and Vs Models

Han's (1986) Laboratory Data

Sample	DW	Clay	5 Mpa		10 Mpa		20 Mpa		30 Mpa		40 Mpa	
			Vp	Vs	Vp	Vs	Vp	Vs	Vp	Vs	Vp	Vs
1	2.33	0	4.26	2.53	4.44	2.69	4.58	2.84	4.64	2.89	4.66	2.91
2	2.31	0	4.08	2.39	4.27	2.54	4.34	2.66	4.4	2.7	4.42	2.72
3	2.53	0	5.15	3.17	5.27	3.39	5.42	3.49	5.47	3.56	5.52	3.6
4	2.39	0	4.61	2.91	4.71	3.01	4.76	3.06	4.78	3.08	4.81	3.1
5	2.32	0	4.16	2.59	4.32	2.73	4.4	2.81	4.43	2.82	4.46	2.85
6	2.25	0.1	3.43	2.02	3.49	2.1	3.58	2.16	3.64	2.2	3.68	2.22
7	2.24	0.16	3.02	1.72	3.15	1.81	3.22	1.91	3.29	1.97	3.36	1.99
8	2.24	0.1	3.35	1.92	3.47	2.03	3.58	2.1	3.64	2.15	3.69	2.17
9	2.38	0.28	3.51	1.88	3.59	1.96	3.71	2.02	3.77	2.05	3.82	2.07
10	2.45	0.06	4.57	2.85	4.62	2.89	4.66	2.93	4.7	2.96	4.73	3
11	2.23	0.04	3.58	2.01	3.74	2.17	3.84	2.29	3.89	2.33	3.92	2.35
12	2.38	0.03	4.4	2.62	4.45	2.69	4.51	2.74	4.55	2.78	4.6	2.81
13	2.47	0.05	4.37	2.56	4.5	2.68	4.61	2.8	4.68	2.85	4.73	2.89
14	2.18	0.06	3.56	1.98	3.63	2.01	3.69	2.05	3.72	2.07	3.74	2.08
15	2.53	0.07	4.9	2.94	4.99	3.02	5.09	3.09	5.16	3.14	5.2	3.17
16	2.41	0.27	3.67	1.94	3.79	2.03	3.93	2.15	4.01	2.2	4.06	2.24
17	2.36	0.06	4.02	2.33	4.13	2.44	4.22	2.52	4.26	2.54	4.3	2.57
18	2.25	0.16	3.24	1.81	3.34	1.91	3.43	1.98	3.49	2.02	3.54	2.05
19	2.5	0.06	4.81	3	4.83	3.04	4.88	3.08	4.91	3.1	4.94	3.12
20	2.47	0.14	3.85	2.14	3.96	2.21	4.07	2.31	4.17	2.37	4.23	2.41
21	2.35	0.06	4.03	2.35	4.14	2.46	4.23	2.55	4.28	2.59	4.32	2.62
22	2.28	0.04	3.58	2.08	3.73	2.18	3.91	2.3	3.98	2.36	4.03	2.4
23	2.34	0.05	3.79	2.16	3.94	2.28	4.08	2.41	4.14	2.47	4.18	2.5
24	2.57	0.08	4.41	2.68	4.51	2.77	4.6	2.86	4.65	2.9	4.69	2.94
25	2.57	0.08	4.65	2.82	4.72	2.91	4.8	2.98	4.85	3.02	4.88	3.05
26	2.27	0.03	3.58	2.15	3.69	2.24	3.79	2.3	3.84	2.34	3.89	2.37

27	2.34	0.06	3.71	2.15	3.92	2.33	4.04	2.43	4.11	2.49	4.15	2.51
28	2.3	0.03	3.66	2.13	3.77	2.23	3.86	2.32	3.91	2.37	3.95	2.39
29	2.28	0.06	3.7	2.11	3.85	2.26	3.94	2.33	4	2.37	4.03	2.4
30	2.31	0.09	3.73	2.23	3.86	2.35	3.98	2.45	4.04	2.5	4.08	2.54
31	2.51	0.13	4.18	2.4	4.34	2.53	4.48	2.65	4.58	2.75	4.62	2.8
32	2.57	0.13	4.3	2.42	4.52	2.52	4.57	2.66	4.76	2.75	4.77	2.8
33	2.55	0.12	4.32	2.38	4.57	2.87	4.72	3.03	4.77	3.19	4.78	3.23
34	2.54	0.13	4.45	2.29	4.54	2.41	4.67	2.49	4.72	2.6	4.79	2.67
35	2.56	0.12	4.63	2.59	4.8	2.77	4.95	2.9	4.99	3.02	5	3.13
36	2.61	0.15	4.92	3.06	5.11	3.14	5.18	3.18	5.22	3.23	5.23	3.26
37	2.57	0.07	4.73	2.61	4.88	2.75	4.97	2.97	5.09	3.07	5.23	3.09
38	2.54	0.18	4.66	2.73	4.82	2.84	4.99	2.99	5.06	3.09	5.13	3.13
39	2.62	0.15	4.87	2.9	5	2.95	5.08	3.06	5.1	3.09	5.11	3.1
40	2.61	0.15	4.44	2.51	4.53	2.6	4.61	2.7	4.6	2.72	4.69	2.73
41	2.55	0.38	4.11	2.41	4.23	2.49	4.3	2.56	4.33	2.59	4.37	2.62
42	2.56	0.4	4.04	2.3	4.1	2.36	4.16	2.41	4.21	2.46	4.24	2.49
43	2.49	0.37	3.81	2.13	3.91	2.22	3.99	2.28	4.04	2.3	4.08	2.34
44	2.53	0.4	3.97	2.29	4.06	2.38	4.16	2.45	4.21	2.5	4.24	2.52
45	2.55	0.35	3.89	2.2	3.97	2.28	4.05	2.35	4.12	2.4	4.17	2.43
46	2.57	0.45	4.03	2.3	4.12	2.39	4.22	2.48	4.28	2.53	4.32	2.57
47	2.41	0.13	3.92	2.23	4.1	2.39	4.31	2.54	4.4	2.6	4.47	2.64
48	2.42	0.14	3.98	2.28	4.1	2.39	4.21	2.47	4.28	2.53	4.32	2.55
49	2.38	0.1	3.81	2.13	3.96	2.26	4.1	2.39	4.18	2.45	4.24	2.51
50	2.38	0.11	3.78	2.04	3.95	2.18	4.11	2.31	4.17	2.38	4.22	2.43
51	2.38	0.16	3.76	2.06	3.91	2.21	4.03	2.32	4.13	2.38	4.19	2.42
52	2.4	0.44	3.42	1.74	3.52	1.81	3.62	1.9	3.66	1.94	3.71	1.97
53	2.38	0.46	3.37	1.81	3.44	1.87	3.53	1.93	3.59	1.97	3.64	1.99
54	2.35	0.51	3.33	1.75	3.43	1.86	3.54	1.94	3.63	1.98	3.69	2.01
55	2.09	0.11	2.96	1.51	3.01	1.6	3.11	1.69	3.16	1.73	3.2	1.75
56	2.12	0.12	2.94	1.57	2.99	1.65	3.08	1.72	3.13	1.75	3.17	1.77
57	2.35	0.27	3.44	1.72	3.6	1.95	3.78	2.01	3.9	2.08	3.99	2.13
58	2.35	0.27	3.55	1.76	3.7	1.94	3.83	2.03	3.93	2.11	4	2.16
59	2.2	0.22	2.93	1.47	3.09	1.64	3.24	1.79	3.31	1.86	3.36	1.89
60	2.19	0.12	3.05	1.53	3.22	1.71	3.41	1.84	3.49	1.9	3.55	1.94
61	2.41	0.37	3.41	1.79	3.54	1.9	3.65	2	3.73	2.08	3.76	2.11
62	2.48	0.44	3.58	1.92	3.64	2	3.74	2.08	3.8	2.13	3.84	2.15
63	2.47	0.41	3.63	1.91	3.76	2	3.85	2.12	3.92	2.16	3.97	2.19
64	2.37	0.27	3.65	1.88	3.74	2.03	3.88	2.09	3.95	2.15	3.98	2.19
65	2.17	0.08	3.27	1.85	3.42	2	3.57	2.13	3.62	2.17	3.67	2.2

66	2.25	0.06	3.15	1.73	3.33	1.84	3.5	2	3.56	2.06	3.61	2.09
67	2.12	0.11	3.12	1.66	3.28	1.84	3.46	1.98	3.52	2.03	3.58	2.07
68	2.17	0.07	2.98	1.5	3.13	1.75	3.33	1.89	3.43	1.95	3.5	1.99
69	2.14	0.07	3.04	1.6	3.23	1.91	3.43	1.96	3.53	2.05	3.58	2.09
70	2.29	0.11	3.32	1.76	3.48	1.91	3.69	2.08	3.81	2.17	3.88	2.23
71	2.47	0.21	3.71	2.09	3.9	2.18	4.08	2.32	4.19	2.42	4.25	2.48
72	2.39	0.06	3.96	2.16	4.17	2.36	4.42	2.53	4.54	2.66	4.61	2.73
73	2.47	0.23	3.91	2.14	4.09	2.3	4.27	2.46	4.35	2.55	4.42	2.61
74	2.64	0.24	4.1	2.28	4.31	2.54	4.44	2.64	4.56	2.72	4.6	2.77
75	2.38	0.18	3.67	2.02	3.85	2.17	3.93	2.27	4.01	2.32	4.07	2.37



Typical Residual Errors Verification

Appendix B

Pressure Data for Jeanne D'Arc Wells (NRC, 2018)

Hebron Sample Well Pressure Data

Depth (M)	Pressure (KPA)	Testing Type	Pressure Type	Remarks
128	1369	DMR	HP	
184	1967	DMR	HP	
608	6501	DMR	HP	
1285.5	13140	FLOT#01	HP	
1285.5	23116	FLOT#01	LOP	
1301	13911	DMR	HP	
1723.1	17240	RFT#01-85	FSI	GOOD TEST
1723.1	19780	RFT#01-85	IH	
1724.7	17255	RFT#01-84	FSI	GOOD TEST
1724.7	19796	RFT#01-84	IH	
1726.3	17270	RFT#01-83	FSI	GOOD TEST
1726.3	19814	RFT#01-83	IH	
1728	17288	RFT#01-82	FSI	GOOD TEST
1728	19834	RFT#01-82	IH	
1795	20250	DMR	HP	
1867	18787	RFT#01-81	FSI	GOOD TEST
1867	21391	RFT#01-81	IH	
1875.5	18859	RFT#01-80	FSI	GOOD TEST
1875.5	21486	RFT#01-80	IH	
1882	21675	DMR	HP	
1883.5	18926	RFT#01-79	FSI	GOOD TEST
1883.5	21574	RFT#01-79	IH	
1889	18971	RFT#01-78	FSI	GOOD TEST
1889	21634	RFT#01-78	IH	
1893.5	19009	RFT#01-77	FSI	GOOD TEST
1893.5	21684	RFT#01-77	IH	
1898	19047	RFT#01-76	FSI	GOOD TEST
1898	21733	RFT#01-76	IH	
1902.5	19089	RFT#01-75	FSI	GOOD TEST

1902.5	21784	RFT#01-75	IH	
1905.5	19112	RFT#01-74	FSI	GOOD TEST
1905.5	21820	RFT#01-74	IH	
1910	19149	RFT#01-73	FSI	GOOD TEST
1910	21868	RFT#01-73	IH	
1913.5	19178	RFT#01-72	FSI	GOOD TEST
1913.5	21906	RFT#01-72	IH	
1916.6	19204	RFT#01-71	FSI	GOOD TEST
1916.6	21938	RFT#01-71	IH	
1919.5	19229	RFT#01-70	FSI	GOOD TEST
1919.5	21970	RFT#01-70	IH	
1921.7	19256	RFT#01-69	FSI	GOOD TEST
1921.7	21995	RFT#01-69	IH	
1924.5	19278	RFT#01-68	FSI	GOOD TEST
1924.5	22024	RFT#01-68	IH	
1925	21943	DMR	HP	
1927.4	22198	DMR	HP	
1929.5	19328	RFT#01-67	FSI	GOOD TEST
1929.5	22080	RFT#01-67	IH	
1931.5	19349	RFT#01-66	FSI	GOOD TEST
1931.5	22102	RFT#01-66	IH	
1933.5	19367	RFT#01-65	FSI	GOOD TEST
1933.5	22125	RFT#01-65	IH	
1938.5	19418	RFT#01-64	FSI	GOOD TEST
1938.5	22181	RFT#01-64	IH	
1941.5	19448	RFT#01-62	FSI	GOOD TEST
1941.5	22213	RFT#01-62	IH	
1945.5	19492	RFT#01-61	FSI	GOOD TEST
1945.5	22264	RFT#01-61	IH	
1950.5	19542	RFT#01-60	FSI	GOOD TEST
1950.5	22322	RFT#01-60	IH	
1952	19557	RFT#01-59	FSI	GOOD TEST
1952	22338	RFT#01-59	IH	
1965	0	RFT#01-57	FSI	DRY TEST
1965	22477	RFT#01-57	IH	
1972.5	19761	RFT#01-54	FSI	GOOD TEST - SAMPLE ATTEMPTED
1972.5	22560	RFT#01-54	IH	
1980.4	23274	DMR	HP	
1985.5	19891	RFT#01-53	FSI	GOOD TEST - SAMPLED

1985.5	22704	RFT#01-53	IH	
2011.7	20157	RFT#01-52	FSI	GOOD TEST
2011.7	22998	RFT#01-52	IH	
2023.7	20277	RFT#01-51	FSI	GOOD TEST
2023.7	23132	RFT#01-51	IH	
2028	22760	DMR	HP	
2053	20572	RFT#01-50	FSI	GOOD TEST
2053	23460	RFT#01-50	IH	
2062	20664	RFT#01-49	FSI	GOOD TEST
2062	23560	RFT#01-49	IH	
2387	26648	DMR	HP	
2595	28970	DMR	HP	
2644	29517	DMR	HP	
				GOOD TEST - SAMPLE ATTEMPTED
2789	28756	RFT#01-48	FSI	
2789	31728	RFT#01-48	IH	
2825	29082	RFT#01-47	FSI	GOOD TEST
2825	32121	RFT#01-47	IH	
2828.5	29177	RFT#01-46	FSI	GOOD TEST
2828.5	32145	RFT#01-46	IH	
2836.5	111	RFT#01-45	FSI	DRY TEST
2836.5	32234	RFT#01-45	IH	
2880	32152	DMR	HP	
2895	31878	RFT#01-44	FSI	GOOD TEST
2895	32888	RFT#01-44	IH	
2896.5	112	RFT#01-43	FSI	DRY TEST
2896.5	32904	RFT#01-43	IH	
2956	31169	RFT#01-42	FSI	GOOD TEST
2956	33569	RFT#01-42	IH	
2978	33246	DMR	HP	
2988	34061	DMR	HP	
2998.5	123	RFT#01-41	FSI	DRY TEST
2998.5	34041	RFT#01-41	IH	
3004.5	110	RFT#01-40	FSI	DRY TEST
3004.5	34106	RFT#01-40	IH	
3013	111	RFT#01-39	FSI	DRY TEST
3013	34203	RFT#01-39	IH	
3028	30549	RFT#01-38	FSI	GOOD TEST
3028	34378	RFT#01-38	IH	
				GOOD TEST - SAMPLE ATTEMPTED
3032.5	30592	RFT#01-37	FSI	

3032.5	34428	RFT#01-37	IH	
3081.5	175	RFT#01-35	FSI	DRY TEST
3081.5	34978	RFT#01-35	IH	
3082	0	RFT#01-33	FSI	DRY TEST
3082	34979	RFT#01-33	IH	
3082.5	166	RFT#01-32	FSI	DRY TEST
3082.5	34985	RFT#01-32	IH	
3082.5	31110	RFT#01-36	FSI	GOOD TEST
3082.5	34987	RFT#01-36	IH	
3093	34530	DMR	HP	
3095.5	31245	RFT#01-27	FSI	GOOD TEST
3095.5	35104	RFT#01-27	IH	
3095.5	31252	RFT#01-31	FSI	GOOD TEST
3095.5	35135	RFT#01-31	IH	
3118	34809	DMR	HP	
3175	32045	RFT#01-25	FSI	GOOD TEST
3175	36016	RFT#01-25	IH	
3197	32270	RFT#01-24	FSI	GOOD TEST
3197	36264	RFT#01-24	IH	
3197	0	RFT#01-28	FSI	DRY TEST
3197	36325	RFT#01-28	IH	
3197	32248	RFT#01-29	FSI	GOOD TEST - SAMPLED
3197	36267	RFT#01-29	IH	
3197.5	32296	RFT#01-30	FSI	GOOD TEST
3197.5	36276	RFT#01-30	IH	
3225	36003	DMR	HP	
3227	37165	DMR	HP	
3255	32847	RFT#01-23	FSI	GOOD TEST
3255	36899	RFT#01-23	IH	
3281	33108	RFT#01-22	FSI	GOOD TEST
3281	38189	RFT#01-22	IH	
3320	37455	DMR	HP	
3382	34142	RFT#01-21	FSI	GOOD TEST
3382	38316	RFT#01-21	IH	
3388.5	34209	RFT#01-20	FSI	GOOD TEST
3388.5	38309	RFT#01-20	IH	
3398.5	34309	RFT#01-19	FSI	GOOD TEST
3398.5	38493	RFT#01-19	IH	
3404	38402	DMR	HP	
3429	38281	DMR	HP	

3449.5	34858	RFT#01-18	FSI	GOOD TEST
3449.5	39062	RFT#01-18	IH	
3490	38962	DMR	HP	
3517	35527	RFT#01-16	FSI	GOOD TEST
3517	39812	RFT#01-16	IH	
3553	35895	RFT#01-15	FSI	GOOD TEST
3553	41212	RFT#01-15	IH	
3568	36040	RFT#01-14	FSI	GOOD TEST
3568	40377	RFT#01-14	IH	
3569	36051	RFT#01-13	FSI	GOOD TEST
3569	40388	RFT#01-13	IH	
3573	36093	RFT#01-12	FSI	GOOD TEST
3573	40430	RFT#01-12	IH	
3578	36152	RFT#01-11	FSI	GOOD TEST
3578	40489	RFT#01-11	IH	
3580	40388	DMR	HP	
3583	40422	DMR	HP	
3617	41231	DMR	HP	
3834.4	47320	FLOT#02	HP	
3834.4	75720	FLOT#02	LOP	
3848	48168	DMR	HP	
3850	48193	DMR	HP	
3869	47292	DMR	HP	
3907.5		RFT#02-41	FSI	LOST SEAL
3907.5	60357	RFT#02-41	IH	
3914	41107	RFT#02-40	FSI	
3914	60462	RFT#02-40	IH	
3918.5	41145	RFT#02-39	FSI	
3918.5	60540	RFT#02-39	IH	
3918.5	41126	RFT#02-59	FSI	SAMPLED
3918.5	61263	RFT#02-59	IH	
3920.5		RFT#02-38	FSI	TIGHT
3920.5	60567	RFT#02-38	IH	
3920.5	41161	RFT#02-38A	FSI	
3920.5	60951	RFT#02-38A	IH	
3922.5	41179	RFT#02-37	FSI	
3922.5	60600	RFT#02-37	IH	
3922.5	41181	RFT#02-37A	FSI	

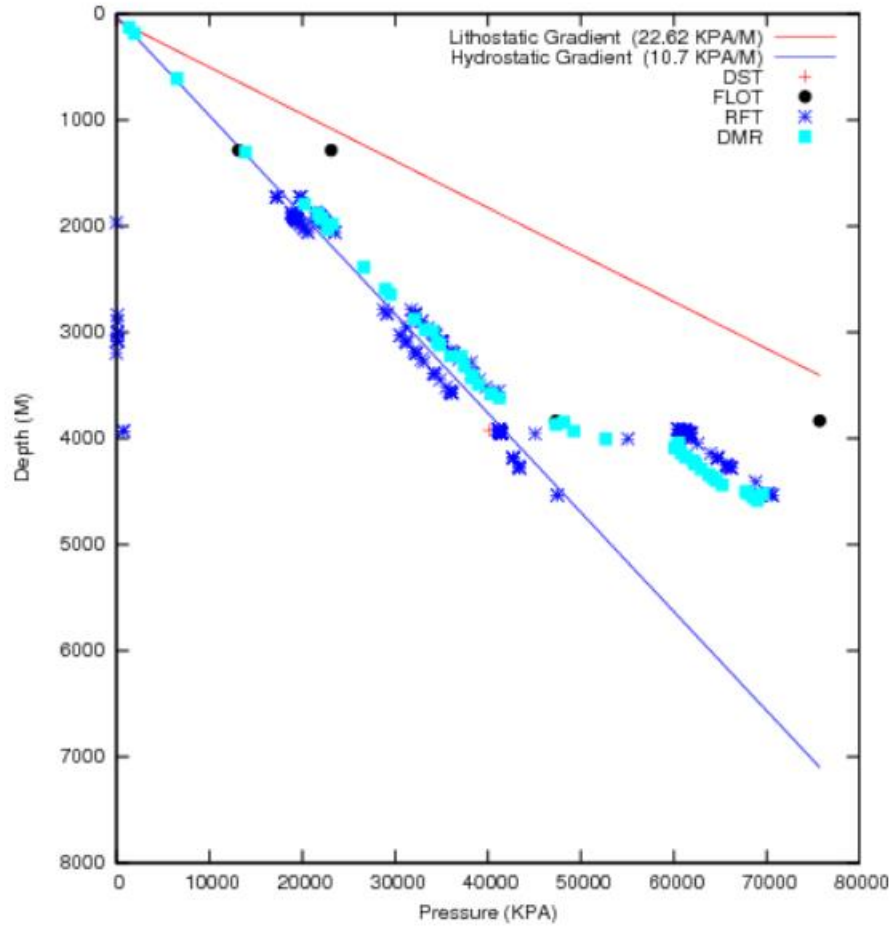
3922.5	60973	RFT#02-37A	IH	
3922.5	41157	RFT#02-56	FSI	SAMPLED
3922.5	61182	RFT#02-56	IH	
3924	40126	DST#01	SI#2	
3925		RFT#02-36	FSI	TIGHT
3925	60643	RFT#02-36	IH	
3925.5	41175	RFT#02-70	FSI	
3925.5	61032	RFT#02-70	IH	
3928		RFT#02-35	FSI	TIGHT
3928	60692	RFT#02-35	IH	
3928	41325	RFT#02-35A	FSI	
3928	61073	RFT#02-35A	IH	
3928	719	RFT#02-69	FSI	TIGHT
3928	61089	RFT#02-69	IH	
3931		RFT#02-34	FSI	TIGHT
3931	60743	RFT#02-34	IH	
3931		RFT#02-34A	FSI	TIGHT
3931	61123	RFT#02-34A	IH	
3931	787	RFT#02-68	FSI	TIGHT
3931	61158	RFT#02-68	IH	
3933	49232	DMR	HP	
3933.9		RFT#02-33	FSI	TIGHT
3933.9	60802	RFT#02-33	IH	
3935.5	41262	RFT#02-67	FSI	
3935.5	61261	RFT#02-67	IH	
3935.5	41262	RFT#02-71	FSI	
3935.5	61258	RFT#02-71	IH	
3935.8	41274	RFT#02-32	FSI	
3935.8	60833	RFT#02-32	IH	
3937.8		RFT#02-31	FSI	TIGHT
3937.8	60874	RFT#02-31	IH	
3937.8		RFT#02-31A	FSI	TIGHT
3937.8	61274	RFT#02-31A	IH	
3940.3		RFT#02-30B	FSI	TIGHT

3940.3	60923	RFT#02-30B	IH	
3940.5		RFT#02-30	FSI	TIGHT
3940.5	60933	RFT#02-30	IH	
3940.7		RFT#02-30A	FSI	TIGHT
3940.7	60938	RFT#02-30A	IH	
3942	41323	RFT#02-66	FSI	
3942	61408	RFT#02-66	IH	
3943.2		RFT#02-29	FSI	TIGHT
3943.2	60944	RFT#02-29	IH	
3943.2	41340	RFT#02-29A	FSI	
3943.2	60991	RFT#02-29A	IH	
3944	41342	RFT#02-65	FSI	
3944	61462	RFT#02-65	IH	
3945.2	41356	RFT#02-28	FSI	
3945.2	60972	RFT#02-28	IH	
3948	41378	RFT#02-52	FSI	
3948	61733	RFT#02-52	IH	
3948	41380	RFT#02-53	FSI	
3948	61737	RFT#02-53	IH	
3948.5	41391	RFT#02-27	FSI	
3948.5	61023	RFT#02-27	IH	
3948.5	41386	RFT#02-54	FSI	SAMPLED
3948.5	61810	RFT#02-54	IH	
3951	41416	RFT#02-64	FSI	
3951	61625	RFT#02-64	IH	
3951.5	41422	RFT#02-26	FSI	
3951.5	61067	RFT#02-26	IH	
3953.5	41439	RFT#02-25	FSI	
3953.5	61085	RFT#02-25	IH	
3953.5	41438	RFT#02-63	FSI	
3953.5	61697	RFT#02-63	IH	
3955	41453	RFT#02-24A	FSI	
3955	61205	RFT#02-24A	IH	
3955	41444	RFT#02-50	FSI	SAMPLED
3955	61954	RFT#02-50	IH	

3956.5	41458	RFT#02-24	FSI	
3956.5	61107	RFT#02-24	IH	
3956.9	41471	RFT#02-62	FSI	LOST SEAL
3956.9	61792	RFT#02-62	IH	
3957	45091	RFT#02-61	FSI	LOST SEAL
3957	61809	RFT#02-61	IH	
3968		RFT#02-23	FSI	TIGHT
3968	61307	RFT#02-23	IH	
3970.9		RFT#02-22	FSI	TIGHT
3970.9	61346	RFT#02-22	IH	
3998.1		RFT#02-21	FSI	NO SEAT
3998.1	61787	RFT#02-21	IH	
3998.4		RFT#02-21A	FSI	TIGHT
3998.4	61793	RFT#02-21A	IH	
4002.3		RFT#02-20	FSI	NO SEAT
4002.3		RFT#02-20	IH	
4003	52700	DMR	HP	
4003.3	55062	RFT#02-19	FSI	
4003.3	61863	RFT#02-19	IH	
4041	60573	DMR	HP	
4049	60455	DMR	HP	
4050.5		RFT#02-18	FSI	TIGHT
4050.5	62590	RFT#02-18	IH	
4090	60104	DMR	HP	
4137	60795	DMR	HP	
4141.5		RFT#02-17	FSI	TIGHT
4141.5	63965	RFT#02-17	IH	
4172	61309	DMR	HP	
4176	61368	DMR	HP	
4180.5	42674	RFT#02-16	FSI	TIGHT
4180.5	64652	RFT#02-16	IH	
4183.5	42690	RFT#02-15	FSI	
4183.5	64754	RFT#02-15	IH	
4183.5	42691	RFT#02-49	FSI	
4183.5	64770	RFT#02-49	IH	
4186		RFT#02-14	FSI	TIGHT
4186		RFT#02-14	IH	
4186.5	42706	RFT#02-14A	FSI	

4186.5	64725	RFT#02-14A	IH	
4187.3	42709	RFT#02-13	FSI	
4187.3	64733	RFT#02-13	IH	
4209	62101	DMR	HP	
4236	62250	DMR	HP	
4244	62367	DMR	HP	
4250		RFT#02-12	FSI	TIGHT
4250	65629	RFT#02-12	IH	
4256		RFT#02-11	FSI	TIGHT
4256	65741	RFT#02-11	IH	
4260.5	43263	RFT#02-10	FSI	SUPERCHARGED
4260.5	65815	RFT#02-10	IH	
4270	43325	RFT#02-09	FSI	
4270	66001	RFT#02-09	IH	
4275		RFT#02-08	FSI	TIGHT
4275	66122	RFT#02-08	IH	
4278.5	43411	RFT#02-07	FSI	
4278.5	66190	RFT#02-07	IH	
4283	43459	RFT#02-06	FSI	
4283	66275	RFT#02-06	IH	
4287	62999	DMR	HP	
4341	63793	DMR	HP	
4370	64219	DMR	HP	
4396	64601	DMR	HP	
4409		RFT#02-05	FSI	TIGHT
4409	68825	RFT#02-05	IH	
4440	65247	DMR	HP	
4502	67749	DMR	HP	
4514.5		RFT#02-04	FSI	TIGHT
4514.5	70103	RFT#02-04	IH	
4519.9		RFT#02-03	FSI	LOST SEAL
4519.9	70285	RFT#02-03	IH	
4521	68034	DMR	HP	
4522	69646	DMR	HP	
4532		RFT#02-02	FSI	VERY LOW K
4532	70520	RFT#02-02	IH	
4532.5		RFT#02-47	FSI	TIGHT
4532.5	70641	RFT#02-47	IH	
4533.5	47480	RFT#02-01	FSI	
4533.5	70581	RFT#02-01	IH	

4533.5	47480	RFT#02-48	FSI	SAMPLED
4533.5	69360	RFT#02-48	IH	
4553	68516	DMR	HP	
4587	69028	DMR	HP	



Pressure-Depth Plot - Hebron Sample Well

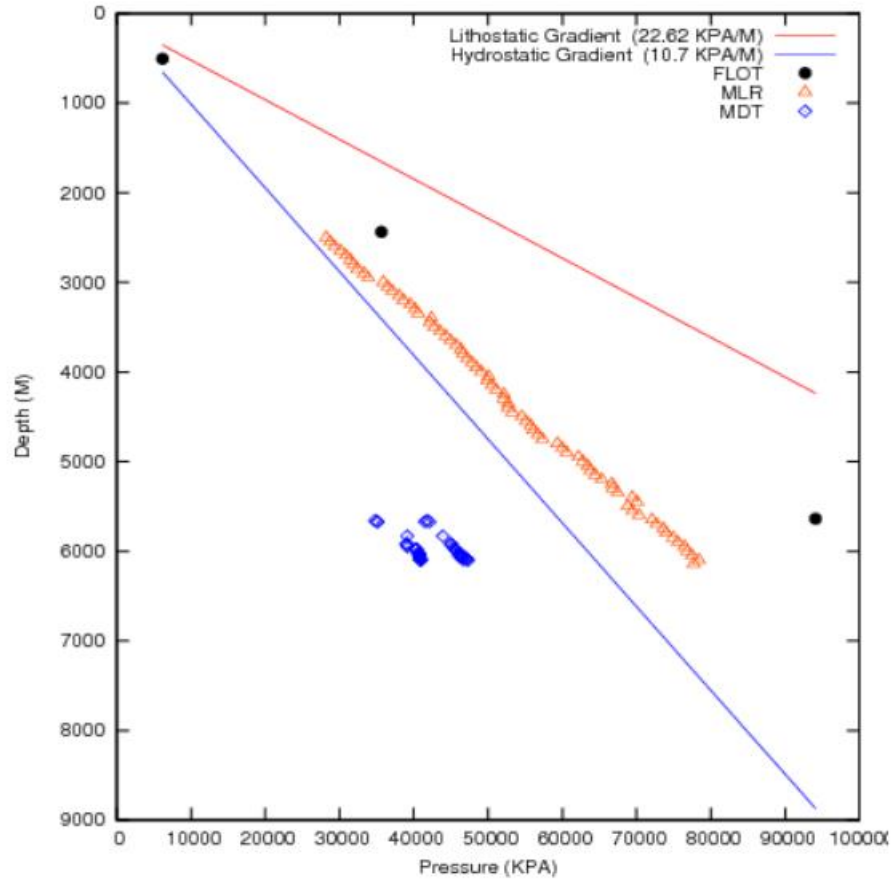
Hibernia Sample Well Pressure Data

Depth (M)	Pressure (KPA)	Testing Type	Pressure Type	Remarks
506.2	6173	FLOT#1	LOP	FORMATION INTEGRITY TEST (FIT)
2437.2	35624	FLOT#2	LOP	FORMATION INTEGRITY TEST (FIT)
2500	28204	MLR	HP	2170.3 M (TVD)
2550	28768	MLR	HP	2195.9 M (TVD)
2600	29332	MLR	HP	2221.2 M (TVD)
2650	30156	MLR	HP	2246.1 M (TVD)
2700	30857	MLR	HP	2270.1 M (TVD)
2750	31429	MLR	HP	2292.7 M (TVD)
2800	31863	MLR	HP	2313.6 M (TVD)
2850	32432	MLR	HP	2334.1 M (TVD)
2900	33285	MLR	HP	2353.7 M (TVD)
2950	33859	MLR	HP	2372.1 M (TVD)
3000	35905	MLR	HP	2389.7 M (TVD)
3050	36503	MLR	HP	2406.9 M (TVD)
3100	37101	MLR	HP	2423.9 M (TVD)
3150	38009	MLR	HP	2440.7 M (TVD)
3200	38612	MLR	HP	2457.3 M (TVD)
3250	39534	MLR	HP	2473.4 M (TVD)
3300	40143	MLR	HP	2489.2 M (TVD)
3350	40586	MLR	HP	2504.9 M (TVD)
3400	42360	MLR	HP	2519.7 M (TVD)
3450	42136	MLR	HP	2533.8 M (TVD)
3500	42747	MLR	HP	2547.8 M (TVD)
3550	43532	MLR	HP	2561.3 M (TVD)
3600	44322	MLR	HP	2574.1 M (TVD)
3650	44937	MLR	HP	2587.4 M (TVD)
3700	45734	MLR	HP	2601 M (TVD)
3750	46352	MLR	HP	2614.6 M (TVD)
3800	46598	MLR	HP	2628.4 M (TVD)
3850	47211	MLR	HP	2642.2 M (TVD)
3900	47824	MLR	HP	2656.6 M (TVD)
3950	48437	MLR	HP	2671 M (TVD)
4000	49050	MLR	HP	2684.8 M (TVD)
4050	50060	MLR	HP	2698.5 M (TVD)

4100	49874	MLR	HP	2712 M (TVD)
4150	50482	MLR	HP	2725.1 M (TVD)
4200	51090	MLR	HP	2738.2 M (TVD)
4250	52116	MLR	HP	2751.5 M (TVD)
4300	52096	MLR	HP	2765.1 M (TVD)
4350	52702	MLR	HP	2775.6 M (TVD)
4400	52660	MLR	HP	2791.2 M (TVD)
4450	53258	MLR	HP	2804.5 M (TVD)
4500	54519	MLR	HP	2818.5 M (TVD)
4550	55125	MLR	HP	2833.5 M (TVD)
4600	55731	MLR	HP	2849.9 M (TVD)
4650	56108	MLR	HP	2866.7 M (TVD)
4700	56712	MLR	HP	2883.8 M (TVD)
4750	57315	MLR	HP	2900.6 M (TVD)
4800	59331	MLR	HP	2917.4 M (TVD)
4850	59949	MLR	HP	2934 M (TVD)
4900	60567	MLR	HP	2950.5 M (TVD)
4950	62156	MLR	HP	2967.7 M (TVD)
5000	62784	MLR	HP	2984.3 M (TVD)
5050	63412	MLR	HP	3000.7 M (TVD)
5100	63790	MLR	HP	3017.2 M (TVD)
5150	64415	MLR	HP	3034.2 M (TVD)
5200	65295	MLR	HP	3052.2 M (TVD)
5250	66696	MLR	HP	3071.7 M (TVD)
5300	66811	MLR	HP	3093.3 M (TVD)
5350	67441	MLR	HP	3117.1 M (TVD)
5400	69396	MLR	HP	3143 M (TVD)
5450	70038	MLR	HP	3170.9 M (TVD)
5500	68793	MLR	HP	3200.9 M (TVD)
5550	69418	MLR	HP	3232.9 M (TVD)
5600	70318	MLR	HP	3266.8 M (TVD)
5638.7	94092	FLOT#3	LOP	FORMATION INTEGRITY TEST (FIT)
5650	72054	MLR	HP	3302.1 M (TVD)
5658.6	34773	MDT#03	FSI	NORMAL PRETEST
5658.6	41757	MDT#03	IH	3308.20 M (TVD)
5672.1	35083	MDT#04	FSI	NORMAL PRETEST - SLOW BUILD
5672.1	42101	MDT#04	IH	3317.89 M (TVD)
5672.6	35080	MDT#01	FSI	NORMAL PRETEST - SLOW BUILD

5672.6	41483	MDT#01	IH	3318.24 M (TVD)
5700	72692	MLR	HP	3337.9 M (TVD)
5750	73612	MLR	HP	3373.9 M (TVD)
5800	73967	MLR	HP	3410.5 M (TVD)
5831	39109	MDT#05	FSI	NORMAL PRETEST
5831	43914	MDT#05	IH	3433.57 M (TVD)
5850	74892	MLR	HP	3447.9 M (TVD)
5900	75532	MLR	HP	3486.1 M (TVD)
5915.2	39022	MDT#06	FSI	NORMAL PRETEST
5915.2	44938	MDT#06	IH	3497.87 M (TVD)
5922	39039	MDT#07	FSI	NORMAL PRETEST
5922	45009	MDT#07	IH	3503.15 M (TVD)
5925	39047	MDT#08	FSI	NORMAL PRETEST
5925	45035	MDT#08	IH	3505.45 M (TVD)
5950	76464	MLR	HP	3524.7 M (TVD)
5951.2	39125	MDT#09	FSI	NORMAL PRETEST - SLOW BUILD
5951.2	45305	MDT#09	IH	3525.64 M (TVD)
5972.2	40303	MDT#10	FSI	NORMAL PRETEST
5972.2	45520	MDT#10	IH	3541.94 M (TVD)
5977	40318	MDT#11	FSI	NORMAL PRETEST
5977	45572	MDT#11	IH	3545.67 M (TVD)
5981.1	40329	MDT#12	FSI	NORMAL PRETEST
5981.1	45600	MDT#12	IH	3548.82 M (TVD)
6000	76812	MLR	HP	3563.7 M (TVD)
6018.5	40642	MDT#13	FSI	NORMAL PRETEST
6018.5	46115	MDT#13	IH	3578.10 M (TVD)
6020	40646	MDT#14	FSI	NORMAL PRETEST
6020	46116	MDT#14	IH	3579.26 M (TVD)
6033.8	40690	MDT#15	FSI	NORMAL PRETEST
6033.8	46256	MDT#15	IH	3590.16 M (TVD)
6038	40703	MDT#16	FSI	NORMAL PRETEST
6038	46325	MDT#16	IH	3593.47 M (TVD)
6043.2	40719	MDT#17	FSI	NORMAL PRETEST
6043.2	46383	MDT#17	IH	3597.55 M (TVD)
6048.1	40734	MDT#18	FSI	NORMAL PRETEST
6048.1	46408	MDT#18	IH	3601.48 M (TVD)
6048.4	40733	MDT#27	FSI	NORMAL PRETEST - 2 SAMPLES
6048.4	46027	MDT#27	IH	3601.67 M (TVD)
6050	77452	MLR	HP	3602.9 M (TVD)

6064.9	40767	MDT#19	FSI	NORMAL PRETEST
6064.9	46639	MDT#19	IH	3614.76 M (TVD)
6070.2	40789	MDT#20	FSI	NORMAL PRETEST
6070.2	46693	MDT#20	IH	3618.95 M (TVD)
6073.6	40802	MDT#26	FSI	NORMAL PRETEST - 2 SAMPLES
6073.6	46426	MDT#26	IH	3621.56 M (TVD)
6080	40831	MDT#21	FSI	NORMAL PRETEST
6080	47051	MDT#21	IH	3626.63 M (TVD)
6085	40853	MDT#22	FSI	NORMAL PRETEST
6085	47031	MDT#22	IH	3630.59 M (TVD)
6093.5	40888	MDT#25	FSI	NORMAL PRETEST - 2 SAMPLES
6093.5	46670	MDT#25	IH	3637.34 M (TVD)
6095.1	40898	MDT#23	FSI	NORMAL PRETEST
6095.1	47177	MDT#23	IH	3638.61 M (TVD)
6100	78392	MLR	HP	3642.5 M (TVD)
6102.7	40946	MDT#24	FSI	NORMAL PRETEST
6102.7	47270	MDT#24	IH	3644.66 M (TVD)
6140	77701	MLR	HP	3674.9 M (TVD)



Pressure-Depth Plot – Hibernia Sample Well

Terra Nova Sample Well

Depth (M)	Pressure (KPA)	Testing Type	Pressure Type	Remarks
506	4959	FLOT#01	HP	
506	7108	FLOT#01	LOP	
1070	11189	MLR	HP	
1180	12757	MLR	HP	
1210	13223	MLR	HP	
1277	13505	FLOT#02	HP	
1277	21021	FLOT#02	LOP	
1297	14688	RFT#41	FH	
1297	14683	RFT#41	IH	

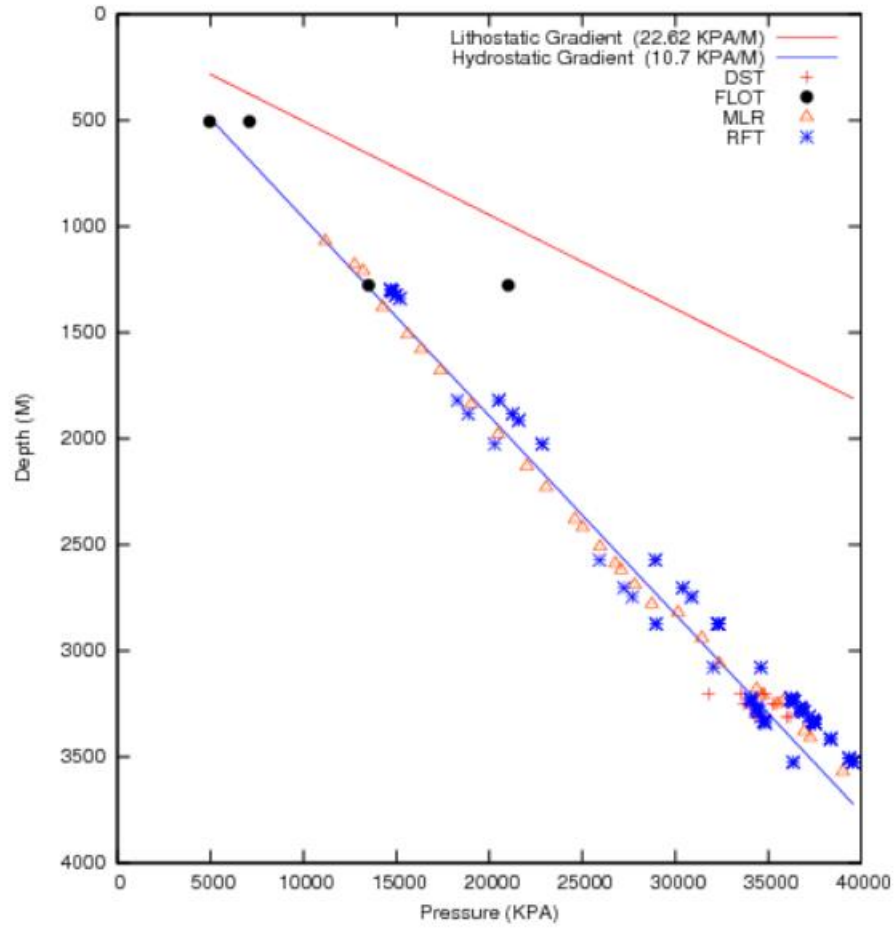
1297		RFT#41	SI	LOST SEAT
1303	14751	RFT#40	FH	
1303	14756	RFT#40	IH	
1303		RFT#40	SI	LEAKED, LOST SEAT
1308	14812	RFT#39	FH	
1308	14810	RFT#39	IH	
1308		RFT#39	SI	LOST SEAT
1323.5	14979	RFT#38	FH	
1323.5	14981	RFT#38	IH	
1323.5		RFT#38	SI	MAXIMUM DRAWDOWN
1340	15170	RFT#37	FH	
1340	15221	RFT#37	IH	
1340		RFT#37	SI	MAXIMUM DRAWDOWN
1380	14269	MLR	HP	
1510	15613	MLR	HP	
1580	16337	MLR	HP	
1680	17371	MLR	HP	
1820	20520	RFT#01	FH	
1820	20534	RFT#01	IH	
1820	18285	RFT#01	SI	PERMEABLE - FAST BUILDUP
1840	19025	MLR	HP	
1883.9	21234	RFT#02	FH	
1883.9	21248	RFT#02	IH	
1883.9	18862	RFT#02	SI	PERMEABLE - FAST BUILDUP
1914.6	21581	RFT#03	FH	
1914.6	21591	RFT#03	IH	
1914.6		RFT#03	SI	LOST SEAT
1980	20473	MLR	HP	
2026.5	22835	RFT#04	FH	
2026.5	22849	RFT#04	IH	
2026.5	20292	RFT#04	SI	PERMEABLE - GOOD TEST
2130	22024	MLR	HP	
2230	23058	MLR	HP	
2380	24609	MLR	HP	
2420	25022	MLR	HP	
2510	25953	MLR	HP	
2572.3	28929	RFT#05	FH	
2572.3	28941	RFT#05	IH	
2572.3	25930	RFT#05	SI	PERMEABLE - BAD GAUGE

				DRIFT
2590	26780	MLR	HP	
2620	27090	MLR	HP	
2690	27814	MLR	HP	
2704.1	30400	RFT#06	FH	
2704.1	30410	RFT#06	IH	
2704.1	27244	RFT#06	SI	PERMEABLE - FAST BUILDUP
2746.3	30882	RFT#07	FH	
2746.3	30892	RFT#07	IH	
2746.3	27681	RFT#07	SI	PERMEABLE - FAST BUILDUP
2780	28744	MLR	HP	
2820	30154	MLR	HP	
2872.3	32263	RFT#35	FH	
2872.3	32304	RFT#35	IH	
2872.3	28957	RFT#35	SI	PERMEABLE - SEGREGATED WATER SAMPLE
2875	32312	RFT#08	FH	
2875	32320	RFT#08	IH	
2875	28976	RFT#08	SI	PERMEABLE - GOOD TEST
2875	32347	RFT#34	FH	
2875	32358	RFT#34	IH	
2875		RFT#34	SI	SEAL FAILURE
2940	31437	MLR	HP	
3060	32360	MLR	HP	
3078.5	34602	RFT#36	FH	
3078.5	34612	RFT#36	IH	
3078.5	32054	RFT#36	SI	PERMEABLE - LARGE DRAWDOWN
3180	34378	MLR	HP	
3203.9	34666	DST#03	FH	
3203.9	31773	DST#03	FSI	
3203.9	34835	DST#03	IH	
3203.9	33499	DST#03	ISI	
3210	34702	MLR	HP	
3223.8	36242	RFT#09	FH	
3223.8	36247	RFT#09	IH	
3223.8	34022	RFT#09	SI	PERMEABLE - OIL, FAST BUILDUP
3226.5	36253	RFT#10	FH	

3226.5	36262	RFT#10	IH	
3226.5	34039	RFT#10	SI	PERMEABLE - OIL, FAST BUILDUP
3230	36278	RFT#11	FH	
3230	36284	RFT#11	IH	
3230	34063	RFT#11	SI	PERMEABLE - OIL, FAST BUILDUP
3237	36357	RFT#12	FH	
3237	36364	RFT#12	IH	
3237	34112	RFT#12	SI	PERMEABLE - OIL, FAST BUILDUP
3240	35789	MLR	HP	
3241	36393	RFT#13	FH	
3241	36400	RFT#13	IH	
3241	34138	RFT#13	SI	PERMEABLE - OIL, MINOR PLUGGING
3249.7	35428	DST#02	FH	
3249.7	34004	DST#02	FSI	
3249.7	35237	DST#02	IH	
3249.7	34008	DST#02	ISI	
3249.7	33708	DST#02	SI#2	
3250	35517	MLR	HP	
3266.5	36690	RFT#14	FH	
3266.5	36713	RFT#14	IH	
3266.5	34355	RFT#14	SI	PERMEABLE - LARGE DRAWDOWN
3272.6	36739	RFT#15	FH	
3272.6	36751	RFT#15	IH	
3272.6	34357	RFT#15	SI	PERMEABLE - LARGE DRAWDOWN
3277	36791	RFT#16	FH	
3277	36796	RFT#16	IH	
3277	34393	RFT#16	SI	PERMEABLE - FAST BUILDUP
3284	36868	RFT#17	FH	
3284	36878	RFT#17	IH	
3284	34441	RFT#17	SI	PERMEABLE - FAST BUILDUP
3289	36924	RFT#18	FH	
3289	36930	RFT#18	IH	
3289	34476	RFT#18	SI	PERMEABLE - FAST BUILDUP

3310.5	37187	RFT#19	FH	
3310.5	37199	RFT#19	IH	
3310.5	34626	RFT#19	SI	PERMEABLE - MINOR PLUGGING
3311.7	35990	DST#01	FH	
3311.7	34264	DST#01	FSI	
3311.7	36174	DST#01	IH	
3311.7	34646	DST#01	ISI	
3311.7	34632	DST#01	SI#2	
3329.7	37389	RFT#20	FH	
3329.7	37408	RFT#20	IH	
3329.7		RFT#20	SI	NO PERMEABILITY
3330	37412	RFT#21	FH	
3330	37423	RFT#21	IH	
3330	34764	RFT#21	SI	PERMEABLE - MODERATE DRAWDOWN
3332	37417	RFT#22	FH	
3332	37425	RFT#22	IH	
3332	34780	RFT#22	SI	PERMEABLE - SLIGHT DRAWDOWN
3332	37393	RFT#33	FH	
3332	37383	RFT#33	IH	
3332	34780	RFT#33	SI	PERMEABLE - SEGREGATED OIL SAMPLE
3336	37450	RFT#23	FH	
3336	37457	RFT#23	IH	
3336	34807	RFT#23	SI	PERMEABLE - FAST BUILDUP
3343.4	37522	RFT#26	FH	
3343.4	37523	RFT#26	IH	
3343.4	34868	RFT#26	SI	PERMEABLE - MODERATE DRAWDOWN
3343.6	37533	RFT#24	FH	
3343.6	37542	RFT#24	IH	
3343.6		RFT#24	SI	NOT PERMEABLE
3343.8	37526	RFT#25	FH	
3343.8	37531	RFT#25	IH	
3343.8		RFT#25	SI	NOT PERMEABLE
3380	36938	MLR	HP	
3410	37266	MLR	HP	
3415	38326	RFT#28	FH	
3415	38337	RFT#28	IH	

3415		RFT#28	SI	NOT PERMEABLE
3415.4	38359	RFT#27	FH	
3415.4	38368	RFT#27	IH	
3415.4		RFT#27	SI	NOT PERMEABLE
3507	39339	RFT#30	FH	
3507	39347	RFT#30	IH	
3507		RFT#30	SI	NOT PERMEABLE
3508.5	39371	RFT#29	FH	
3508.5	39389	RFT#29	IH	
3508.5		RFT#29	SI	NOT PERMEABLE
3525	39538	RFT#31	FH	
3525	39577	RFT#31	IH	
3525	36321	RFT#31	SI	PERMEABLE - LARGE DRAWDOWN
3527.8	39563	RFT#32	FH	
3527.8	39575	RFT#32	IH	
3527.8	36371	RFT#32	SI	PERMEABLE - LARGE DRAWDOWN
3570	39014	MLR	HP	



Pressure-Depth Plot - Terra Nova Sample Well

Whiterose Sample Well

Depth (M)	Pressure (KPA)	Testing Type	Pressure Type	Remarks
716	7488	FLOT#01	HP	
716	10185	FLOT#01	LOP	
730	7584	MLR	HP	

910	9561	MLR	HP	
1175	12345	MLR	HP	
1215	12765	MLR	HP	
1350	14263	MLR	HP	
1575	20225	MLR	HP	SIDETRACK AT 1536 M
1645	21124	MLR	HP	
1755	22691	MLR	HP	
1920	24825	MLR	HP	
2120	27411	MLR	HP	
2263	27128	FLOT#02	HP	
2263	38029	FLOT#02	LOP	
2305	25325	MLR	HP	
2560	29785	MLR	HP	
2866	41727	RFT#01-01	HP	
2866	29371	RFT#01-01	ISI	PERMEABLE
2870.7	41749	RFT#01-02	HP	
2870.7	29379	RFT#01-02	ISI	LOW PERMEABILITY
2873.8	41801	RFT#01-03	HP	
2873.8	29378	RFT#01-03	ISI	PERMEABLE
2873.8	29266	RFT#01-71	FSI	
2873.8	41948	RFT#01-71	HP	
2873.8	29281	RFT#01-71	ISI	PERMEABLE - SAMPLED
2876.8	41854	RFT#01-04	HP	
2876.8	29401	RFT#01-04	ISI	PERMEABLE
2879.5	41881	RFT#01-05	HP	
2879.5		RFT#01-05	ISI	NOT PERMEABLE
2879.8	41952	RFT#01-06	HP	
2879.8	29395	RFT#01-06	ISI	PERMEABLE
2884.9	41954	RFT#01-08	HP	
2884.9	29399	RFT#01-08	ISI	PERMEABLE
2885	41990	RFT#01-07	HP	
2885	29389	RFT#01-07	ISI	PERMEABLE
2885.1	41962	RFT#01-09	HP	
2885.1	29411	RFT#01-09	ISI	PERMEABLE
2887.3	31192	DST#06	FH	
2887.3	29013	DST#06	FSI	
2887.3	31199	DST#06	IH	
2887.3	29131	DST#06	ISI	
2888.9	31302	DST#07A	FH	
2888.9	31475	DST#07A	IH	
2888.9	28765	DST#07A	SI	

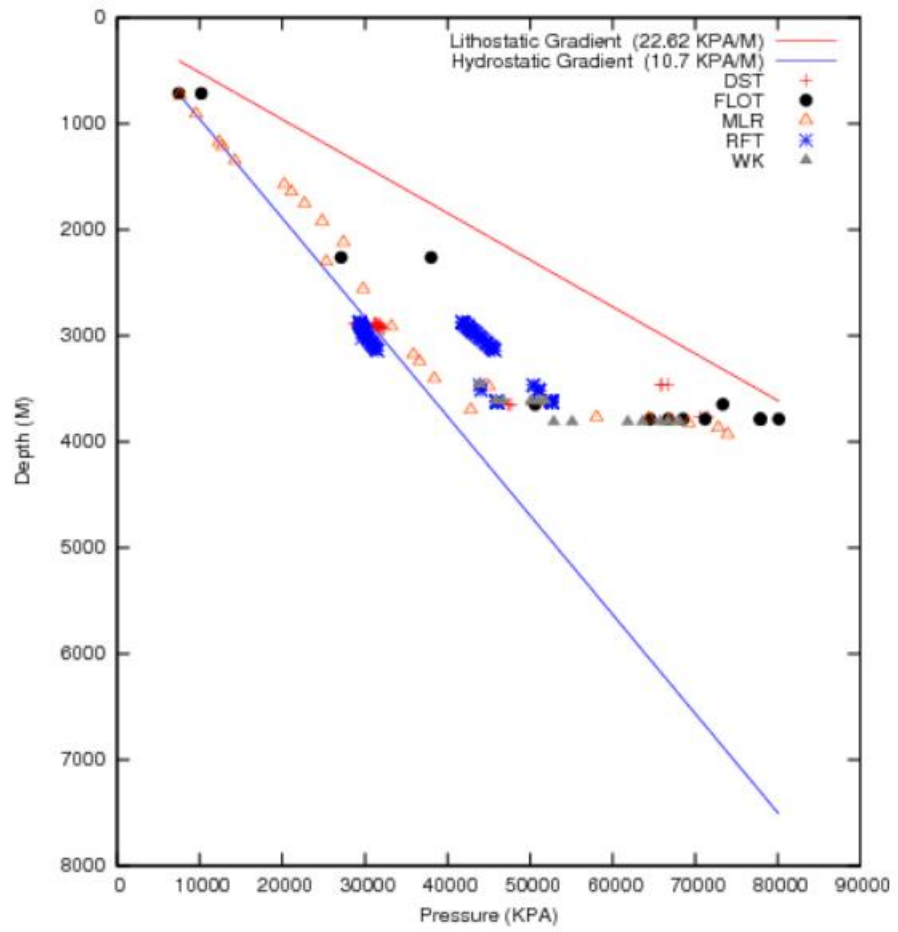
2890.3	31882	DST#05	FH	
2890.3	29096	DST#05	FSI	
2890.3	31489	DST#05	IH	
2890.3	29158	DST#05	ISI	
2892.8	42098	RFT#01-10	HP	
2892.8	29431	RFT#01-10	ISI	PERMEABLE
2905	42287	RFT#01-11	HP	
2905	29508	RFT#01-11	ISI	PERMEABLE
2905	29540	RFT#01-73	FSI	
2905	42507	RFT#01-73	HP	
2905	29564	RFT#01-73	ISI	PERMEABLE - SAMPLED
2905	29533	RFT#01-75	FSI	
2905	42428	RFT#01-75	HP	
2905	29560	RFT#01-75	ISI	PERMEABLE - SAMPLED
2908	42302	RFT#01-12	HP	
2908	29530	RFT#01-12	ISI	PERMEABLE
2915	33229	MLR	HP	
2916.2	31944	DST#04	FH	
2916.2	29179	DST#04	FSI	
2916.2	31930	DST#04	IH	
2916.2	29393	DST#04	ISI	
2918.3	42475	RFT#01-13	HP	
2918.3	29599	RFT#01-13	ISI	PERMEABLE
2920.6	31530	DST#07	FH	
2920.6	31537	DST#07	IH	
2920.6	29172	DST#07	ISI	
2925	42565	RFT#01-14	HP	
2925	29645	RFT#01-14	ISI	PERMEABLE
2929	42608	RFT#01-15	HP	
2929	29672	RFT#01-15	ISI	PERMEABLE
2934.2	32095	DST#03	FH	
2934.2	29241	DST#03	FSI	
2934.2	32316	DST#03	IH	
2934.2	29599	DST#03	ISI	
2935.9	42721	RFT#01-16	HP	
2935.9	29720	RFT#01-16	ISI	PERMEABLE
2940	42766	RFT#01-17	HP	
2940	29749	RFT#01-17	ISI	PERMEABLE
2944.5	42834	RFT#01-18	HP	
2944.5	29780	RFT#01-18	ISI	PERMEABLE
2951	42933	RFT#01-19	HP	

2951	29825	RFT#01-19	ISI	PERMEABLE
2955	42933	RFT#01-20	HP	
2955	29853	RFT#01-20	ISI	PERMEABLE
2960.2	43061	RFT#01-22	HP	
2960.2	29886	RFT#01-22	ISI	PERMEABLE
2960.3	43073	RFT#01-21	HP	
2960.3	29886	RFT#01-21	ISI	PERMEABLE
2960.4	43066	RFT#01-23	HP	
2960.4	29885	RFT#01-23	ISI	PERMEABLE
2966.9	43178	RFT#01-24	HP	
2966.9	29938	RFT#01-24	ISI	PERMEABLE
2976.5	43328	RFT#01-25	HP	
2976.5	30006	RFT#01-25	ISI	PERMEABLE
2976.5	30029	RFT#01-74	FSI	
2976.5	43426	RFT#01-74	HP	
2976.5	30063	RFT#01-74	ISI	PERMEABLE - SAMPLED
2984.4	43448	RFT#01-27	HP	
2984.4	30059	RFT#01-27	ISI	PERMEABLE
2984.5	43433	RFT#01-26	HP	
2984.5	30059	RFT#01-26	ISI	PERMEABLE
3000	43723	RFT#01-28	HP	
3000	30172	RFT#01-28	ISI	PERMEABLE
3002.8		RFT#01-29	HP	
3002.8		RFT#01-29	ISI	NO SEAT
3006.9	43778	RFT#01-30	HP	
3006.9	30219	RFT#01-30	ISI	PERMEABLE
3017.5	43955	RFT#01-31	HP	
3017.5	30302	RFT#01-31	ISI	PERMEABLE
3019.5	43957	RFT#01-32	HP	
3019.5	30318	RFT#01-32	ISI	PERMEABLE
3025.5	29604	RFT#01-33	FSI	
3025.5	44044	RFT#01-33	HP	
3025.5	30365	RFT#01-33	ISI	PERMEABLE - SAMPLED
3033.9	44194	RFT#01-34	HP	
3033.9	30447	RFT#01-34	ISI	PERMEABLE
3041.3	44298	RFT#01-35	HP	
3041.3	30520	RFT#01-35	ISI	PERMEABLE
3053.6	44516	RFT#01-36	HP	
3053.6	30636	RFT#01-36	ISI	PERMEABLE
3060	44591	RFT#01-37	HP	
3060	30701	RFT#01-37	ISI	PERMEABLE

3067.1	44681	RFT#01-38	HP	
3067.1	30769	RFT#01-38	ISI	PERMEABLE
3073.7	44779	RFT#01-39	HP	
3073.7	30835	RFT#01-39	ISI	PERMEABLE
3077.2	44815	RFT#01-40	HP	
3077.2	30872	RFT#01-40	ISI	PERMEABLE
3083.1	44910	RFT#01-41	HP	
3083.1	30928	RFT#01-41	ISI	PERMEABLE
3095	45111	RFT#01-42	HP	
3095	31042	RFT#01-42	ISI	PERMEABLE
3100.9	45191	RFT#01-43	HP	
3100.9	31103	RFT#01-43	ISI	PERMEABLE
3105.4	45251	RFT#01-44	HP	
3105.4	31141	RFT#01-44	ISI	PERMEABLE
3113.8		RFT#01-45	HP	
3113.8		RFT#01-45	ISI	NO TEST
3113.8	45341	RFT#01-46	HP	
3113.8	31244	RFT#01-46	ISI	PERMEABLE
3117	45366	RFT#01-48	HP	
3117		RFT#01-48	ISI	NOT PERMEABLE
3117.9	45399	RFT#01-47	HP	
3117.9		RFT#01-47	ISI	NOT PERMEABLE
3125	45532	RFT#01-49	HP	
3125	31324	RFT#01-49	ISI	PERMEABLE
3130.9	45612	RFT#01-50	HP	
3130.9	31396	RFT#01-50	ISI	PERMEABLE
3135.9	45675	RFT#01-51	HP	
3135.9	31443	RFT#01-51	ISI	PERMEABLE
3142.9	45786	RFT#01-52	HP	
3142.9	31599	RFT#01-52	ISI	PERMEABLE
3180	35875	MLR	HP	
3245	36608	MLR	HP	
3405	38414	MLR	HP	
3459	43909	WK#01	HP	
3463.6	65873	DST#01A	FH	
3463.6	65907	DST#01A	IH	
3463.6	66707	DST#01A	SI	
3465	43985	MLR	HP	
3465.5	50340	RFT#01-53	HP	
3465.5	43887	RFT#01-53	ISI	PERMEABLE
3472	50428	RFT#01-54	HP	

3472		RFT#01-54	ISI	NOT PERMEABLE
3472.2	50450	RFT#01-55	HP	
3472.2		RFT#01-55	ISI	NOT PERMEABLE
3480	44995	MLR	HP	
3503	51029	RFT#01-56	HP	
3503	44045	RFT#01-56	ISI	PERMEABLE
3516	51095	RFT#01-57	HP	
3516		RFT#01-57	ISI	NOT PERMEABLE
3516.1	51060	RFT#01-58	HP	
3516.1		RFT#01-58	ISI	NOT PERMEABLE
3520.5	51158	RFT#01-59	HP	
3520.5	44115	RFT#01-59	ISI	PERMEABLE
3610	51775	MLR	HP	
3610	52533	RFT#01-60	HP	
3610		RFT#01-60	ISI	NOT PERMEABLE
3610.2	52493	RFT#01-61	HP	
3610.2		RFT#01-61	ISI	NOT PERMEABLE
3613	45864	WK#02A	HP	
3613	46715	WK#02B	HP	
3613	50117	WK#02C	HP	
3613	50968	WK#02D	HP	
3613	51818	WK#02E	HP	
3615	52557	RFT#01-62	HP	
3615	45899	RFT#01-62	ISI	PERMEABLE
3616.6	52544	RFT#01-63	HP	
3616.6	45912	RFT#01-63	ISI	PERMEABLE
3616.8	45928	RFT#01-72	FSI	
3616.8	52678	RFT#01-72	HP	
3616.8	45941	RFT#01-72	ISI	PERMEABLE - SAMPLED
3620	52584	RFT#01-64	HP	
3620	46028	RFT#01-64	ISI	PERMEABLE
3622	52605	RFT#01-65	HP	
3622	45946	RFT#01-65	ISI	PERMEABLE
3627	52684	RFT#01-66	HP	
3627	46114	RFT#01-66	ISI	PERMEABLE
3627.2	52654	RFT#01-67	HP	
3627.2	46028	RFT#01-67	ISI	PERMEABLE
3633	52671	RFT#01-68	HP	
3633	46062	RFT#01-68	ISI	PERMEABLE
3633.1	52654	RFT#01-69	HP	
3633.1	46001	RFT#01-69	ISI	PERMEABLE

3635.6	52769	RFT#01-70	HP	
3635.6	46061	RFT#01-70	ISI	PERMEABLE
3648	50603	FLOT#03	HP	
3648	73327	FLOT#03	LOP	
3649.3	50284	DST#02	FH	
3649.3	47443	DST#02	FSI	
3649.3	51056	DST#02	IH	
3649.3	47740	DST#02	ISI	
3649.3	47298	DST#02	SI#2	
3700	42830	MLR	HP	SIDETRACK AT 3670 M
3768.7	71499	DST#01	FH	
3768.7	71237	DST#01	IH	
3768.7	70603	DST#01	SI	
3770	58064	MLR	HP	
3780	64411	MLR	HP	
3786	64513	FLOT#04	HP	
3786	77884	FLOT#04	LOP	NO LEAK-OFF OBSERVED
3786	66742	FLOT#05	HP	
3786	77884	FLOT#05	LOP	NO LEAK-OFF OBSERVED
3786	68525	FLOT#06	HP	
3786	77884	FLOT#06	LOP	NO LEAK-OFF OBSERVED
3786	71199	FLOT#07	HP	
3786	80112	FLOT#07	LOP	NO LEAK-OFF OBSERVED
3795	66900	MLR	HP	
3811	52864	WK#03A	HP	
3811	55107	WK#03B	HP	
3811	61836	WK#03C	HP	
3811	63631	WK#03D	HP	
3811	65837	WK#03E	HP	
3811	66734	WK#03F	HP	
3811	68080	WK#03G	HP	
3825	69230	MLR	HP	
3870	72778	MLR	HP	
3930	73907	MLR	HP	



Pressure-Depth Plot - Whiterose Sample Well

References

Aadnoy, B.S., 2010. Introduction to Geomechanics in Drilling. Mitchell, Robert F Miska, Stefan Z. Fundam. Drill. Eng. Soc. Pet. Eng. 57.

Adegoke J.O., Mofoluso F., Godstime J., Agbaje G., 2010. An Assessment of Recent Changes in the Niger Delta Coastline Using Satellite Imagery. Journal of Sustainable Development, 3(4).

Ajayi E.O. and Okosun E.A., 2014. Calcareous Nannofossil Biostratigraphy of A,B,C,D Wells, Offshore Niger Delta, Nigeria. Earth Science Research, Vol 3, No. 1.

Akhter, G., Khan, Y., Bangash, A.A., Shahzad, F., Hussain, Y., 2018. Petrophysical relationship for density prediction using V_p & V_s in Meyal oilfield, Potwar sub-basin, Pakistan. Geod. Geodyn. 9, 151-155.

Archie G.E., 1942. Electrical resistivity log as an aid in determining some reservoir characteristics. Journal of Petroleum Technology, 54-62.

Assaad, F.A., 2008. Field methods for petroleum geologists: A guide to computerized lithostratigraphic correlation charts case study: Northern Africa. Springer Science & Business Media.

Athy, L.F., 1930. Density, Porosity, and Compaction of Sedimentary Rocks. Am. Assoc. Pet. Geol. Bull. 14, 194–200. <https://doi.org/10.1306/3D93289E-16B1-11D7-8645000102C1865D>

Avseth P., Jørstad A., van Wijngaarden A.J., Mavko G., 2009. Rock physics estimation of cement volume, sorting, and net-to-gross in North Sea sandstones. *Lead Edge*.

Avseth P., Mukerji T., Mavko G., Dvorkin., 2010. A review of selected models and suggested work flows. J. Rock-physics diagnostics of depositional texture, diagenetic alterations, and reservoir heterogeneity in high-porosity siliciclastic sediments and rocks *Geophysics*.

Avseth P, Mukerji T, Mavko G, Tyssekvam J.A., 2001. Rock physics and AVO analysis for lithofacies and pore fluid prediction in a North Sea oil field. *Lead Edge*. 20(4):429-434.

Avseth, P., Jorstad, A., van Wijngaarden, A. J., and Mavko, G., 2009. Rock physics estimation of cementation, sorting and net-to-gross in North Sea sandstones, *The Leading Edge*, 28, 98-109.

Avseth, P., Skjei, N., and Mavko, G., 2012. Rock physics modeling of stress sensitivity in patchy cemented sandstones. EAGE Expanded Abstract, 74th EAGE conference, Copenhagen.

Ayonma W.F., 2015. Sequencing Stratigraphy and Depositional Environments of Middle-Late Miocene Sediments in the Eastern Part of the Coastal Swamp Depobelt, Niger Delta Basin, Nigeria. Arab Journal of Geoscience, Saudi Society of Geosciences. 9815-9827.

B. Yusuf et al., The Formation Bulk Density Prediction for Intact and Fractured Siliciclastic Rocks, Geodesy and Geodynamics, <https://doi.org/10.1016/j.geog.2019.05.005>

B. Yusuf and R. Fleming, 2018. Excess Pressure Methodology for Subsurface Properties Estimation - A Case Study. 52nd US Rock Mechanics Symposium, Seattle, Washington, USA. June 17-20.

Bourgoyne A.T. et al., 1991. Applied Drilling Engineering, SPE, Richardson, TX, pp. 246 - 252.

Birch F., 1961. The Velocity of Compressional Waves In Rocks to 10 kilobars:2. Journal of Geophysical Research, Vol 66, Issue 7.

Bourgoyne, A.T. and Rocha, A.L. Jr., 1996. A New, Simple Way to Estimate Fracture Pressure Gradient," SPEDC, September, pp. 153 - 159.

Bowers, G. L., 2001. Determining an Appropriate Pore-Pressure Estimation Strategy, Paper OTC 13042.

Breckels I.M., and Van Eekelen H.A.M., 1981. Relationship Between Horizontal Stress and Depth in Sedimentary Basins. *International Journal of Rock Mechanics and Mining Science*, 34 (09).

Brocher T.M., 2005. Empirical Relations between Elastic Wavespeeds and Density in the Earth's Crust. *Bulletin of the Seismological Society of America*, Vol. 95, No. 6, pp. 2081-2092.

Brocher T.M., Ruebel A.L., Brabb E.E., 1997. *Compilation of 59 Sonic and Density Logs from 51 Oil Test Wells in the San Francisco Bay Area, California*. US Department of the Interior, US Geological Survey.

Brocher, T.M., 2005. Empirical Relations between Elastic Wavespeeds and Density in the Earth's Crust". *Bull. Seismol. Soc. Am.* 95, 2081-2092.

Brown A. 2003. Improved interpretation of wireline pressure data. *AAPG Bulletin*, v. 87, NO. 2. 295-311.

Canada Newfoundland and Labrador Offshore Petroleum Board (CNLOPB).
<https://www.cnlopb.ca/>

Carvalho N.A, Lazary J., Pinheiro N., Mengel F. and Weinheber P., 2009. Evaluation of Reservoir Connectivity of Gimboa Field, Deepwater West Africa. In *Proceeding of Offshore Technology Conference*, Houston.

Carroll, R.D., 1969. The determination of the acoustic parameters of volcanic rocks from compressional velocity measurements, in: International Journal of Rock Mechanics and Mining Sciences & Geomechanics Abstracts. Elsevier, pp. 557-579.

Castagna, J.P., Backus, M.M., 1993. Offset-dependent reflectivity—Theory and practice of AVO analysis. Society of Exploration Geophysicists.

Castagna J.P., Batzle M.L., Eastwood R.L., 1985. Relationships between compressional-wave and shear-wave velocities in clastic silicate rocks. *Geophysics*.

Chang C., Zoback, M.D., Khaksar, A., 2006. Empirical relations between rock strength and physical properties in sedimentary rocks. *J. Pet. Sci. Eng.* 51, 223-237.

Christensen N.I. and Mooney W.D., 1995. Seismic Velocity Structure and Composition of the Continental Crust: A Global View. *Journal of Geophysical Research Atmosphere*, 100(B6), 9761-9788.

Christman S.A., 1973. Offshore Fracture Gradients. *Journal of Petroleum Technology (JPT)*, SPE Paper 4133.

Clavier, C., Hoyle, W., Meunier, D., 1971. Quantitative interpretation of thermal neutron decay time logs: part I. Fundamentals and techniques. J. Pet. Technol. 23, 743-755.

Coates G.R. and Denoo S.A., 1980. Log Derived Mechanical Properties and Rock Stress. SPWLA 21st Annual Logging Symposium, Lafayette, Louisiana.

Crombie A et al., 1998. Innovations in Wireline Fluid Sampling: Schlumberger Oilfield Review Vol. 10, No. 3, pp 26-42.

Crombie A, Halford F, Mcneil R, Thomas E.C., Mullins O.C., 1998. Innovations in Wireline Fluid Sampling. *Oil Rev.*

Daines, S.R., 1982. Prediction of fracture pressures for wildcat wells. JPT 34:863-872.

DeSilva, N.R., "Sedimentary Basins and Petroleum Systems Offshore Newfoundland and Labrador", In: Fleet, A.J., & Boldy, S.A.R. (eds.), Petroleum Geology of Northwest Europe: Proceedings of the 5th Conference, p. 501- 515, 1999.

Dewan J.T., 1983. *Essentials of Modern Open-Hole Log Interpretation*. PennWell Books.

Dey A.K. and Stewart R.R., 1997. Predicting Density using Vs and Gardner's Relationship. CREWES Research Report.

Doust H., 1990. Petroleum geology of the Niger Delta. *Geol Soc London, Spec Publ.*

Dutta N.C., 2002. Geopressure prediction using seismic data: Current status and the road ahead. *Geophysics.*

Eastwood R.L., Castagna J.P., 1983. Basis for interpretation of Vp/Vs ratios in complex lithologies. *SPWLA 24th Annual Logging Symposium.* Society of Petrophysicists and Well-Log Analysts:1-17.

Eaton, B.A., and Eaton, L.E., 1997. Fracture Gradient Prediction for the New Generation. *World Oil*, p. 93.

Eaton, B.A., 1969. Fracture Gradient Prediction and Its Application in Oilfield Operations," *JPT*, p. 246

Eaton, B.A., 1975. The Equation for Geopressure Prediction from Well Logs," paper SPE 5544 presented at the SPE Annual Technical Conference and Exhibition, Dallas, TX, September 28 - October 1.

Eberhart-Phillips D, Han D.H., Zoback M.D., 1989. Empirical relationships among seismic velocity, effective pressure, porosity, and clay content in sandstone. *Geophysics*. 54(1):82-89.

Ejedawe J.E., 1981. Patterns of Incidence of Oil Reserves in Niger Delta Basin. *Am Assoc Pet Geol Bull*. 65(9):1574-1585.

Enachescu, M.E., 1987. Tectonic and structural framework of the Northeast Newfoundland continental margin, Sedimentary basins and basin-forming mechanisms, (Eds.) Beaumont, C. and A. J. Tankard,, Basins of Eastern Canada and worldwide analogues, Canadian Society of Petroleum Geologists Memoir 12, Atlantic Geoscience Society Special Publication, vol. 5, p. 117-146

Enachescu M.E., 2005. Offshore Newfoundland and Labrador - An Emerging Energy Powerhouse. Offshore Technology Conference (OTC), 17570.

Enachescu, M.E. and Hogg J.R., 2005. Exploring for Atlantic Canada's next giant petroleum discovery. CSEG Recorder, 30, no. 5. p.19-30.

Enachescu, M.E., Smee, G.W., Negut, D.D., Skuce, A., Cilensek, S., Mewhort, L.E., Hedlin, K.J., Emery, D.J., Hale, C.A., 1998. Structural and stratigraphic resolution of marine 3-D seismic data, Jeanne d'Arc Basin offshore Newfoundland, First Joint Convention of the CSPG, CSEG and the CWLS, Geo-Triad '98, Calgary, AB, Canada, p. 383-386

Evamy B.D., Haremboure J, Kamerling P, Knaap W.A., Molloy F.A., Rowlands P.H., 1984. Hydrocarbon Habitat of Tertiary Niger Delta. *Pet Geochemistry Basin Eval AAPG Mem 35*. 62(1):325-351.

Fagan A.J. and Atkinson I.A., 2001. Petroleum Exploration in Newfoundland and Labrador: What we found and where do we go from here, Rock the Foundation Convention, Canadian Society of Petroleum Geologists.

Faust, L. Y., 1951, Seismic velocity as a function of depth and geologic time: *Geophysics*, 16 (2), 192-206

Flemings, P.B., Stump, B.B., Finkbeiner, T., Zoback, M., 2002. Flow focusing in overpressured sandstones: Theory, observations, and applications. *Am. J. Sci.* 302, 827-855.

Gardner, G.H., Gardner, L., Gregory, A., 1974. Formation Velocity and Density - The Diagnostic Basic for Stratigraphic Traps". *Geophysics* 39, 770-780.

Glover P., 2010. The Formation Density Log. Petrophysics MSc. Course Notes. University of Leeds.

Green S.M., 2012. Pressures and Overpressures in the Subsurface. Nalcor Energy-Ikon Training.

Greenberg M.L., Castagna J.P., 1992. Shear-Wave Velocity Estimation in Porous Rocks: Theoretical Formulation, Preliminary Verification and Applications1. *Geophys Prospect.* 40(2):195-209.

Gregory R.L., 1977. Vision with Insoluminant Colour Contrast: 1. A projection Technique and an Observation. *Perception* 6, 113 - 119.

Guzman-Garcia A. 2016. Excess Pressure - Formation Tester. Catrachon.wixsite.com/angelguzmangarcia/single-post/2016/05/31/Excess-Pressure-Formation-Tester-1.

Han, D., Nur, A., Morgan, D., 1986. Effects of porosity and clay content on wave velocities in sandstones. *Geophysics* 51, 2093-2107. <https://doi.org/10.1190/1.1442062>

Hamada G.M., 2004. Reservoir Fluids Identification Using V_p/V_s Ratio. *Oil and Gas Science and Technology - Rev IFP.* Vol. 59, 649-654.

Hamilton W.B., 1979. Tectonics of the Indonesian Region. US Geoplogical Survey Professional Paper 1078.

Hammond P.S and Pop J.J. 2005. Correcting Supercharging in Formation Pressure Measurements Made While Drilling. SPE 95710.

Han D, Nur A, Morgan D., 1986. Effects of porosity and clay content on wave velocities in sandstones. *Geophysics*. 51(11):2093-2107.

Hart, B.S., Flemings, P.B., Deshpande, A., 1995. Porosity and pressure: Role of compaction disequilibrium in the development of geopressures in a Gulf Coast Pleistocene basin. *Geology* 23, 45-48.

Hashem M. et al., 2010. Linear Pressure Gradients – Myths or Reality. SPWLA 51st Annual Logging Symposium, June 19-23.

Hottmann, C.E. and Johnson, R.K. (1965) Estimation of Formation Pressures from Log-Derived Shale Properties. *Journal of Petroleum Technology*, 17, 717-722.

Hoesni, M.J., 2004. Origins of overpressure in the Malay Basin and its influence on petroleum systems. (Doctoral Diss. Durham Univ.

Ikon Science. 2016. Nalcor Energy Internal Training Manual.

Jaramillo S. J., and Stewart, R. R., 2002, Well log analysis of elastic properties from the White Rose oilfield, offshore Newfoundland, CREWES Research Report Volume 14, 21 pages.

Jaramillo S. J., and Stewart, R.R., 2003, Petrophysical relationship derived from well logs in the White Rose oilfield, offshore Newfoundland. CSEG abstract.

Jenakumo T.D. and Ranasinghe M.K., 2011. Application of the Excess Pressure Technique to Investigate Connectivity of Deepwater Turbidite Reservoirs, Offshore Nigeria. In proceeding at the SPE Nigeria Annual International Conference and Exhibition, Abuja, 30 July-3 August.

Jincai Z. and Shang-Xian Y., 2017. Fracture Gradient Prediction: An Overview and Improved Method, *Journal of Petroleum Science*. 720-730.

Johnson, J. E., and Christensen N.I., 1992. Shear wave reflectivity, anisotropies, Poisson's ratios, and densities of a southern Appalachian Paleozoic sedimentary sequence, *Tectonophysics* 210, 1-20.

Knox G.J., Omatsola E.M., 1989. Development of the Cenozoic Niger Delta in terms of the 'Escalator Regression' model and impact on hydrocarbon distribution. In: *Coastal Lowlands*. Springer:181-202.

Kowallis B.J, Jones L.E.A., Wang H.F., 1984. Velocity- porosity- clay content systematics of poorly consolidated sandstones. *J Geophys Res.* 89(B12):10355-10364.

Kozlovskaya E. and Ylinieni J., 1999. Deep Structure of the Earth's Crust Along the SVEKA Profile and it's extension to the North East. *Geophysica* 1-2(1).

Kozlovskaya E., Karatayev G.R., Ylinieni J., 2001. Lithosphere structure along the northern part of EUROBRIDGE in Lithuania; results from integrated interpretation of DSS and gravity data. *Technophysics*, 339(1): 177-191.

Krasovsky S.S., 1981. Reflection of the Crustal Dynamics in Gravity Field. Naukova Dumka, Kiev, pp261.

Larionov, V. V., 1969. Radiometry of boreholes. Nedra, Moscow 127.

Lindseth R.O., 1979. Synthetic Sonic Logs - A Process for Stratigraphic Interpretation. *Geophysics* 44. 3 - 26.

Ludwig, W., Nafe, J., Drake, C., 1970. No Title. *Seism. Refract. Sea, A. E. Maxwell Vol. 4*, 53-84.

Lyons W., 2010. Working Guide to Reservoir Engineering. 1st Ed. Oxford: Gulf Publishing.

Macleod, M.K., Hanson R.A., Bell C.R., and McHugo S., 1999b. The Alba field ocean bottom cable seismic survey: Impact on development. Offshore Europe Conference, Aberdeen, SPE 56977.

Matthews W.R., Kelly, J., 1967. How to predict formation pressure and fracture gradient. *Oil Gas J.* 780 65:92-106.

Matthews, W.R., 1972. Here is How to Calculate Pore Pressure from Logs. OGJ, November 15, 1971 – January 24.

McAlpine, K. D., 1990. Mesozoic stratigraphy, sedimentary, evolution and petroleum potential of the Jeanne d'Arc Basin, Grand Banks of Newfoundland. Geological Survey of Canada, 89:17.

Mullins O.C. et al. 2005. Compartment Identification by Downhole Fluid Analysis. Petrophysics, Vol. 46, No. 4: p. 302-312.

Murat R.C., 1972. Stratigraphy and paleogeography of the Cretaceous and lower Tertiary in Southern Nigeria. *African Geol.* 251-266.

Natural Resource Canada (NRC). Basin and Wells Database. http://basin.gdr.nrcan.gc.ca/wells/index_e.php

NL Department of Mines and Energy. 2001. Sedimentary Basins and Hydrocarbon Potential of Newfoundland and Labrador.

Nwozor K.K., Onuorah L.O., Onyekuru S.O., Egbuachor C.J., 2017. Calibration of Gardner coefficient for density-velocity relationships of tertiary sediments in Niger Delta Basin. *J Pet Explor Prod Technol.* 7(3):627-635.

Petroleum P.A.O., Statoil N.S., Stanford G.M., 2012. Rock Physics Modelling of Stress Sensitivity in Patchy Cemented Sandstones. In: *74th EAGE Conference*

& Exhibition Incorporating SPE EUROPEC 2012 Copenhagen, Denmark, 4-7 June: 4-7.

Pickett G.R., 1963. Acoustic Character Logs and Their Applications in Formation Evaluation. *J Pet Technol.* 15(06):659-667.

Pickett, G. R., 1966. A review of current techniques for determination of water saturation from logs. *Journal of Petroleum Technology*, 18(11), 1-425.

Pickett, G.R., 1963. Acoustic character logs and their applications in formation evaluation. *Journal of Petroleum Technology*, 15, 650-667.

Potter, C.C., 1999. Relating density and elastic velocities in clastics: an observation. CREWES 1999 Res. Rep. 11.

Potter, C.C., Stewart, R.R., 1998. Density predictions using V_p and V_s sonic logs. CREWES Res 10, 1-10.

Quijada, M.F., Stewart, R.R., 2007. Density estimations using density-velocity relations and seismic inversion. CREWES Res Rep 19, 1-20.

Reijers T.J.A., 1996. Selected chapters in geology: sedimentary geology and sequence stratigraphy in Nigeria and three case studies and field guide. *Shell Pet Co Niger Corp Reprgr Serv Warri, 197p.*

Rubey, W.W., Hubber, K.M., 1959. Role of Fluid Pressure in Mechanics of Overthrust Faulting. *Bull. Geol. Soc. Am.* 70, 167-206.

Rodgers S. 1998. A protocol for interwell pressure comparison: *Log Analyst*, v. 39, March-April, p. 10.

Sarasty J.J. and Stewart R.R., 2002. Well log analysis of elastic properties from the White Rose oilfield , offshore Newfoundland.14:1-21.

Schlumberger: "Oilfield Glossary - Where the Oilfield Meets the Dictionary," <http://www.glossary.oilfield.slb.com>.

Sharma S. et al., 2016. A Novel Approach to Compare Pressure Regimes for Compartments Identification in Low Mobility Environment. In Proceeding at the SPE Kingdom of Saudi Arabia Annual Technical Symposium, Dammam, Saudi Arabia, April 25-28.

Short K.C., 1967. Outline of Geology of Niger Delta. *Am Assoc Pet Geol Bull.* 51(5):761-779.

Sonnichsen, GV and King, EL. 2005. Grand Bank seabed and shallow sub-bottom geology in relation to subsea engineering design. In: R. Hiscott and A.Pullham A. (Editors). *Petroleum Resources and Reservoirs of the Grand*

Banks, Eastern Canadian Margin. Geological Association of Canada Special Paper 43. 11-27 (GSC Cont.# 2002018).

Stieber, S.J., 1970. Pulsed neutron capture log evaluation-louisiana gulf coast, in: Fall Meeting of the Society of Petroleum Engineers of AIME. Society of Petroleum Engineers.

Terzaghi, K., 1943. Theoretical Soil Mechanics. John Wiley and Sons, New York City, NY.

Tixier, M.P., Loveless, G.W., Anderson, R.A., 1975. Estimation of Formation Strength From the Mechanical-Properties Log (includes associated paper 6400). J. Pet. Technol. 27, 283-293.

Tosaya C, Nur A., 1982. Effects of diagenesis and clays on compressional velocities in rocks. *Geophys Res Lett.* 9(1):5-8.

Tosaya C.A., 1982. Acoustical properties of clay-bearing rock. *PhD Thesis, StanfordUniv.* 156.

Ursenbach, C.P., 2002. Generalized Gardner relation for gas-saturated rocks. CREWES 2002 Res. Rep. 14, 1-6.

Ursenbach, C.P., 2001. A generalized Gardner relation. CREWES 2001 Res. Rep. 13, 77-82.

Van-Dunem F. et. al. 2008. Evaluating Reservoir Connectivity and Compartmentalization using a combination of Formation Tester and NMR Data: SPWLA 49TH Annual Logging Symposium, May 25-18, Edinburgh, Scotland.

White Rose DA Volume 2 (Development Plan), 2001

Wilkins R., Simmons G. and Lou C., 1984. The Ratio of V_p/V_s as a discriminant of composition of siliceous limestone. *Geophysics*, 49, 1850-1860.

Xu, H., Zhou, W., Xie, R., Da, L., Xiao, C., Shan, Y., Zhang, H., 2016. Characterization of rock mechanical properties using lab tests and numerical interpretation model of well logs. *Math. Probl. Eng.* 2016.

Zoback, M.D., 2010. *Reservoir geomechanics*. Cambridge University Press.

Zoback, M.D., Barton, C.A., Brudy, M., Castillo, D.A., Finkbeiner, T., Grollmund, B.R., Moos, D.B., Peska, P., Ward, C.D., Wiprut, D.J., 2003. Determination of stress orientation and magnitude in deep wells. *Int. J. Rock Mech. Min. Sci.* 40, 1049-1076.